Bay Area Environmental Research Institute
560 3rd Street West
Sonoma, CA 95476

FINAL PERFORMANCE REPORT

Time Period: December 31, 2000 through June 30, 2004

Project: Cooperative Agreement NCC2-1213 entitled "A Study of Cirrus Clouds and Aerosols in the Upper Troposphere using Models and Satellite Data"

Principal Investigator: Dr. Robert W. Bergstrom

Date: July 26, 2004

Table of Contents

1. Introduction

This report is the final report for the Cooperative Agreement NCC2-1213. It is a compilation of publications produced under this Cooperative Agreement and conference presentations. The tasks outlined in the various proposals are listed below with a brief comment as to the research performed.

2. NCC2-1094 Task and Accomplishments

A. An Aerosol Physical Chemistry Model for the Upper Troposphere

Task 1: To compare APCM predictions against the SUCCESS data and other aircraft campaigns and to investigate the role of aerosol composition on cirrus cloud nucleation.

Task 2: To study the seasonal evolution and spatial distribution of upper-tropospheric tropical and polar cirrus

Task 3: To investigate CLAES cirrus data with other complementary (TOGA-COARE and CEPEX) data

Publications

Tabazadeh et al, Heterogeneous chemistry involving methanol in tropospheric clouds, Geophysical Research Letters, Vol 31, Lo6114, doi:10.1029/2003GL018775 (2004)

Djijek and Tabazadeh, Effect of adsorption on the uptake of trace gases by clouds, Journal of Geophysical Research, Vol 108, No. 22, 4689, doi:10.1029/2003JD003741 (2003)

B. Upper Tropospheric Cirrus Clouds

Task 1: Assemble 3-hourly (or more frequent) meteorological satellite data from geostationary satellites to obtain a global, or nearly global, dataset of infrared brightness temperatures as a function of time for airborne experimental periods.

Task 2: Explore methods to improve the cloud top altitude distributions calculated from meteorological satellite data. This will focus on linking the 6.5 micron channel geostationary brightness temperatures and the 10.5 micron brightness temperatures.

Task 3: Explore methods to differentiate convective from stratiform cloudiness.

Task 4: Perform trajectory analyses using an existing trajectory modeling package that links the cloud data with air mass histories.

Task 5: Apply techniques from tasks 1 through 4 to provide meteorological support to the CRYSTAL-FACE mission, both in its preparation and deployment phases.

Publication

Pagen et al, Observational evidence against mountain-wave generation of ice nuclei as a prerequisite for the formation of three solid nitric acid polar stratospheric clouds observed in the Arctic in early December 1999, Journal of Geophysical Research, Vol 19, D04312, doi:10.1029/2003JD003846,2004

C. The solubility and rate coefficient for acetaldehyde uptake into low-temperature aqueous H_2SO_4

The uptake measurements were performed by Dr. Samantha Ashbourn at NASA Ames Research Center in the laboratory of Dr. Laura T. Iraci. The solubility and rate coefficient for acetaldehyde uptake into low-temperature aqueous H_2SO_4 was measured.

Publication:

Michelson et al, Dissolution, Speciation and Reaction of Acetaldehyde in Cold Sulfuric Acid, submitted to Journal of Geophysical Research, (May, 2004)

Conference presentations

Dec 2003 AGU
abstract #A41G-06
TI: Dissolution and Speciation of Oxygenated Organic Compounds in Sulfate Particles: Acetaldehyde
Michelsen, R R; Ashbourn, S F; Iraci, L T

Dec 2002 AGU
abstract# A22B-0089
TI: Uptake of Acetaldehyde in Low Temperature Sulfuric Acid
Ashbourn, S F; Biggle, K ; Conrad, D; Iraci, L T

abstract# A12F-05
TI: Separation of Solubility and Reactivity in Coupled Laboratory Data: Focus on HOBr
Iraci, L T; Ashbourn, S F; Michelsen, R R; Golden, D M

Dec 2003, Fall AGU
abstract #A32A-0112
TI: Aqueous Reaction of Methanol and Nitric Acid: Formation of Methyl Nitrate via Aerosol Chemistry
Iraci, L T; Stephenson, R M

May 2004 Spring AGU meeting, Montreal;
abstract #A23A-13
TI: Nitration of Methanol to Methyl Nitrate in $H_2SO_4/HNO_3/H_2O$ Solutions: Implications for Aerosol Chemistry
Riffel, B G; Iraci, L T; Michelsen, R R

Heterogeneous chemistry involving methanol in tropospheric clouds

A. Tabazadeh,[1] R. J. Yokelson,[2] H. B. Singh,[1] P. V. Hobbs,[3] J. H. Crawford,[4] and L. T. Iraci[1]

Received 4 October 2003; revised 2 December 2003; accepted 20 February 2004; published 23 March 2004.

[1] In this report we analyze airborne measurements to suggest that methanol in biomass burning smoke is lost heterogeneously in clouds. When a smoke plume intersected a cumulus cloud during the SAFARI 2000 field project, the observed methanol gas phase concentration rapidly declined. Current understanding of gas and aqueous phase chemistry cannot explain the loss of methanol documented by these measurements. Two plausible heterogeneous reactions are proposed to explain the observed simultaneous loss and production of methanol and formaldehyde, respectively. If the rapid heterogeneous processing of methanol, seen in a cloud impacted by smoke, occurs in more pristine clouds, it could affect the oxidizing capacity of the troposphere on a global scale. *INDEX TERMS:* 0322 Atmospheric Composition and Structure: Constituent sources and sinks; 0345 Atmospheric Composition and Structure: Pollution—urban and regional (0305); 0368 Atmospheric Composition and Structure: Troposphere—constituent transport and chemistry; 0365 Atmospheric Composition and Structure: Troposphere—composition and chemistry. **Citation:** Tabazadeh, A., R. J. Yokelson, H. B. Singh, P. V. Hobbs, J. H. Crawford, and L. T. Iraci (2004), Heterogeneous chemistry involving methanol in tropospheric clouds, *Geophys. Res. Lett.*, *31*, L06114, doi:10.1029/2003GL018775.

1. Introduction

[2] After methane, methanol (CH_3OH) is the second most abundant organic trace gas in the Earth's atmosphere [*Singh et al.*, 2000, 2001]. In the troposphere CH_3OH reacts directly with OH in the gas and aqueous phases, contributing to sources of reactive species such as formaldehyde (HCHO), ozone and hydrogen radicals. Currently, the sources and sinks of methanol are not well understood [*Singh et al.*, 2000; *Heikes et al.*, 2002; *Galbally and Kirstine*, 2002]. The mass of methanol lost in the atmosphere due to gas and aqueous phase OH oxidation is estimated to be ~100 and ~10 Tg/year [*Heikes et al.*, 2002], respectively, which is smaller than the total estimated source. According to these estimates, the lifetime of methanol in the atmosphere is primarily controlled by gas phase oxidation. Below the possibility of a heterogeneous sink for methanol is explored.

2. Measurement Summary

[3] The SAFARI 2000 (S2K) field project employed a combination of ground, airborne, and satellite instruments to study the atmospheric effects of biomass burning [*Hobbs et al.*, 2003]. The mixing of clouds and smoke was common during the S2K experiment (see auxiliary photos[1]). The bottom figure in the auxiliary file shows a smoke plume mixing with a capping cumulus cloud on August 18, 2000. The latter situation provides a unique opportunity to explore how various trace gases, particularly oxygenated organics, interact with clouds.

[4] A number of trace gases were measured with an airborne FTIR (AFTIR) instrument [*Yokelson et al.*, 1999, 2003a] during the S2K field experiment. Laboratory studies indicate that the inlet has a good passing efficiency for a large number of molecules, including CH_3OH, HCHO, and C_2H_4 [*Yokelson et al.*, 2003b]. Most reactive and stable trace gases present above 5–20 ppbv (e.g., the CH_3OH detection limit is ~5 ppb) were measured by the AFTIR.

[5] On August 18, 2000 the University of Washington's Convair-580 aircraft penetrated a fresh biomass-burning plume at various altitudes below and within a capping cumulus cloud. The AFTIR measured rapid loss and production of CH_3OH and HCHO, respectively, which correlated with increased exposure to the cloud [*Yokelson et al.*, 2003a]. Isolated, and cloud-free, plumes from three other fires were sampled at different stages in their evolutions, ranging in age from 5–45 minutes, but no significant changes of CH_3OH and HCHO were detected in these cases [*Yokelson et al.*, 2003a; *Hobbs et al.*, 2003]. This is consistent with the stability of these two compounds for the first 2–3 hours of "cloud-free" smoke aging for a biomass fire observed in Alaska [*Goode et al.*, 2000].

[6] The smoke plume was penetrated and sampled at three altitudes: once below the cloud, and twice within the cumulus cloud at different altitudes above the cloud base (Table 1). We assume that the degree of cloud processing of the smoke increases with altitude above the cloud base. From the rate of the observed ozone recovery in the smoke [*Yokelson et al.*, 2003a], the horizontal dimensions of the cloud (~3 km), the measured horizontal windspeed (5 ± 1 m s^{-1}), and typical updraft velocities (~1–2 m s^{-1}), we can estimate how long the smoke sampled was cloud-processed. The results are summarized in Table 1. We use CO as a conserved tracer to account for the dilution of

[1]Earth Science Division, NASA Ames Research Center, Moffett Field, California, USA.
[2]Department of Chemistry, University of Montana, Missoula, Montana, USA.
[3]Department of Atmospheric Sciences, University of Washington, Seattle, Washington, USA.
[4]Earth Science Division, NASA Langley Research Center, Hampton, Virginia, USA.

0094-8276/04/2003GL018775$05.00

[1]Auxiliary material are available at ftp://ftp.agu.org/apend/gl/2003GL018775.

Table 1. Observations of Chemical Changes Due to Cloud Processing of Smoke[a]

		Excess Mixing Ratio (ppb)				
Sample	H(m)	CH_3OH	HCHO	NO_2	NO	CO
1	1945	68 (0.0135)	102 (0.0202)	191 (0.0379)	185 (0.0367)	5043
2a	3866	36 (0.0135)	54 (0.0202)	101 (0.0370)	98 (0.0367)	2663
2b	3866	15 (0.0056)	59 (0.0222)	86 (0.0323)	122 (0.0458)	2663
2c	3866	−21	+5	−15	+24	2663
3a	4166	30 (0.0135)	45 (0.0202)	84 (0.0379)	81 (0.0367)	2215
3b	4166	< 5	76 (0.0343)	58 (0.0262)	121 (0.0546)	2215
3c	4166	−25 to −30	+31	−26	+40	2215

[a]Excess mixing ratio (EMR) is defined as ppbv in the smoke minus ppbv in the background. Numbers in parentheses are dimensionless quantities, which are obtained by dividing the species EMR by the CO EMR. Sample 1 gives the EMR measured below the cloud base in a diluting column. Trace gas-to-CO ratios in sample 1 (cloud free) provide the benchmark for detecting chemical changes in samples 2 and 3, which were taken after the smoke intersected a cumulus cloud. 2a and 3a give the calculated EMR at different heights, due to dilution only, which were obtained by multiplying trace gas to CO ratios in sample 1 by the EMR of CO in samples 2 and 3, respectively. 2b and 3b give the measured EMR after ~3 and ~10 mins of smoke exposure to the cloud, respectively. 2c and 3c give the inferred chemical changes (sample (b)-sample (a)) due to cloud processing of the smoke. AFTIR precision and calibration accuracy are better than 1% and 5%, respectively (1σ). The detection limits, which dominate the uncertainty (2σ) in this data are: CH_3OH and CO (~5 ppbv); NO, NO_2, and HCHO (15–20 ppbv).

the smoke [*Hobbs et al.*, 2003]. The CH_3OH gas-phase concentration measured by the AFTIR in the lowest in-cloud sample (sample 2) was not close to 36 ppb, which would occur from dilution alone, but was 15 ppb after only ~3 minutes of exposure to cloudy conditions (Figure 1). After ~10 minutes of exposure (Table 1, sample 3), the methanol concentration was below the AFTIR detection [*Yokelson et al.*, 1999, 2003a].

3. Gas- and Aqueous-Phase Oxidation

[7] Biomass burning emits large quantities of chlorine species into the atmosphere [*Li et al.*, 2003]. We performed some simple calculations to explore the possibility of oxidation chemistry involving chlorine radicals. A drop in CH_3OH concentration by more than one-half in ~3 mins (Figure 1) requires a steady state concentration of Cl in the gas phase of $\sim 7 \times 10^7$ cm^{-3} (rate constant for Cl reaction with CH_3OH is 5.5×10^{-11} cm^3 s^{-1}) [*Atkinson et al.*, 1997]. At such high Cl levels, C_2H_4 oxidation would have been complete, since it reacts with Cl about 5 times faster than methanol (rate constant for C_2H_4 reaction with Cl is 3×10^{-10} cm^3 s^{-1}) [*Atkinson et al.*, 1997]. Clearly, this did not happen since no significant loss in C_2H_4/CO ratio was measured with the AFTIR during even the first 10 mins of exposure to the cloud [see *Yokelson et al.*, 2003a, Table 1]. In addition, in cloud-free smoke, produced by another fire in the same region, the rate of oxidation in the gas phase for a large number of species was consistent with OH chemistry [*Hobbs et al.*, 2003].

[8] Having ruled out chlorine chemistry, the rapid decrease in the CH_3OH concentration cannot be explained by "standard" gas and aqueous phase chemistry (see Appendix A in the auxiliary file, reactions 1–4). In 3 mins (Figure 1), less than 0.1 ppb of CH_3OH can be lost through gas-phase reaction with OH. The maximum aqueous phase loss, where we assumed water droplets to be in thermodynamic equilibrium with the gas phase, can account for only ~7 ppb loss of CH_3OH in 3 mins. In fact, more than 3 times as much CH_3OH was lost during this time period (Table 1). Overall, measurable loss through bulk aqueous phase chemistry is highly unlikely due to mass transport limitations, since significant gas transfer into the bulk of water droplets cannot occur in 3 to 10 mins of exposure [*Jacob*, 1986] (see auxiliary file (Appendix A), for more details). Below we propose a few plausible heterogeneous chemical processes involving OH and NO_2 that may help to explain the rapid loss of gaseous CH_3OH in the cloud.

4. Possible Heterogeneous Reactions

[9] Here we use the measured rate of change in the CH_3OH gas phase concentration, as well as typical microphysical properties of cloud drops, to determine a pseudo first-order rate constant for methanol reaction on cloud droplet surfaces. In deriving the pseudo first-order rate constants below, we assumed only the gas phase supplied the oxidant to the surface of cloud drops. However, in reality, the steady state oxidant concentration at the surface is also affected by supply from the bulk phase as well as possible in situ conversion mechanisms at the surface (e.g., the reaction of $O(^1D)$ with surface water to produce in situ OH). Some recent molecular dynamics simulations suggest that the OH concentration is enriched at the interface of aqueous salt solutions [*Roeselova et al.*, 2003]. Whether this conclusion applies to water droplets in clouds requires

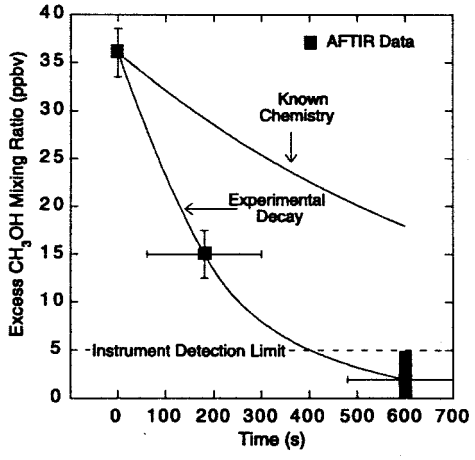

Figure 1. The measured chemical decrease in the CH_3OH gas-phase concentration as a function of exposure time to the cloud. The AFTIR data point at time zero gives the CH_3OH concentration just below the cloud base. The error bars indicate the range of measurement uncertainties. The upper line shows the maximum calculated decrease in the CH_3OH gas-phase concentration based on known aqueous phase chemistry since the gas phase loss due to the reaction with OH is negligible. The lower line shows a fit to the experimental data. The experimental decay curve was used to derive a range of possible heterogeneous rate constants, which are given in the auxiliary file (Appendix A). See caption to Table 1 and the auxiliary file (Appendix A) for more details.

further investigation. However, it is beyond the scope of this paper to distinguish what processes may have contributed to the oxidant concentration at or near the surface.

[10] The most likely heterogeneous process to consider here is the reaction of adsorbed CH_3OH with OH:

$$CH_3OH(s) + OH(g) \rightarrow CH_2OH(s) + H_2O(s)$$

$$CH_2OH(g) + O_2(g) \rightarrow HCHO(g) + HO_2(g)$$

This heterogeneous process may also help to explain why a rapid production of HCHO was simultaneously observed in the cloud (Table 1). Laboratory measurements indicate that CH_3OH on dry ammonium sulfate surfaces (relative humidity (RH) ~35%) can react with OH to yield formaldehyde [*Oh and Andino*, 2000, 2001]. According to these measurements, the rate of gas phase methanol reaction with OH is enhanced by about 30% in the presence of dry ammonium sulfate surfaces at ~35% RH. However, no yield for CH_3OH reaction with OH on dry ammonium sulfate was measured at ~3% RH [*Sorensen et al.*, 2002]. Since the RH conditions were different in the above experiments, we suspect that the rate of this reaction may have a dependence on the RH and/or the physical phase of the particles. In the Sorensen *et al.* study, it was assumed that OH was only supplied to the surface from the gas phase. While this assumption may hold at 3% RH, at higher RHs other mechanisms (noted above) may also supply OH to the surface of particles, thereby enhancing the overall rate of this surface oxidation process. More experimental work is needed to investigate whether the above reaction can occur at a faster rate on cloud drop surfaces.

[11] To obtain a pseudo first-order rate constant for the heterogeneous CH_3OH reaction with OH, the measurements shown in Figure 1 were used. Assuming a constant concentration for gas phase OH in the smoke ($[OH] = 2 \times 10^7$ cm^{-3}) [*Hobbs et al.*, 2003], the change in the CH_3OH gas-phase concentration can be calculated from,

$$\ln\frac{[CH_3OH]_f}{[CH_3OH]_i} = -\left[k_g + k_{aq}^* + k_{het}^{OH}\right][OH]_g \Delta t$$

where, $[CH_3OH]_i$ is the expected concentration of CH_3OH in sample 2 (~36 ppbv), and $[CH_3OH]_f$ is the measured concentration of CH_3OH in sample 2. We set $[CH_3OH]_f$ = 15 ppbv and Δt = 180 s (see Table 1) to derive a value for the rate of this heterogeneous process (k_{het}^{OH}) at −5°C. The rest of the parameters in the above equation are constant and are given in the auxiliary file (Appendix A).

[12] The normalized pseudo first-order heterogeneous rate constant obtained here (~3.7×10^{-8} cm^3 s^{-1} cm, see Appendix A in the auxiliary file) is about 300 times larger than the gas-phase rate constant for the conditions sampled in this cloud (S = 0.0063 cm^2 cm^{-3}, where S is the surface area of cloud droplets per unit volume of air). Although this relative increase appears to be too large, it is perhaps more useful to compare the heterogeneous and aqueous phase loss rates to assess whether the inferred rates derived here are plausible. To do so we analyze the loss rates calculated and measured for sample 2 (Table 1). The maximum aqueous phase methanol loss for sample 2 is 7 ppb (Figure 1). On the other hand, the observed loss for sample 2 is 21 ppb (Table 1), indicating that the heterogeneous loss is ~3 times faster (21/7) than the maximum aqueous phase loss. In a recent study, the reaction of $Cl_2^{\bullet-}$ radical anion with ethanol was found to be at least two times faster at the air-water interface than in the bulk [*Strekowski et al.*, 2003]. Thus the inferred loss rate calculated here for the methanol reaction with OH on the cloud surface is consistent with current information (admittedly limited) on reactions of radicals with small alcohols on aqueous surfaces.

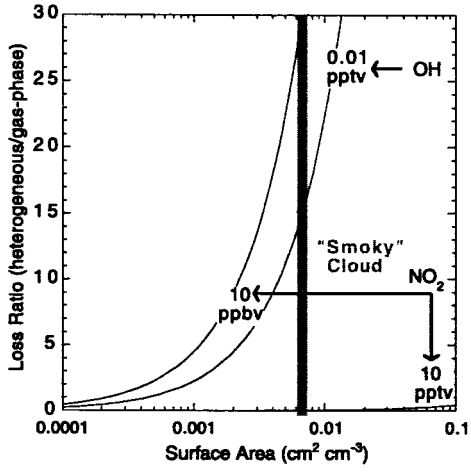

Figure 2. The ratio of heterogeneous-to-gas phase loss of CH_3OH as a function of surface area of cloud drops for an assumed range of oxidant concentrations. The gas-phase and heterogeneous rate constants used in the calculations are given in the auxiliary file (Appendix A). The heterogeneous loss is calculated for a period of 1 h (rate = $1 \times k_{het} \times S$ [oxidant] [CH_3OH]). The gas phase loss is calculated for a period of 24 h (rate = $24 \times k_{gas}$[OH] [CH_3OH]). Gas-phase OH concentration was set to 10^6 cm^{-3} for all calculations. See text for more details. The surface area of the particles in the cloud affected by smoke, which was sampled on August 18, 2000, is indicated on the plot by the shaded vertical line.

[13] Another possible heterogeneous process is the reaction of adsorbed methanol with gas phase NO_2:

$$CH_3OH(s) + 2NO_2(g) \rightarrow CH_3ONO(s) + HNO_3(s)$$

$$CH_3ONO(g) + h\nu \rightarrow CH_3O(g) + NO(g)$$

$$CH_3O(g) + O_2(g) \rightarrow HCHO(g) + HO_2(g)$$

where methyl nitrite (CH_3ONO) photolyzes in the gas phase, as shown above, to yield NO and formaldehyde. *Taylor et al.* [1980] showed that the photochemical lifetime of CH_3ONO is nearly independent of altitude and is ~2 mins. Laboratory studies indicate that the reaction of CH_3OH with NO_2 is enhanced catalytically on various surfaces, including stainless steel, Pyrex and smog chamber walls [*Takagi et al.*, 1986]. We used pseudo first-order kinetics to derive a normalized rate constant (~4.3×10^{-13} cm^3 s^{-1} cm, see Appendix A in the auxiliary file) for the CH_3OH reaction with NO_2. The procedure used is identical to that described above for the reaction with OH.

[14] Of the two reactions proposed above, the OH reaction is more plausible since methanol loss (~25–30 ppb) and HCHO production in sample 3 (31 ppb) are nearly identical (see Table 1). However, the measurements seem to indicate that NO_2 and methanol were consumed as NO and HCHO were produced in the cloud (Table 1), which provides some support for the NO_2 surface reaction.

5. Atmospheric Implications

[15] In Figure 2 the ratio of heterogeneous-to-gas phase loss of CH_3OH is shown using the rate constants given in Appendix A for typical ranges of oxidant concentrations. The heterogeneous loss is calculated assuming that an air mass spends on average ~1 h in cloudy air each day [*Jacob*, 1999]. The gas phase loss is calculated for 24 h. If the heterogeneous rate constants derived in this work from field data are applicable to the global troposphere, then clouds can provide a major sink for gas-phase CH_3OH through reaction with OH. For the NO_2 reaction, the effect could be significant only for polluted conditions.

[16] In clouds affected by smoke there might be significant organic coverage on the surface. This might, in turn, promote the methanol uptake and oxidation on the surface. In clouds unaffected by smoke, the surface tension of water droplets is lower than pure water due to organic contamination [*Facchini et al.*, 2000]. Partial or complete organic coatings may provide a more suitable medium for CH_3OH uptake and for reactions to occur in the global atmosphere [*Djikaev and Tabazadeh*, 2003]. However, the rate of heterogeneous CH_3OH oxidation in the global atmosphere may be lower than that determined here for a "dirty" cloud, since organic layers on aqueous surfaces are probably thicker and more prominent in smoky environments.

[17] Clearly, future targeted laboratory and fieldwork are needed to determine whether the heterogeneous CH_3OH loss, reported here to occur rapidly in a cloud affected by smoke, also occurs in more pristine clouds. The mixing of clouds and smoke is quite common throughout the tropics [e.g., *Reid et al.*, 1998]. If the heterogeneous reactions proposed here occur in cleaner environments, then oxidation of methanol on cloud drops would be a more important process, since methanol and clouds are globally distributed in the Earth's atmosphere. Thus, heterogeneous oxidation in clouds has the potential to provide a major global source for reactive organic species (e.g., HCHO, CH_3ONO), as well as a sink for CH_3OH.

[18] **Acknowledgments.** We thank Prof. Roger Atkinson for helpful comments and discussions. Data collection was supported by grants NAG5-9022 and NAG5-7675 from NASA's Radiation Science Program and grants ATM-9901G24, ATM-9900494, and ATM-0228003 from NSF's Division of Atmospheric Sciences.

References

Atkinson, R., et al. (1997), Evaluated kinetic, photochemical, and heterogeneous data for atmospheric chemistry: Supplement V, *J. Phys. Chem. Ref. Data*, *26*, 521.

Djikaev, Y., and A. Tabazadeh (2003), The effect of surface adsorption on the uptake of organic trace gas by cloud droplets, *J. Geophys. Res.*, *108*(D22), 4689, doi:10.1029/2003JD003741.

Facchini, M. C., et al. (2000), Surface tension of atmospheric wet aerosol and cloud/fog droplets in relation to the organic carbon content and chemical composition, *Atmos. Environ.*, *34*, 4853.

Galbally, I. E., and W. Kirstine (2002), The production of methanol by flowering plants and the global cycle of methanol, *J. Atmos. Chem.*, *43*, 195.

Goode, J. G., et al. (2000), Measurements of excess O_3, CO_2, CO, CH_4, $C2H_4$, C_2H_2, HCN, NO, NH_3, HCOOH, CH_3COOH, HCHO, and CH_3OH in 1997 Alaskan biomass burning plumes by airborne Fourier transform infrared spectroscopy (AFTIR), *J. Geophys. Res.*, *105*, 2147.

Heikes, B. G., et al. (2002), Atmospheric methanol budget and ocean implications, *Global Biogeochem. Cycles*, *16*(4), 1133, doi:10.1029/2002GB001895.

Hobbs, P. V., et al. (2003), Evolution of particle and gas emissions from a savanna fire in South Africa, *J. Geophys. Res.*, *108*(D13), 8485, doi:10.1029/2002JD002352.

Jacob, D. J. (1986), Chemistry of OH in remote clouds and its role in the production of formic acid and peroxymonosulfate, *J. Geophys. Res.*, *91*, 9807.

Jacob, D. J. (1999), Heterogeneous chemistry and tropospheric ozone, *Atmos. Environ.*, *34*, 2131.

Li, J., et al. (2003), Individual aerosol particles from biomass burning in southern Africa: 2. Composition and aging of inorganic particles, *J. Geophys. Res.*, *108*(D13), 8484, doi:10.1029/2002JD002310.

Oh, S., and J. M. Andino (2000), Effects of ammonium sulfate aerosols on the gas-phase reactions of hydroxyl radical with organic compounds, *Atmos. Environ.*, *34*, 2091.

Oh, S., and J. M. Andino (2001), Kinetics of the gas-phase reactions of hydroxyl radicals with C_1–C_6 aliphatic alcohols in the presence of ammonium sulfate aerosols, *Int. J. Chem. Kinetics*, *33*, 422.

Reid, J. S., et al. (1998), Physical, chemical, and optical properties of regional hazes dominated by smoke in Brazil, *J. Geophys. Res.*, *103*, 32,059.

Roeselova, M., et al. (2003), Impact, trapping and accommodation of hydroxyl radical and ozone at aqueous salt aerosol surfaces. A molecular dynamics study, *J. Phys. Chem. B.*, *107*, 12,690.

Singh, H. B., et al. (2000), Distribution and fate of selected oxygenated organic species in the troposphere and lower stratosphere over the Atlantic, *J. Geophys. Res.*, *105*, 3795.

Singh, H. B., et al. (2001), Evidence from the pacific troposphere for large global sources of oxygenated organic compounds, *Nature*, *410*, 1078.

Sorensen, M., et al. (2002), Do aerosols act as catalysts in the OH radical initiated atmospheric oxidation of volatile organic compounds?, *Atmos. Environ.*, *36*, 5947.

Strekowski, R. S., R. Remorov, and C. George (2003), Direct kinetic study of the reaction of $Cl_2^{\bullet-}$ radical anion with ethanol at the air-water interface, *J. Phys. Chem. A.*, *107*, 2497.

Takagi, H., et al. (1986), Formation of methyl nitrite in the surface reaction of nitrogen dioxide and methanol. 1. Dark reaction, *Environ. Sci. Technol.*, *20*, 387.

Taylor, W. D., et al. (1980), Atmospheric photodissociation lifetimes for nitromethane, methyl nitrite, and methyl nitrate, *Int. J. Chem. Kinet.*, *12*, 231.

Yokelson, R. J., et al. (1999), Emissions of formaldehyde, acetic acid, methanol, and other trace gases from biomass fires in North Carolina measured by airborne Fourier transform infrared spectroscopy, *J. Geophys. Res.*, *104*, 30,109.

Yokelson, R. J., et al. (2003a), Trace gas measurements in nascent, aged, and cloud-processed smoke from African savanna fires by airborne Fourier transform infrared spectroscopy, *J. Geophys. Res.*, *108*(D13), 8478, doi:10.1029/2002JD002322.

Yokelson, R. J., et al. (2003b), Evaluation of adsorption effects on measurements of ammonia, acetic acid, and methanol, *J. Geophys. Res.*, *108*(D20), 4649, doi:10.1029/2003JD003549.

J. H. Crawford, Earth Science Division, NASA Langley Research Center, Mail Stop 401-B 21 Langley Blvd., Room 207, Hampton VA 23681-0001, USA.

P. V. Hobbs, Department of Atmospheric Sciences, University of Washington, Seattle, WA 98195-1640, USA.

L. T. Iraci, H. B. Singh, and A. Tabazadeh, Earth Science Division, NASA Ames Research Center, Moffett Field, CA 94035, USA. (atabazadeh@mail.arc.nasa.gov)

R. J. Yokelson, Department of Chemistry, University of Montana, Missoula, MT 59812, USA.

Observational evidence against mountain-wave generation of ice nuclei as a prerequisite for the formation of three solid nitric acid polar stratospheric clouds observed in the Arctic in early December 1999

Kathy L. Pagan,[1] Azadeh Tabazadeh,[2] Katja Drdla,[2] Mark E. Hervig,[3]
Stephen D. Eckermann,[4] Edward V. Browell,[5] Marion J. Legg,[6] and Patricia G. Foschi[7]

Received 9 June 2003; revised 13 October 2003; accepted 16 December 2003; published 26 February 2004.

[1] A number of recently published papers suggest that mountain-wave activity in the stratosphere, producing ice particles when temperatures drop below the ice frost point, may be the primary source of large NAT particles. In this paper we use measurements from the Advanced Very High Resolution Radiometer (AVHRR) instruments on board the National Oceanic and Atmospheric Administration (NOAA) polar-orbiting satellites to map out regions of ice clouds produced by stratospheric mountain-wave activity inside the Arctic vortex. Lidar observations from three DC-8 flights in early December 1999 show the presence of solid nitric acid (Type Ia or NAT) polar stratospheric clouds (PSCs). By using back trajectories and superimposing the position maps on the AVHRR cloud imagery products, we show that these observed NAT clouds could not have originated at locations of high-amplitude mountain-wave activity. We also show that mountain-wave PSC climatology data and Mountain Wave Forecast Model 2.0 (MWFM-2) raw hemispheric ray and grid box averaged hemispheric wave temperature amplitude hindcast data from the same time period are in agreement with the AVHRR data. Our results show that ice cloud formation in mountain waves cannot explain how at least three large-scale NAT clouds were formed in the stratosphere in early December 1999. *INDEX TERMS:* 0320 Atmospheric Composition and Structure: Cloud physics and chemistry; 3334 Meteorology and Atmospheric Dynamics: Middle atmosphere dynamics (0341, 0342); 3360 Meteorology and Atmospheric Dynamics: Remote sensing; 3329 Meteorology and Atmospheric Dynamics: Mesoscale meteorology; 3349 Meteorology and Atmospheric Dynamics: Polar meteorology; *KEYWORDS:* AVHRR, NAT PSC formation mechanism, mountain wave cooling

Citation: Pagan, K. L., A. Tabazadeh, K. Drdla, M. E. Hervig, S. D. Eckermann, E. V. Browell, M. J. Legg, and P. G. Foschi (2004), Observational evidence against mountain-wave generation of ice nuclei as a prerequisite for the formation of three solid nitric acid polar stratospheric clouds observed in the Arctic in early December 1999, *J. Geophys. Res.*, *109*, D04312, doi:10.1029/2003JD003846.

1. Introduction

[2] Lidar observations show that both liquid (Type Ib) and solid (Type Ia) HNO_3-containing polar stratospheric cloud (PSC) particles are abundant in the winter polar stratosphere [*Browell et al.*, 1990; *Toon et al.*, 2000]. While the formation of liquid HNO_3-containing cloud particles in the stratosphere is now well understood, the nucleation mechanism for solid HNO_3 PSC formation still remains controversial [*World Meteorological Organization*, 2003]. Both homogeneous [*Salcedo et al.*, 2001; *Tabazadeh et al.*, 2001] and heterogeneous [*Tolbert and Toon*, 2001; *Drdla et al.*, 2003] freezing mechanisms have been suggested to account for the formation of solid nitric acid particles in the stratosphere. For standard homogenous and heterogeneous nucleation mechanisms to operate, the cooling caused by synoptic-scale uplift of air masses [*Teitelbaum et al.*, 2001; *Hitchman et al.*, 2003] can provide favorable conditions for solid nitric acid (NAT) clouds to form. In addition, *Carslaw et al.* [1998, 1999] have shown evidence for NAT cloud formation in air masses passing through regions of high-amplitude mountain-wave activity in the Arctic. NAT is assumed to nucleate heterogeneously on ice particles formed in mountain waves, leading to the release of small NAT particles when the ice evaporates in the warmer synoptic-scale temperatures downstream. If the synoptic-scale temperatures remain below the NAT threshold temperature, they can continue to take up HNO_3 and

[1]San Francisco State University, San Francisco, California, USA.
[2]NASA Ames Research Center, Moffett Field, California, USA.
[3]G & A Technical Software, Inc., Driggs, Idaho, USA.
[4]Naval Research Laboratory, Washington, DC, USA.
[5]NASA Langley Research Center, Hampton, Virginia, USA.
[6]Bay Area Environmental Research Institute, Sonoma, California, USA.
[7]Romberg Tiburon Center for Environmental Studies, San Francisco State University, Tiburon, California, USA.

0148-0227/04/2003JD003846$09.00

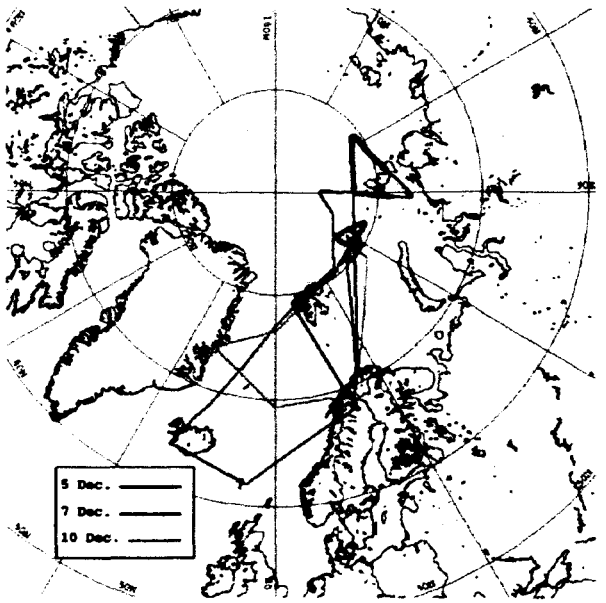

Figure 1. DC-8 flight paths for 5 December (red), 7 December (blue), and 10 December (green) 1999. The flight segments where the DC-8 DIAL lidar measured Type Ia PSCs are noted with a bold line.

H_2O and form NAT clouds. This process is described in detail by *Zondlo et al.* [2000]. A number of recent studies have provided additional support for the involvement of mountain-wave activity in the formation of NAT clouds in middle to late January 2000 within the Arctic vortex [*Fueglistaler et al.*, 2002a, 2002b; *Dhaniyala et al.*, 2002; *Luo et al.*, 2003; *Voight et al.*, 2003].

[3] Our approach in searching for the mechanism of NAT cloud formation described in this paper is novel. We use thermal infrared Advanced Very High Resolution Radiometer (AVHRR) data to map regions of ice PSCs formed by mountain-wave activity in the Arctic and then attempt to connect these regions (in time and space using trajectories) with regions where the DC-8 lidar observed NAT clouds. We also compare the AVHRR data with the location and timing of ice PSCs as predicted by the Mountain Wave Forecast Model Version 2 (MWFM-2). Our findings suggest that NAT clouds can indeed form in the stratosphere without ever passing through regions of mountain-wave activity. This is in agreement with an earlier analysis of Airborne Arctic Stratospheric Expedition (AASE) lidar observations of Type Ia PSCs by *Tabazadeh et al.* [1996]. However, our analysis cannot determine whether homogeneous nucleation or heterogeneous nucleation on particles other than ice was involved in causing the formation of these three NAT clouds in early December 1999 within the Arctic vortex.

[4] The article is organized as follows: In section 2, lidar data for the three NAT clouds observed on 5, 7, and 10 December 1999 are presented. In section 3, location and temperature histories of back trajectories calculated for each PSC event are shown. In section 4, the AVHRR ice PSC mapping algorithm is described and an ice PSC map is shown for the period 25 November to 10 December 1999. Back trajectory data are compared with the AVHRR ice PSC map to determine if the three NAT clouds were formed upstream in regions of mountain-wave activity with sufficient cooling to form ice PSCs. We also compare AVHRR ice PSC statistics for early December 1999 and January 2000 with mountain-wave ice PSC climatology statistics derived by *Dörnbrack and Leutbecher* [2001]. In section 5, we compare MWFM-2 hindcast data with the AVHRR ice PSC data and back trajectory data. Finally, in section 6, we present our conclusions and briefly discuss possible nucleation mechanisms that might account for the formation of the three NAT clouds observed in early December 1999.

2. DC-8 Lidar PSC Observations

[5] The NASA DC-8 made numerous flights in the Arctic region during the SAGE III Ozone Loss and Validation Experiment (SOLVE). The DC-8 Differential Absorption Lidar (DIAL) observed PSCs on 5, 7, and 10 December 1999, centered near 80°N and 24°E, 80°N and 105°E, and 81°N and 60°E, respectively. The DC-8 flight path and the PSC location for each of these three days are shown in Figure 1. These were large-scale PSCs, with areal extents, as measured along the DC-8 flight path, of approximately 500 km, 1405 km, and 992 km for 5, 7, and 10 December, respectively. All of these PSCs exhibited low scattering ratios and high depolarization ratios that are indicative of Type Ia (NAT) PSCs [*Browell et al.*, 1990]. Plots of the infrared depolarization ratios at 1064 nm in Figure 2 show the PSCs to be centered at ~20 to 22 km altitude with vertical extents of ~3 to 4 km.

[6] There were no DC-8 lidar measurements of ice PSCs in early December 1999. While the synoptic-scale temperatures were cold enough to sustain Type I PSCs, United Kingdom Meteorological Office (UKMO) analyses suggested that the synoptic conditions were too warm for ice PSC formation in early December 1999 [*Manney et al.*, 2003]. However, *Carslaw et al.* [1998, 1999], *Dörnbrack and Leutbecher* [2001], *Dörnbrack et al.* [2001] and others have shown that ice PSCs can form in the Arctic as a result of localized cooling associated with mesoscale mountain-wave activity. Therefore we used the locations of the DC-8 lidar Type Ia PSCs to initialize back trajectories for the three PSC events to determine whether the air parcels ever traveled through regions of mountain-wave activity prior to their detection.

3. Synoptic-Scale Back Trajectories

[7] We calculated 10-day back trajectories for the three NAT clouds observed in early December 1999 using the Goddard Space Flight Center (GSFC) isentropic trajectory model and 3.75° longitude × 2.50° latitude UKMO 1200 UTC temperature and wind data. We used the DC-8 lidar data to determine the starting points for the trajectories (15, 50, and 31 points for 5, 7, and 10 December, respectively) using a uniform grid (0.5 km vertical, 70 km horizontal) that covered the horizontal and vertical extent of each PSC. The synoptic-scale temperature history for each set of back trajectories is shown in Figure 3. The gray region in Figure 3 repre-

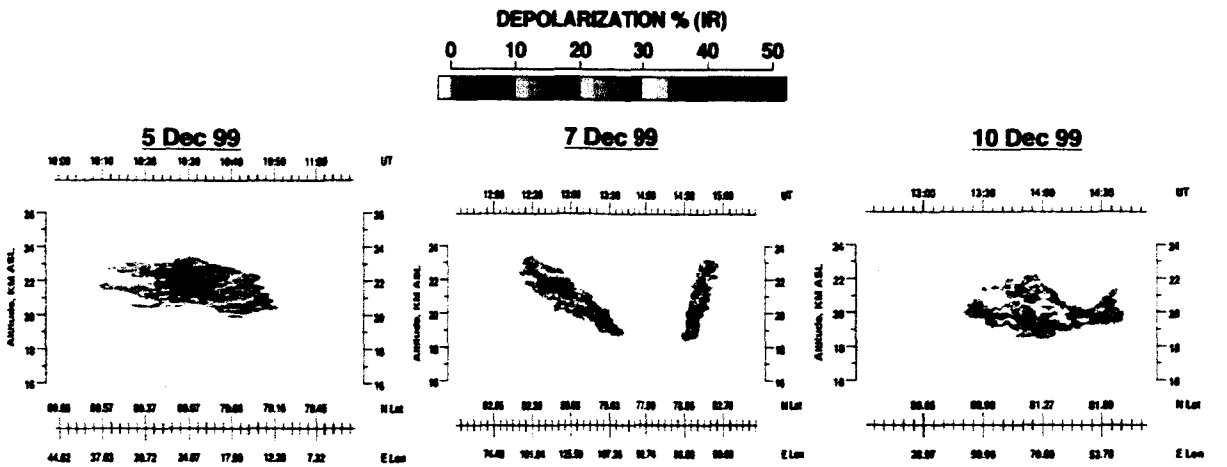

Figure 2. Infrared (1064 nm) DIAL lidar depolarization ratios for 5, 7, and 10 December 1999. High depolarization ratios and low scattering ratios (not shown) indicate these clouds were Type Ia (solid nitric acid) PSCs.

sents the range of synoptic-scale temperatures associated with all the trajectories, whereas the thick, colored line represents the mean synoptic-scale temperature history for each PSC event. The PSCs and the associated back trajectories were located in the region from ~30–50 hPa. The mean air parcel temperature for each PSC event cooled to below the NAT frost point (197.5 K at 50 hPa and 193.0 K at 30 hPa, assuming 10 ppbv HNO_3 and 5 ppmv H_2O) about 5 days prior to the lidar cloud measurements. At no time during the 10-day back trajectory period did the mean or minimum air parcel temperatures reach or drop below the ice frost point (188.4 K at 50 hPa and 185.5 K at 30 hPa, assuming 5 ppmv H_2O). Thus on the synoptic scale, there is no evidence that ice particles could have played a role in the formation of the Type Ia PSCs measured by the DC-8 lidar in early December 1999. This is in agreement with an analysis of synoptic-scale temperatures and PSC freezing processes by *Drdla et al.* [2003]. However, it is possible that cooling associated with mesoscale mountain-wave activity could lower the ambient air temperatures below the ice frost point. Therefore we compared the location of the back trajectories (Figure 5) with the AVHRR ice PSC map for the corresponding time period (Figure 4a) to determine if the air parcels traveled through regions of mountain-wave cloud activity at any time during the back trajectory period. The results of this comparison are discussed in the following section.

4. AVHRR Ice PSC Mapping

4.1. AVHRR Ice PSC Model

[8] The AVHRR instruments on board the National Oceanic and Atmospheric Administration (NOAA) polar-orbiting satellites have excellent spatial and temporal resolution at polar latitudes and have been collecting data continuously since 1979. The AVHRR is a five-channel, nadir-viewing, cross-track scanning radiometer with a horizontal resolution of 1.1 km at nadir [*Kidder and Vonder Haar*, 1995]. There are typically two AVHRR instruments in operation, and together they can collect upwards of eight passes per day for a given location at polar latitudes. The high spatial and temporal resolution of AVHRR data make them particularly useful for studying quickly evolving mesoscale wave-cloud events.

[9] *Pagan* [1996] and *Garcia et al.* [1995] determined that AVHRR channel 5 brightness temperatures (T_5) can be used to detect optically thick PSCs. *Foschi and Pagan* [2002] determined that the brightness temperature difference between AVHRR channels 4 and 5 (BTD) could be used to detect optically thin PSCs. Both of these studies concluded that the PSCs identified in AVHRR imagery were most likely composed of ice (Type II PSC). *Hervig et al.* [2001] developed a radiative transfer model that uses calibrated and georegistered AVHRR thermal infrared data (channel 4, 10.88 μm and channel 5, 11.94 μm) to identify PSCs. They simulated the AVHRR response to PSCs and concluded that Type I PSCs are invisible to AVHRR, whereas Type II (ice) PSCs are detectable for optical depths above ~0.05 to 0.10 for AVHRR thermal infrared wavelengths. They also determined that PSC and cirrus AVHRR signatures are similar, as they are both high, cold ice clouds. However, some differences between cirrus and PSCs exist; PSCs are colder, usually have lower optical depths, and have smaller particle sizes.

[10] *Hervig et al.* [2001] modeled simulations of the AVHRR response to ice PSCs and cirrus for a range of polar winter conditions (see Figure 12 in the work of *Hervig et al.* [2001] for an example). The modeled PSC and cirrus signals may overlap in some cases, and it was determined that using the cirrus maximum BTD (BTD_{max}) as a threshold to separate ice PSCs from cirrus would yield the most reliable method for identifying PSCs in AVHRR imagery. AVHRR T_5 versus BTD measurements were compared to the modeled ice PSC and cirrus signatures. Ice PSCs are indicated for AVHRR BTD > cirrus BTD_{max}. Using the modeled cirrus BTD_{max} as a threshold to separate cirrus and ice PSCs yields a conservative estimate of ice PSC occurrence.

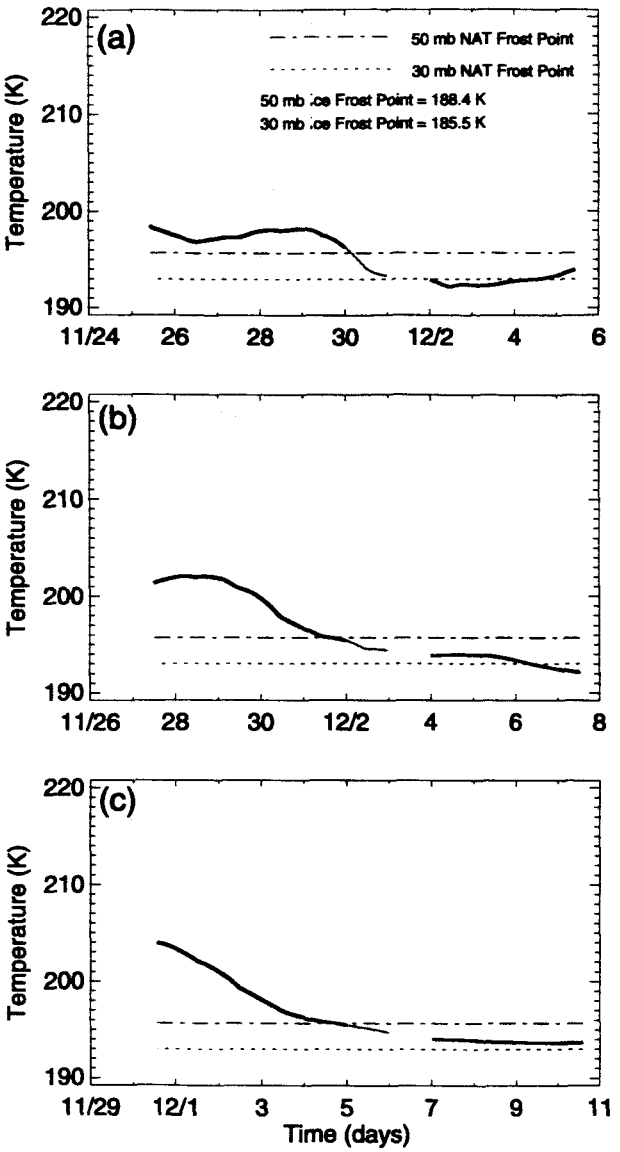

Figure 3. Temperature histories for 10-day back trajectories starting on: (a) 5 December; (b) 7 December; and (c) 10 December 1999. Back trajectories were initialized at the PSC locations shown in Figure 2. The number of trajectories for each PSC is: 15, 50, and 31 for 5, 7, and 10 December, respectively. The gray regions on each plot represent the temperature range for all the trajectories, whereas the thick, colored line represents the mean temperature for all the trajectories. Each color represents one day, as shown on the abscissa. NAT and ice frost points for 30 and 50 hPa were calculated using 5 ppmv H_2O and 10 ppbv HNO_3.

[11] In this study, we used the *Hervig et al.* [2001] AVHRR ice PSC model. Daily T_5 and BTD maps were created from AVHRR 4-km thermal infrared data from the NOAA-14 and NOAA-15 satellites. The T_5 and BTD maps were created by combining all available AVHRR passes for each day. Where pixels overlapped, the minimum T_5 and maximum BTD were chosen as they represent the strongest ice PSC signature. The model also used daily surface temperature (T_{sfc}) and tropopause temperature (T_{trop}) maps. We produced the T_{sfc} maps by interpolating National Center for Environmental Prediction (NCEP) 2.5° × 2.5° daily mean surface temperature reanalysis data to the 4-km AVHRR pixel locations. The T_{trop} maps were produced from 3.75° longitude × 2.5° latitude UKMO 1200 UTC pressure and temperature analysis data. A value of 2.0 potential vorticity units (PVU) was used to identify the tropopause [*Pfister et al.*, 2003]. The T_{trop} data were then interpolated to the 4-km AVHRR pixel locations.

[12] The *Hervig et al.* [2001] AVHRR ice PSC mapping model is a two-step process. First, to identify optically thick ice PSCs, AVHRR T_5 data are compared with UKMO T_{trop} and maximum stratospheric ice frost point temperature (T_{ice}) data on a pixel by pixel basis. In this study, a maximum T_{ice} was calculated assuming a pressure of 150 hPa and 5ppmv H_2O, which yielded a value of ~195 K. AVHRR pixels with $T_5 < T_{trop}$ and BTD > 2.0 or $T_5 < T_{ice}$ and BTD > 2.0 are mapped as ice PSCs. Using the condition BTD > 2.0 eliminates the confusion of cold high clouds with cold earth surfaces, such as ice sheets or sea ice, that have BTDs near zero [*Foschi and Pagan*, 2002]. As the majority of PSCs are optically thin and AVHRR is a nadir-viewing instrument, this step identifies only a small fraction of ice PSCs. For optically thin clouds, AVHRR T_5 is a combination of the cloud and upwelling radiation from below, resulting in a T_5 that is usually warmer than the actual cloud top temperature.

[13] The second step in the model uses BTDs to identify optically thin ice PSCs. In this study, we modeled BTDs for a 2-km thick cirrus layer located at the tropopause, using T_{trop} to estimate the cirrus temperature and T_{sfc} to estimate the underlying surface temperature. We confined T_{trop} to 205 K or the UKMO tropopause temperature, whichever was lower, to assure a realistic but conservative temperature for a tropopause cirrus layer located within the polar vortex. The model yields a series of cirrus BTD curves for each pixel combination of T_{trop} and T_{sfc} that are then compared, pixel by pixel, with AVHRR BTD and T_5 data. AVHRR pixels with BTD > cirrus BTD_{max} are confidently categorized as "ice PSCs." Those pixels with BTD > cirrus BTD_{mean} are labeled as "probable ice PSCs," and pixels with BTD > cirrus BTD_{min} are labeled as "probable tropopause cirrus." Pixels with BTD < cirrus BTD_{min} are labeled as "no PSC." This information is summarized in Table 1, along with the color-coding used for the ice PSC maps described in the next section.

4.2. AVHRR Ice PSC Map and UKMO Back Trajectory Comparisons

[14] Composite AVHRR ice PSC maps for each of the three Type Ia PSC events and associated 10-day back trajectory periods were created. For example, for the 5 December PSC event, we composited the daily ice PSC maps for the period 25 November to 5 December 1999. Where PSC pixels overlapped, we chose the strongest ice PSC signal (i.e., where the criteria in Table 1, from top to bottom, represent the strongest to weakest signature) for that location during the entire 10-day period. These three composite maps showed very little evidence of ice PSCs. Thus we chose to further composite the maps to show ice PSC activity during the period 25 November to 10 December

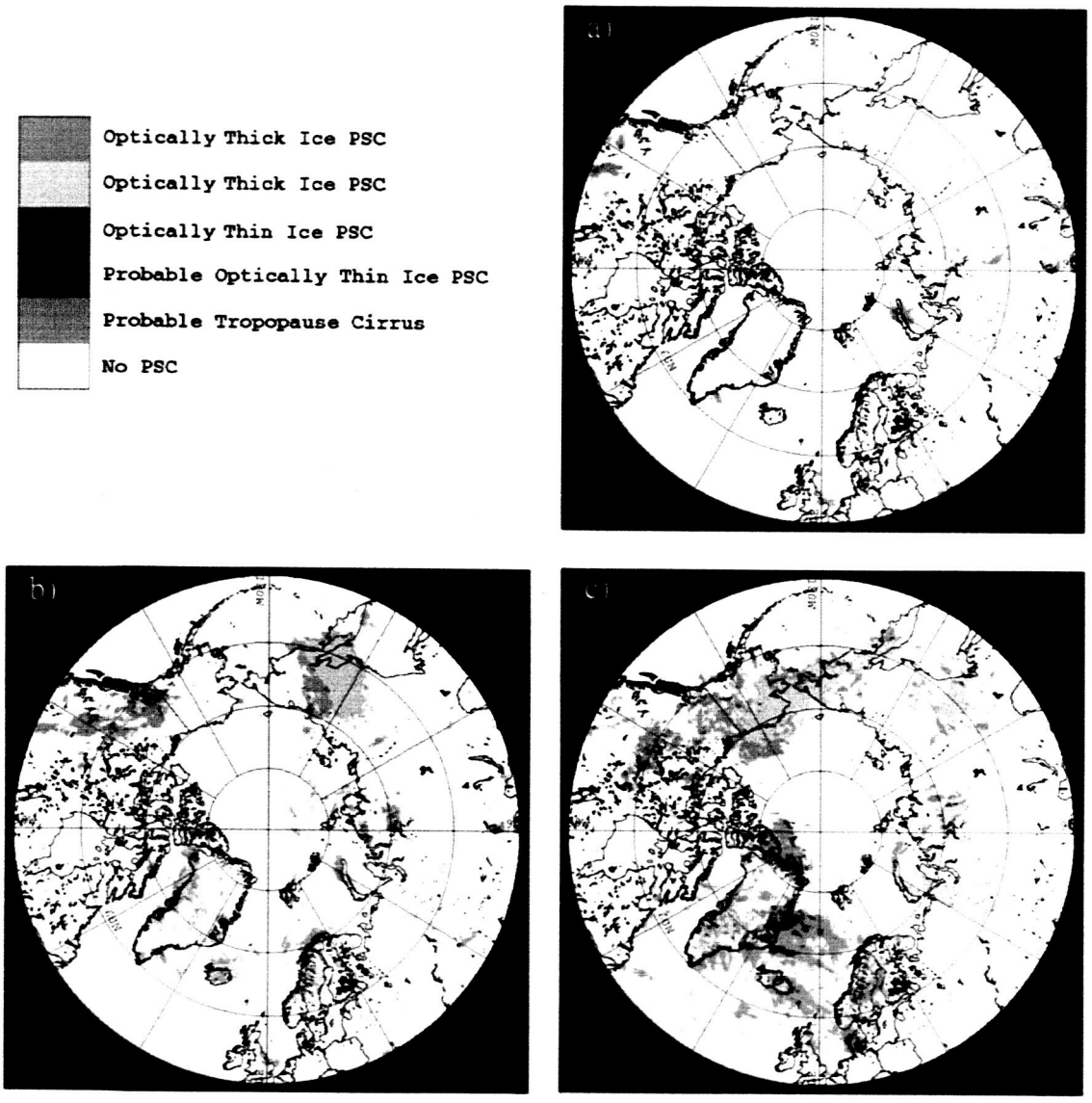

Figure 4. Composite AVHRR ice PSC map for: (a) 25 November to 10 December 1999; (b) 1 December–31 December 1999; and (c) 1 January–31 January 2000. When PSC events overlap during the composite period, the strongest PSC event is mapped. The ice PSC map color-coding is described in Table 1, and the ice PSC statistics are shown in Table 2.

1999 (Figure 4a). This period encompasses all three Type Ia PSC events and associated 10-day back trajectories. Such AVHRR ice PSC maps can represent ice PSCs formed by a variety of means (e.g., synoptic-scale uplift or diabatic cooling, mesoscale mountain-wave activity, nonorographic inertia-gravity waves, etc.). However, AVHRR is particularly suitable for mapping mesoscale mountain-wave cloud events where the rapid cooling produces a large number density of small ice particles that produce large BTDs [*Hervig et al.*, 2001]. Mountain-wave clouds are evidenced

Table 1. Summary of AVHRR Ice PSC Map Categories and Color-Coding

Color	Criteria	PSC Flag
Green	$T_5 < T_{ice}$ and BTD > 2.0	Optically Thick Ice PSC
Gray	$T_5 < T_{trop}$ and BTD > 2.0	Optically Thick Ice PSC
Red	BTD > cirrus BTD_{max}	Optically Thin Ice PSC
Blue	BTD > cirrus BTD_{mean}	Probable Optically Thin Ice PSC
Cyan	BTD > cirrus BTD_{min}	Probable Tropopause Cirrus
White	BTD < cirrus BTD_{min} and $T_5 > T_{trop}$	No PSC
Black	No AVHRR Data	No PSC

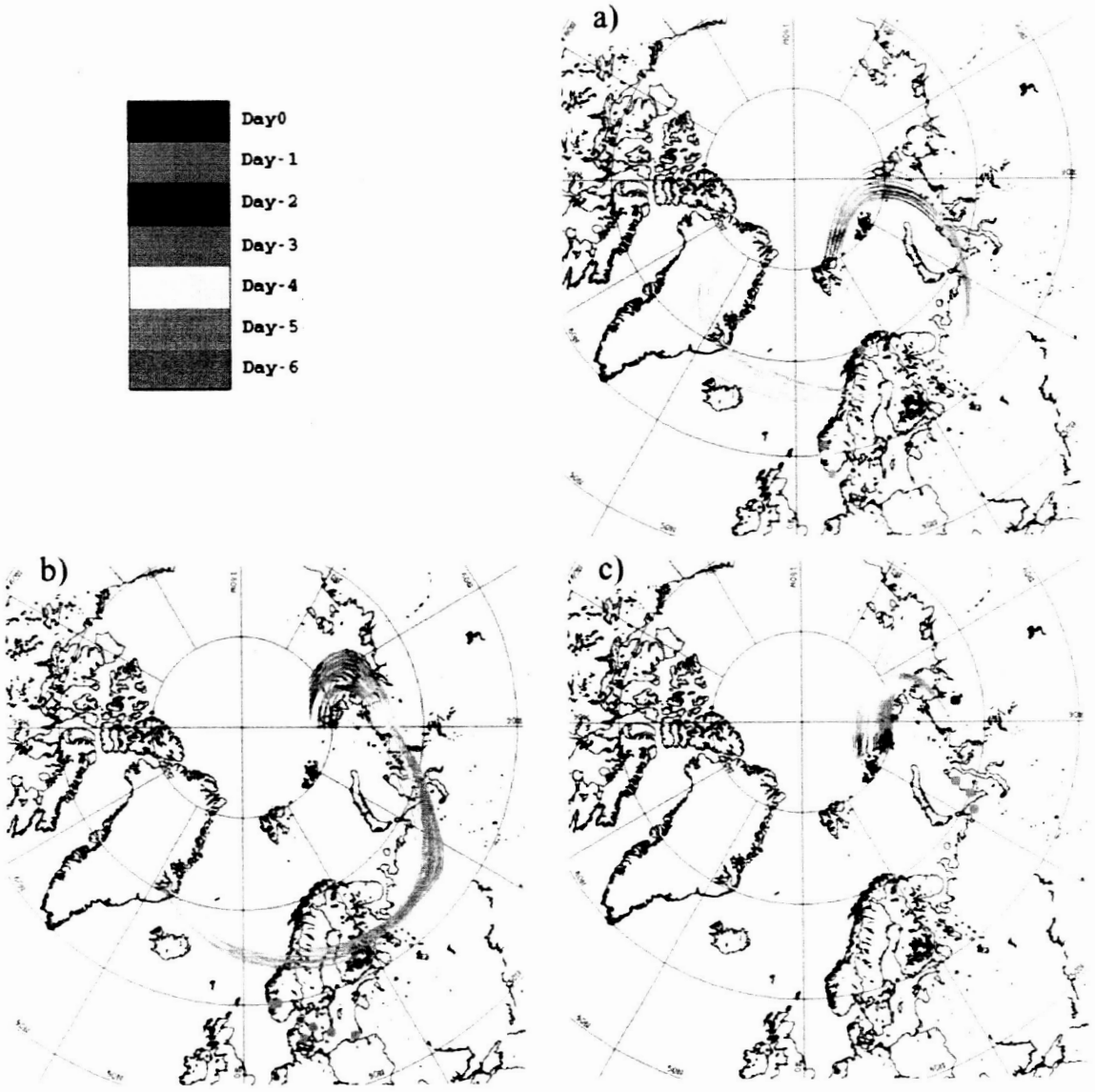

Figure 5. UKMO back trajectory paths and 0000 UTC grid box averaged MWFM-2 wave temperature amplitude hindcast data for locations with cooling below the ice frost point for: (a) 29 November to 5 December 1999; (b) 1 December to 7 December 1999; and (c) 4 December to 10 December 1999. Six-day back trajectories and MWFM-2 $T_{DAO} - T_{RMS} - T_{\sigma}$ data are overlaid in color: red, green, blue, cyan, yellow, orange, and pink indicate Day0 through Day-6, respectively. Note that the MWFM-2 points and back trajectory paths are color-coordinated. Thus for a MWFM-2 point to overlap temporally and spatially with a back trajectory path, they must have the same color. The only MWFM-2 $T_{DAO} - T_{RMS} - T_{\sigma} - 3$ K point (associated with cooling sufficient to lower the air temperature at least 3 K below the ice frost point) is indicated with a small black dot. All the MWFM-2 data points are located at 30 hPa.

in AVHRR as high cirrus or ice PSCs over and downwind of mountainous terrain.

[15] The ice PSC map shown in Figure 4a indicates that very little ice PSC activity occurred during 25 November to 10 December 1999. Some small regions of localized mountain-wave cloud activity were noted, for example, off the southeast coast of Greenland and over Novaya Zemlya. Our analysis shows that these mountain-wave clouds were most likely tropospheric (i.e., colored cyan, probable tropopause cirrus) with only a minimal number of pixels representing ice PSCs or probable ice PSCs (red and dark blue on the map). We compared the path of the back trajectories for each Type Ia PSC event (Figure 5) with the ice PSC locations in Figure 4a. In none of the three cases did the

Table 2. Statistics for Ice PSC Maps in Figure 4 for 25 November to 10 December 1999 (Figure 4a); 1 December to 31 December 1999 (Figure 4b); and 1 January to 31 January 2000 (Figure 4c)[a]

Color	PSC Flag	Figure 4a Coverage, %	Figure 4b Coverage, %	Figure 4c Coverage, %
Green	Optically Thick Ice PSC	<0.001	<0.001	<0.001
Gray	Optically Thick Ice PSC	0.004	2.542	4.304
Red	Optically Thin Ice PSC	0.002	0.076	0.148
Blue	Probable Optically Thin Ice PSC	0.038	0.314	0.923
Cyan	Probable Tropopause Cirrus	0.550	4.016	8.467
White	No PSC	99.407	93.051	86.158

[a]Coverage (%) is defined as the percentage of pixels that fall into each class within the region from 50° to 90°N.

air parcels travel through any category of ice PSCs prior to the lidar detection of the NAT clouds.

4.3. AVHRR and Mountain-Wave Cloud PSC Climatology Comparison

[16] *Dörnbrack et al.* [2001] compared Penn State/National Center for Atmospheric Research Mesoscale Model (MM5) mesoscale fields with European Center for Medium-Range Weather Forecasts (ECMWF) synoptic-scale analyses and remote sensing and in situ observations over northern Scandinavia for one month, January 1997. From this study, they developed a set of dynamic criteria for stratospheric mountain-wave cloud activity over Scandinavia based on low-level (900 hPa) wind speed and direction and the directional shear between low-level (900 hPa) and high-level (500 to 50 hPa) winds.

[17] *Dörnbrack and Leutbecher* [2001] used the dynamic criteria described above to develop a 20-year seasonal (1979–1980 to 1998–1999) climatology of potential PSC formation at 30, 50, and 70 hPa over Scandinavia. Based on an analysis of this 20-year climatology, they concluded that: (1) Type II PSCs are less likely to form than Type I PSCs; (2) Type II PSC formation was dominated by mesoscale cooling events on the order of 2–8 K; and (3) Type II PSCs have the highest potential to form in January and February and have the lowest potential for formation in December and March.

[18] Composite AVHRR ice PSC maps for 25 November to 10 December 1999, 1 December to 31 December 1999, and 1 January to 31 January 2000 are shown in Figure 4. PSC statistics for each of these maps are shown in Table 2. The AVHRR ice PSC statistics reveal that within the area from 50° to 90° N, ice PSCs (all categories on the map except for "Probable Tropopause Cirrus," colored cyan) covered ~0.05% of the region from 25 November to 10 December 1999, ~2.9% of the region in December 1999, and ~5.4% of the region in January 2000. These statistics represent areal coverage and not frequency, and they represent ice clouds for all levels in the stratosphere. PSC frequency for a given location can be determined by computing the number of times each pixel fell into an ice PSC category on each day during the period of interest. We did not attempt to do this analysis for this study. However, a visual inspection of the daily AVHRR ice PSC maps revealed that ice PSCs formed more often over Greenland and Scandinavia (regions associated with high-amplitude mountain-wave activity) during January 2000 than in December 1999.

[19] Although AVHRR has excellent temporal and horizontal resolution, it is difficult to determine the exact altitude of the ice PSCs. For optically thick PSCs, T_5 can be used as a conservative estimate of cloud top temperature and can therefore be compared to temperature analyses or radiosonde data to estimate the vertical position of the cloud. Determining the vertical placement of optically thin PSCs is more difficult. For these clouds, the *Hervig et al.* [2001] model uses the BTD criteria. We use a conservative value of T_{trop} (205 K or UKMO, whichever is less), and this ensures that the clouds mapped as ice PSCs are in the stratosphere. Future work on the AVHRR ice PSC model will include methods to estimate the temperature of optically thin ice PSCs, which will help to determine their altitude within the stratosphere.

[20] A direct comparison of the AVHRR ice PSC data with the ice PSC climatology data derived by *Dörnbrack and Leutbecher* [2001] is not possible. The AVHRR PSCs extend over a wider altitude range and a larger areal extent. The PSC mountain-wave climatology statistics are limited to northern Scandinavia and cover only 30–70 hPa. Furthermore, the AVHRR ice PSC statistics represent PSC areal coverage, whereas the PSC mountain-wave climatology statistics represent frequency of PSC formation potential. Nevertheless, the AVHRR ice PSC statistics show that a larger region of ice PSCs formed in January than in December (with a visual inspection of daily ice PSC maps indicating they also formed more often in January), which is in agreement with the trend in the ice PSC climatology statistics derived by *Dörnbrack and Leutbecher* [2001]. While the AVHRR ice PSC maps in Figure 4 represent a combination of PSC formation dynamics, there are regions of obvious mountain-wave cloud activity. These regions are in alignment with preferred regions of mountain-wave cloud activity for other PSC seasons, such as those shown by *Carslaw et al.* [1998], and show a marked increase from December to January.

5. AVHRR and MWFM-2 Type II PSC Comparisons

[21] To provide further evidence that the three Type Ia PSCs observed in early December 1999 did not form by heterogeneous nucleation of NAT on ice particles generated in mountain waves, we performed MWFM-2 hindcasts [*Eckermann and Preusse*, 1999; *Bacmeister et al.*, 1994; *Jiang et al.*, 2004] to identify locations where stratospheric mountain-wave activity was predicted to cool synoptic-scale temperatures below the ice frost point. We then overlaid the back trajectory paths on the MWFM-2 hindcast maps to determine whether the air parcels traveled through regions

of high-amplitude mountain-wave activity prior to the time the DC-8 lidar observed the NAT clouds.

[22] The MWFM uses a detailed parameterization approach to forecast/hindcast the geographical locations and amplitudes of mountain waves in the troposphere and stratosphere, as well as wave-induced effects such as turbulence or wave-cloud formation. Briefly, the MWFM "postprocesses" large-scale atmospheric winds and temperatures generated either by numerical weather prediction models (MWFM forecast mode) or data assimilation systems (MWFM hindcast mode) to estimate the subgrid-scale mountain wave content for a particular atmospheric environment. Surface winds are "blown" over a collection of diagnosed ridges which define major topographic structures over the globe relevant to mountain-wave forcing, and a set of forced mountain waves is generated. Wind and temperature profiles above the parent ridge are then used to model the radiation of these mountain waves away from the ridge feature, including tracking of wave amplitudes along the wave's group propagation path.

[23] *Bacmeister et al.* [1994] describe the formulation and first results of Version 1 of the model (MWFM-1), which used a two-dimensional hydrostatic irrotational gravity wave formation. In this study, we use Version 2 of the MWFM (MWFM-2), which employs a three-dimensional nonhydrostatic rotational ray-tracing formulation to more accurately specify both horizontal and vertical group propagation of wave energy away from parent ridges. The MWFM-2 was used to forecast mountain waves during SOLVE-THESEO 2000 and was used by *Hertzog et al.* [2002] to hindcast and study a stratospheric mountain wave measured by balloon over southern Scandinavia on 2 March 2000.

[24] Whereas MWFM-1 generates a single plane hydrostatic wave over any given ridge feature, MWFM-2 launches a collection of rays of different horizontal wavenumbers and wave azimuths from each parent ridge. The raw hemispheric ray data generated by MWFM-2 are voluminous and, as such, can be impractical for certain applications. For example, *Pierce et al.* [2003] chose to average the raw ray data from MWFM-2 hindcasts of wave temperature amplitudes in their chemical transport model (CTM) study in order to yield a more tractable mean mountain wave contribution within a grid box that could be easily ingested into their CTM calculations. Their approach was to compute root mean square (r.m.s.) peak mountain-wave temperature amplitudes, T_{RMS}, as well as standard deviations based on all the MWFM-2 ray data at a given altitude within a given 1° × 1° grid box, T_σ, as hindcast by MWFM-2 using the NASA Data Assimilation Office (DAO) 0000 UTC analyses. We used the same grid box averaged MWFM-2 data as described above (also see section 6 of *Pierce et al.* [2003]) to characterize a mean mountain-wave temperature perturbation within each 1° × 1° grid box for pressure levels ranging from 100 to 10 hPa. The ray launch parameters we used follow those described in section 3.2.3 of *Hertzog et al.* [2002], except we used two instead of three different horizontal wavenumbers, launched at 18 azimuths successively rotated by 10° to span a full 180° downwind of the ridge axis (see also *Jiang et al.* [2004]).

[25] We calculated ice frost point temperatures for 30, 40, and 50 hPa (assuming 5 ppmv H_2O), corresponding to the range of pressure levels for the three NAT clouds and associated back trajectories. We used the grid box averaged MWFM-2 0000 UTC hindcast wave temperature amplitude data along with DAO 0000 UTC mean temperature analysis data (T_{DAO}) to locate regions of predicted ice PSC formation from 50° to 90°N. First, we computed $T_{DAO} - T_{RMS}$ values for the period 25 November to 10 December 1999. No day during that time period experienced sufficient mountain-wave activity to cool the air below the ice frost point. This result is in agreement with the AVHRR results discussed previously, which showed no evidence of ice PSCs at or downwind of mountainous terrain.

[26] Next, to investigate a broader set of possible mountain-wave cooling events, we computed $T_{DAO} - T_{RMS} - T_\sigma$ for the same time period. This yielded only 16 data points (all at 30 hPa), with almost half (seven) occurring on 1 December 1999. These data points were plotted along with the 6-day back trajectory paths for each of the three PSC events in early December 1999 (Figure 5). We used 6-day back trajectories because, in these three cases, the synoptic-scale temperatures were too warm to sustain a Type Ia PSC formed more than 6 days earlier. Note that the circles in Figure 5 which represent locations where grid box averaged MWFM-2 data predict mountain-wave cooling below the ice frost point are color-coordinated with the back trajectory paths. Thus for a trajectory path to overlap a MWFM-2 point in time and space, they must have the same color. A visual inspection of the back trajectory and grid box averaged MWFM-2 wave temperature amplitude data in Figure 5 shows virtually no spatial or temporal correlation between the two data sets. None of the back trajectory data overlaps a MWFM-2 point, and the nearest coincidence is at least 500 km away and occurs on only 2 days.

[27] *Carslaw et al.* [1998] and *Chang et al.* [1999] have suggested that air temperatures need to drop 3 to 4 K below the ice frost point for ice nucleation to occur. Thus we subtracted 3 K from the grid box averaged MWFM-2 $T_{DAO} - T_{RMS} - T_\sigma$ data to determine if any of the mountain-wave cooling events described above were sufficient to initiate ice nucleation. Only one data point, on 1 December 1999, met this criterion and is noted in Figure 5 as a yellow or pink circle with a black dot.

[28] The results of the comparisons between the synoptic-scale back trajectory data and the grid box averaged MWFM-2 wave temperature amplitude hindcast data (for all three scenarios: $T_{DAO} - T_{RMS}$, $T_{DAO} - T_{RMS} - T_\sigma$, and $T_{DAO} - T_{RMS} - T_\sigma - 3$ K) show that mountain-wave activity was not sufficient to produce cooling to or below the ice frost point needed to initiate Type II PSC formation. These results are in agreement with our AVHRR ice PSC analysis.

[29] We explored the possibility that the grid box averaged MWFM-2 wave temperature amplitude data used above may not be the most appropriate metric to predict ice formation. The grid box averaging procedure can eliminate much of the structure and variability contained within the original hindcast, particularly when there are a large number of rays in a given grid box that have tiny amplitudes. Thus depending upon the spectrum of waves present at a location, the coldest local temperatures, which

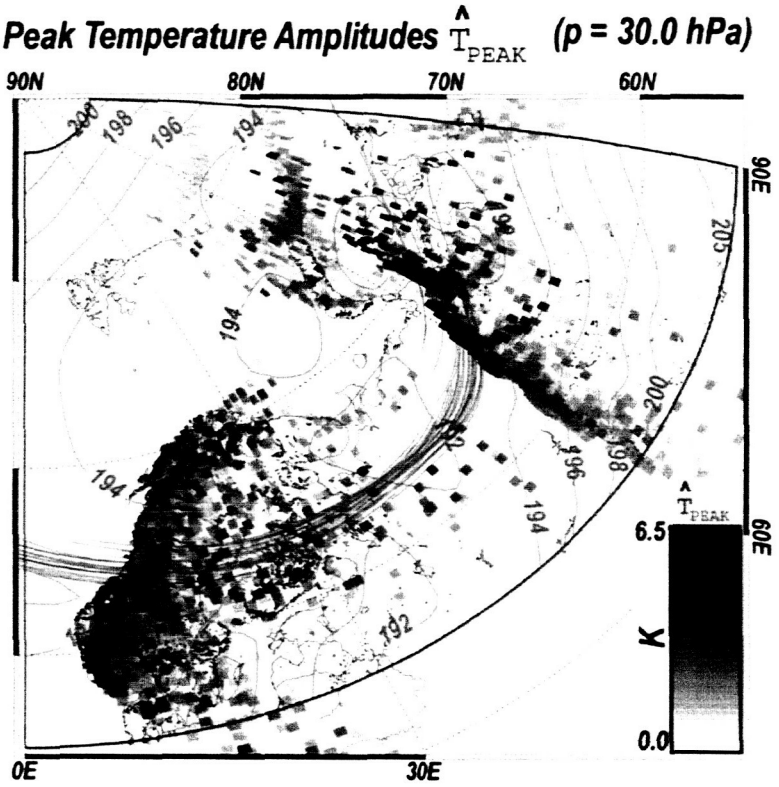

Figure 6. MWFM-2 hindcast of peak mountain wave temperature amplitudes at 30 hPa on 1 December 1999 at 1200 UTC, derived from the DAO "first-look" analysis. Each square pixel (width 0.5° × 1°) represents the group location and amplitude of a mountain wave ray (see attached color bar; scale is linear). Pixels are plotted in order of ascending amplitude; thus in regions with many colocated rays, the largest amplitude rays are plotted on top of the smaller amplitude ones, since only the largest amplitude rays are significant microphysically. Synoptic-scale DAO analysis temperatures (K) are contoured in cyan, while trajectories for this date from Figure 5b are overplotted in green. Red border shows the region within which MWFM-2 performed a forecast.

are most relevant to the ice formation potential, could potentially be more extreme than $T_{DAO} - T_{RMS} - T_{\sigma}$.

[30] For the period 25 November to 10 December, the grid box averaged data had the strongest signature for mountain-wave cooling sufficient to lower the synoptic-scale temperatures to or below the ice frost point on 1 December 1999. We analyzed 0000 and 1200 UTC MWFM-2 raw (unaveraged) hemispheric ray hindcast data for 1 December 1999 and then compared the raw data with the grid box averaged data for that day. MWFM-2 produces a voluminous output of raw hemispheric ray data, which makes a point-by-point comparison of these data with AVHRR and back trajectory data impractical. Rather, we generated hindcast maps of peak temperature amplitudes (similar to those shown in Figure 8 of *Hertzog et al.* [2002]) at 30, 40, and 50 hPa and compared them with our earlier trajectory analyses. The 30 hPa hindcast of peak temperature amplitudes for 1 December 1999 at 1200 UTC is shown in Figure 6, for a geographical subregion corresponding to the location of the back trajectory data for this date. The 1 December locations of the back trajectories corresponding to the 7 December 1999 Type Ia PSC are shown in green in Figure 6. The largest peak amplitude temperature cooling at 1200 UTC for 1 December at 30 hPa was ~6.5 K (dark red and black on the temperature color scale in Figure 6). The majority of the pixels (rays) show cooling less than 6.0 K. We then compared the ice frost point temperature for 30 hPa (185.5 K, using 5ppmv H_2O) with the 1200 UTC DAO temperature field (cyan contours on Figure 6). We determined that there was not sufficient mountain-wave cooling to lower the synoptic-scale temperatures below the ice frost point. Furthermore, an additional 3–4 K cooling would be needed to initiate ice nucleation. Similar comparisons of 1200 UTC MWFM-2 peak temperature amplitude data with 1200 UTC DAO synoptic scale temperatures for 40 and 50 hPa yielded the same conclusion. We also note that the 1 December locations of the back trajectories corresponding to the 5 December 1999 Type Ia PSC (Figure 5a) are located slightly north of the trajectories shown in Figure 6. Thus our discussion above also holds true for the 5 December 1999 PSC event.

[31] The grid box averaged MWFM-2 wave temperature amplitude hindcast data for 0000 UTC on 1 December 1999 (Figures 5a and 5b) did show seven locations where mountain-wave activity cooled the air temperature below the ice frost point, of which one location was at least 3 K

below the ice frost point. We compared the back trajectory locations for 1 December with the 0000 UTC MWFM-2 raw (unaveraged) hemispheric ray hindcast data for 30, 40, and 50 hPa and determined that the 0000 UTC MWFM-2 raw data also showed cooling below the ice frost point in roughly the same region as shown in Figures 5a and 5b, with only a few locations at 30 hPa with cooling at least 3 K below the ice frost point. As was the case with the grid box averaged MWFM-2 wave temperature amplitude data shown in Figures 5a and 5b, the small regions of localized cooling in the raw data were ~500 km south of the back trajectories.

[32] The results of the analysis of MWFM-2 hindcast data, using both the raw hemispheric ray data and the grid box averaged data, show strong evidence that ice particles formed in regions of mountain-wave activity in the stratosphere were not a factor in the formation of the three NAT clouds measured by the DC-8 lidar in early December 1999. When compared with back trajectory locations, the cooling associated with mountain-wave activity in early December was not sufficient to lower synoptic-scale temperatures to or below the ice frost point and initiate ice nucleation. It is likely that the grid box averaged MWFM-2 hindcast data underestimates the mountain-wave cooling, whereas the raw hemispheric ray data better match or slightly overestimate the wave cooling [e.g., *Eckermann and Preusse*, 1999; *Hertzog et al.*, 2002]. Thus it is likely that the actual cooling associated with mountain-wave activity is somewhere between these two limits. In our case, both MWFM hindcast data sets show insufficient cooling to initiate ice clouds and are therefore in agreement with the AVHRR data which show no evidence of ice PSCs at or close to the three NAT cloud back trajectory locations.

6. Discussion and Conclusions

[33] The analysis presented in this paper shows strong evidence that the three Type Ia PSCs measured by the DC-8 lidar in the Arctic vortex during early December 1999 were not formed as a result of heterogeneous nucleation of NAT on ice particle surfaces in regions of stratospheric mountain-wave activity. The analysis of AVHRR data showed scant evidence of ice PSC formation during 25 November to 10 December 1999. The AVHRR ice PSCs statistics for this period are in agreement with ice PSC climatology statistics derived by *Dörnbrack and Leutbecher* [2001]. Comparisons of AVHRR ice PSC locations with UKMO back trajectories initialized at locations where the DC-8 lidar observed the NAT clouds show no evidence that the air passed through regions of Type II PSCs formed by stratospheric mountain-wave activity prior to the NAT cloud observations. Furthermore, an analysis of MWFM-2 hindcast wave temperature amplitude data did not show evidence of sufficient cooling to lower synoptic-scale temperatures to or below the ice frost point to initiate ice nucleation.

[34] Based on our analysis, we conclude that Type Ia PSCs can nucleate in relatively warm synoptic-scale temperature fields and are not limited to forming at or downwind of regions of strong mountain-wave activity with sufficient cooling to produce ice nuclei. Our conclusion does not concur with a prevailing theory that Type Ia PSCs only form, or most likely form, by heterogeneous nucleation of NAT on ice particles in regions of stratospheric mountain-wave activity [*Carslaw et al.*, 1998, 1999; *Zondlo et al.*, 2000; *Füglistaler et al.*, 2002a, 2002b; *Dhaniyala et al.*, 2002; *Luo et al.*, 2003; *Voight et al.*, 2003.]

[35] *Hitchman et al.* [2003] suggest that the Type Ia PSC detected on 7 December 1999 was formed due to cooling associated with nonorographic inertia-gravity waves generated by breaking synoptic-scale tropospheric Rossby waves along the polar front jet, which propagate into the stratosphere. We generated MWFM-2 raw hemispheric ray hindcast data for 7 December 1999 and overlaid DAO synoptic-scale temperatures on the MWFM-2 maps. The MWFM-2 raw data showed no evidence of mountain-wave activity in the region of the observed Type Ia PSC. The cooling associated with the inertia-gravity wave described by *Hitchman et al.* [2003] was at most ~3 K. The 7 December DAO synoptic-scale temperature fields for 30, 40, and 50 hPa at the location of the observed Type Ia PSC were ~4–7 K above the ice frost point temperature. Thus cooling on the order of ~3 K would not be sufficient to lower the synoptic-scale temperatures to, or 3 K below, the ice frost point. While nonorographic inertia-gravity waves may play a role in the generation of Type Ia PSCs, in this case, the Type Ia PSC observed on 7 December 1999 did not form by heterogeneous nucleation of NAT on ice particles, but rather by some other nucleation mechanism.

[36] It is beyond the scope of this paper to provide a detailed analysis of other nucleation mechanisms that might be responsible for the formation of the three NAT clouds observed in the Arctic vortex in early December 1999. However, we provide a brief summary of possible nucleation mechanisms as follows.

[37] We explored the possibility of homogeneous freezing as a mechanism for the formation of the three NAT clouds. We calculated hourly solid particle production rates for volume-based nucleation modes [*Salcedo et al.*, 2001] and surface-based nucleation modes [*Tabazadeh et al.*, 2002]. The synoptic-scale trajectories shown in Figure 3 indicate that the air parcels spent roughly five days in the mean temperature range of 192–195 K for all three PSCs. In this temperature range, and at pressures ranging from 30–50 hPa, neither the *Salcedo et al.* [2001] homogeneous volume nucleation rates nor the *Tabazadeh et al.* [2002] surface nucleation rates can produce solid NAD particles. Further calculations showed that temperatures would need to lower to 189 K (at 30 hPa) and 191 K (at 50 hPa) for homogeneous nucleation to begin. The surface-based nucleation mode would require a few hours of air mass exposure at these lower temperatures to yield a sufficient number of NAD nuclei in the air for the lidar to observe the particles; the volume-based nucleation mode would require several days' exposure at these lower temperatures to yield a cloud. The lower temperatures needed for NAD particle production may be explained by temperature uncertainties in the synoptic-scale temperature analyses and back trajectory calculations or by small-amplitude mesoscale fluctuations. We note that direct homogeneous nucleation of NAT based on current nucleation rates [*Salcedo et al.*, 2001; *Tabazadeh et al.*, 2002] is insufficient by itself to produce enough solid particles in the air for lidar to detect these Type Ia PSCs. Thus based on the discussion above, taking temperature uncertainties and

small-amplitude mesoscale fluctuations into account, surface-based homogeneous nucleation of NAD particles that later on convert to NAT cannot be excluded as a possible mechanism for the formation of the three Type Ia PSCs observed in early December 1999.

[38] Other possibilities for NAT cloud formation may include heterogeneous nucleation on exotic solid nuclei [*Drdla et al.*, 2003; *Tolbert and Toon*, 2001]. However, no published rates are currently available to quantitatively determine if heterogeneous nucleation on exotic nuclei can explain the occurrence of these clouds in early winter.

[39] Whatever nucleation process was responsible for the formation of the three NAT clouds in the relatively warm synoptic-scale environment in early December 1999 should also operate efficiently when synoptic-scale temperature fields are significantly colder, such as in January 2000. We have provided strong evidence that heterogeneous nucleation of NAT on ice particles generated in regions of mountain-wave activity cannot be the sole mechanism for Type Ia PSC formation in the Arctic vortex. We plan to repeat our analysis technique for January 2000 to determine what percentage of Type Ia PSCs observed during the SOLVE campaign can be linked to mountain-wave activity upstream. Furthermore, *Strawa et al.* [2002] have developed a method to discriminate Type Ia from Type Ib PSCs in Polar Ozone and Aerosol Measurement (POAM) data. This method is also applicable to Stratospheric Aerosol and Gas Experiment (SAGE) data as well. These data sets can provide a long-term record of Type Ia PSCs that can be analyzed using AVHRR ice PSC data and back trajectory data to help determine whether ice particles generated in regions of mountain-wave activity play a dominant role in the formation of NAT clouds in the Arctic vortex.

[40] **Acknowledgments.** This work was supported by the NASA ACMAP and the NASA UARS projects. The AVHRR data were acquired through the NOAA Satellite Active Archive. We thank Leonhard Pfister for the many helpful conversations regarding various aspects of this paper.

References

Bacmeister, J. T., P. A. Newman, B. L. Gary, and K. R. Chan (1994), An algorithm for forecasting mountain wave-related turbulence in the stratosphere, *Weather Forecasting*, *9*, 241–253.

Browell, E. V., et al. (1990), Airborne lidar observations in the wintertime Arctic stratosphere: Polar stratospheric clouds, *Geophys. Res. Lett.*, *17*(4), 385–388.

Carslaw, K. S., M. Wirth, A. Tsias, B. P. Luo, A. Dörnbrack, M. Leutbecher, H. Volkert, W. Renger, J. T. Bacmeister, and T. Peter (1998), Particle microphysics and chemistry in remotely observed mountain polar stratospheric clouds, *J. Geophys. Res.*, *103*(D5), 5785–5796.

Carslaw, K. S., T. Peter, J. T. Bacmeister, and S. D. Eckermann (1999), Widespread solid particle formation by mountain waves in the Arctic stratosphere, *J. Geophys. Res.*, *104*(D1), 1827–1836.

Chang, H. A., T. Koop, L. T. Molina, and M. J. Molina (1999), Phase transition in emulsified HNO_3/H_2O and $HNO_3/H_2SO_4/H_2O$ solutions, *J. Phys. Chem.*, *103*, 2673–2679.

Dhaniyala, S., K. A. McKinney, and P. O. Wennberg (2002), Lee-wave clouds and denitrification of the polar stratosphere, *Geophys. Res. Lett.*, *29*(9), 1322, doi:10.1029/2001GL013900.

Dörnbrack, A., and M. Leutbecher (2001), Relevance of mountain wave cooling for the formation of polar stratospheric clouds over Scandinavia: A 20 year climatology, *J. Geophys. Res.*, *106*(D2), 1583–1593.

Dörnbrack, A., M. Leutbecher, J. Reichardt, A. Behrendt, K. Müller, and G. Baumgarten (2001), Relevance of mountain wave cooling for the formation of polar stratospheric clouds over Scandinavia: Mesoscale dynamics and observations for January 1997, *J. Geophys. Res.*, *106*(D2), 1569–1581.

Drdla, K., M. R. Schoeberl, and E. V. Browell (2003), Microphysical modeling of the 1999–2000 Arctic winter: 1. Polar stratospheric clouds, denitrification, and dehydration, *J. Geophys. Res.*, *108*(D5), 8312, doi:10.1029/2001JD000782.

Eckermann, S. D., and P. Preusse (1999), Global measurements of stratospheric mountain waves from space, *Science*, *286*, 1534–1537.

Foschi, P. G., and K. L. Pagan (2002), Toward a polar stratospheric cloud climatology using advanced very high resolution radiometer thermal infrared data, *Can. J. Remote Sens.*, *28*(2), 187–195.

Füglistaler, S., B. P. Luo, C. Voight, K. S. Carslaw, and T. Peter (2002a), NAT-rock formation by mother clouds: A microphysical model study, *Atmos. Chem. Phys.*, *2*, 93–98.

Füglistaler, S., et al. (2002b), Large NAT particle formation by mother clouds: Analysis of SOLVE/THESEO-2000 observations, *Geophys. Res. Lett.*, *29*(12), 1610, doi:10.1029/2001GL014548.

Garcia, O., K. L. Pagan, P. G. Foschi, S. Gaines, and R. S. Hipskind (1995), Detection of polar stratospheric clouds over Antarctica using AVHRR images obtained at Palmer Station during August 1992, *Polar Rec.*, *31*, 211–226.

Hertzog, A., F. Vial, A. Dörnbrack, S. D. Eckermann, B. M. Knudsen, and J. P. Pommereau (2002), In situ observations of gravity waves and comparisons with numerical simulations during the SOLVE/THESEO 2000 campaign, *J. Geophys. Res.*, *107*(D20), 8292, doi:10.1029/2001JD001025.

Hervig, M. E., K. L. Pagan, and P. G. Foschi (2001), Analysis of PSC measurements from AVHRR, *J. Geophys. Res.*, *106*(D10), 10,363–10,374.

Hitchman, M. H., M. L. Bucker, G. J. Tripoli, E. V. Browell, W. B. Grant, T. J. McGee, and J. F. Burris (2003), Nonorographic generation of Arctic polar stratospheric clouds during December 1999, *J. Geophys. Res.*, *108*(D5), 8325, doi:10.1029/2001JD001034.

Jiang, J. H., S. D. Eckermann, D. L. Wu, and J. Ma (2004), A search for mountain waves in MLS stratospheric limb radiance from the Northern Hemisphere: Data analysis and global mountain wave modeling, *J. Geophys. Res.*, *109*, doi:10.1029/2003JD003974, in press.

Kidder, S. Q., and T. H. Vonder Haar (1995), Meteorological satellite instrumentation, in *Satellite Meteorology: An Introduction*, pp. 87–97, Academic, San Diego, Calif.

Luo, B. P., C. Voight, S. Füglistaler, and T. Peter (2003), Extreme NAT supersaturation in mountain wave ice PSCs: A clue to NAT formation, *J. Geophys. Res.*, *108*(D15), 4441, doi:10.1029/2002JD003104.

Manney, G. L., et al. (2003), Lower stratospheric temperature differences between meteorological analyses in two cold Arctic winters and their impact on polar processing studies, *J. Geophys. Res.*, *108*(D5), 8328, doi:10.1029/2001JD001149.

Pagan, K. L. (1996), Detection of polar stratospheric clouds over Antarctica using AVHRR satellite imagery, M.S. thesis, San Francisco State Univ., San Francisco, Calif.

Pfister, L. H., et al. (2003), Processes controlling water vapor in the winter Arctic tropopause region, *J. Geophys. Res.*, *108*(D5), 8314, doi:10.1029/2001JD001067.

Pierce, R. B., et al. (2003), Large-scale chemical evolution of the Arctic vortex during the 1999/2000 winter: HALOE/POAM III Lagrangian photochemical modeling for the SAGE III Ozone Loss and Validation Experiment (SOLVE) campaign, *J. Geophys. Res.*, *108*(D5), 8317, doi:10.1029/2001JD001063.

Salcedo, D., L. T. Molina, and M. J. Molina (2001), Homogeneous freezing of concentrated aqueous nitric acid solutions at polar stratospheric temperatures, *J. Phys. Chem.*, *105*(9), 1433–1439.

Strawa, A. W., et al. (2002), Discriminating Types Ia and Ib polar stratospheric clouds in POAM satellite data, *J. Geophys. Res.*, *107*(D20), doi:10.1029/2001JD000458.

Tabazadeh, A., O. B. Toon, B. L. Gary, J. T. Bacmeister, and M. R. Schoeberl (1996), Observational constraints on the formation of Type Ia polar stratospheric clouds, *Geophys. Res. Lett.*, *23*(16), 2109–2112.

Tabazadeh, A., E. J. Jensen, O. B. Toon, K. Drdla, and M. R. Schoeberl (2001), Role of the stratospheric polar freezing belt in denitrification, *Science*, *291*, 2591–2594.

Tabazadeh, A., Y. S. Djikaev, P. Hamill, and H. Reiss (2002), Laboratory evidence for surface nucleation of solid polar stratospheric cloud particles, *J. Phys. Chem.*, *106*, 10,238–10,246.

Teitelbaum, H., M. Moustaoui, and M. Fromm (2001), Exploring polar stratospheric cloud and ozone minihole formation: The primary importance of synoptic-scale flow perturbations, *J. Geophys. Res.*, *106*(D22), 28,173–28,188.

Tolbert, M. A., and O. B. Toon (2001), Atmospheric science: Enhanced: Solving the PSC mystery, *Science*, *292*, 61–63.

Toon, O. B., A. Tabazadeh, E. V. Browell, and J. Jordan (2000), Analysis of lidar observations of Arctic polar stratospheric clouds during January 1989, *J. Geophys. Res.*, *105*(D16), 20,589–20,615.

Voight, C., et al. (2003), In situ mountain-wave polar stratospheric cloud measurements: Implications for nitric acid trihydrate formation, *J. Geophys. Res.*, *108*(D5), 8331, doi:10.1029/2001JD001185.

World Meteorological Organization (2003), Scientific assessment of ozone depletion: 2002, *Rep. 47*, 498 pp., Global Ozone Res. and Monit. Proj., Geneva.

Zondlo, M. A., P. K. Hudson, A. J. Prenni, and M. A. Tolbert (2000), Chemistry and microphysics of polar stratospheric clouds and cirrus clouds, *Annu. Rev. Phys. Chem.*, *51*, 473–499.

E. V. Browell, NASA Langley Research Center, Mail Stop 401A, Hampton, VA 23681-2199, USA. (edward.v.browell@nasa.gov)

K. Drdla and A. Tabazadeh, NASA Ames Research Center, MS 245-4, Moffett Field, CA 94035-1000, USA. (katja.drdla-1@nasa.gov; azadeh.tabazadeh-1@nasa.gov)

S. D. Eckermann, Middle Atmospheric Dynamic Section, E. O. Hulbert Center for Space Research, Naval Research Laboratory, Code 7646, Washington, DC 20375-5352, USA. (stephen.eckermann@nrl.navy.mil)

P. G. Foschi, Romberg Tiburon Center for Environmental Studies, San Francisco State University, 3152 Paradise Drive, Tiburon, CA 94920-1205, USA. (tfoschi@sfsu.edu)

M. E. Hervig, G & A Technical Software, Inc., P. O. Box 449, Driggs, ID 83422, USA. (m.e.hervig@gats-inc.com)

M. J. Legg and K. L. Pagan, NASA Ames Research Center, MS 245-5, Moffett Field, CA 94035-1000, USA. (legg@pixels.arc.nasa.gov; pagan@cloud1.arc.nasa.gov)

JOURNAL OF GEOPHYSICAL RESEARCH, VOL. 108, NO. D22, 4689, doi:10.1029/2003JD003741, 2003

Effect of adsorption on the uptake of organic trace gas by cloud droplets

Y. S. Djikaev
National Research Council Research Associateship Program, NASA Ames Research Center, Moffett Field, California, USA

A. Tabazadeh
Earth Science Division, NASA Ames Research Center, Moffett Field, California, USA

Received 1 May 2003; revised 27 June 2003; accepted 28 August 2003; published 18 November 2003.

[1] Adsorption can greatly influence the partitioning of organic trace species between the gas and liquid phases. Here we investigate how adsorption of organic species at the air-water interface in clouds can increase the amount of trace gas found in cloud water. For atmospherically relevant cloud surface areas and realistic ranges of adsorption parameters, we show that a significant amount of organic molecules can reside at the cloud droplet surface. Two different physical situations are considered corresponding to the cases where the surfactant is water-soluble and where it is water-insoluble. For both cases, numerical calculations were carried out for a wide range of adsorption parameters, effective Henry's law constants (the former case only), and cloud surface areas. For a soluble surfactant, our calculations show that the "overall" Henry's law constant, which takes into account for both adsorption at the droplet surface and partitioning into the droplet interior, can significantly differ from the standard Henry's law constant. For a moderately soluble species the overall uptake can strongly depend on the surface coverage if the species has a strong affinity for partitioning into the surface layer. Our results also suggest that even insoluble and/or scarcely soluble species can be scavenged by clouds if they are surface-active. *INDEX TERMS:* 0305 Atmospheric Composition and Structure: Aerosols and particles (0345, 4801); 0320 Atmospheric Composition and Structure: Cloud physics and chemistry; 0368 Atmospheric Composition and Structure: Troposphere—constituent transport and chemistry; *KEYWORDS:* uptake of organics, adsorption effect, cloud droplets

Citation: Djikaev, Y. S., and A. Tabazadeh, Effect of adsorption on the uptake of organic trace gas by cloud droplets, *J. Geophys. Res.*, *108*(D22), 4689, doi:10.1029/2003JD003741, 2003.

1. Introduction

[2] Clouds can significantly alter the chemical composition of the atmosphere through many processes, such as physical uptake, chemical reactions, precipitation, lightning, etc. [*Seinfeld and Pandis*, 1998; *Fleagle and Businger*, 1980; *Gill et al.*, 1983]. In this paper we will focus on the physical process of trace gas uptake in clouds.

[3] The process of physical adsorption has a number of important atmospheric implications. First, adsorbed species can participate in heterogeneous chemical reactions [*Bertram et al.*, 2001; *Ellison et al.*, 1999; *Abbatt and Waschewsky*, 1998], which can greatly influence the chemical composition of the atmosphere. Second, experimental studies of field collected samples indicate that the surface tension of cloud and/or aerosol particles can be lowered, relative to that of pure water [*Facchini et al.*, 1999a, 1999b, 2000; *Decesari et al.*, 2000], which is most likely due to the adsorption of organic molecules at the aqueous solution-air interface. The presence of organic molecules at the aqueous solution-air interface can influence both the activation process of aerosol particles into cloud droplets [*Nenes et al.*, 2002; *Anttila and Kerminen*, 2002; *Facchini et al.*, 2000], and the formation of ice in aqueous solutions [*Djikaev et al.*, 2002, 2003; *Tabazadeh et al.*, 2002a, 2002b].

[4] Usually, in atmospheric studies the physical uptake of a trace gas in cloud water is treated by using the Henry's law solubility constant, which linearly relates the trace gas pressure to its bulk concentration in liquid water. However, many observational data exist indicating that the standard Henry's law solubility constant sometimes underestimates the amount of trace gas measured in cloud water, particularly for organic species [*Glotfelty et al.*, 1987, 1990; *Capel et al.*, 1991; *Schomburg et al.*, 1991; *Sagebiel and Seiber*, 1993]. In this paper we suggest that surface adsorption may provide one possible explanation for the underestimation of solubilities predicted by the Henry's law. Specifically, the process of adsorption is not included in the definition of the Henry's law solubility constant. As we show below, for some cases, the number of trace gas molecules adsorbed on the cloud surface may exceed the number of molecules, which are dissolved in the bulk. For such scenarios, the

overall trace gas uptake in cloud water can deviate dramatically from that predicted by Henry's law because this formulation only relates the trace gas pressure to its concentration in the bulk and not on the surface.

2. Trace Gas Uptake Without Adsorption

[5] We will first outline the standard procedure for uptake calculations before presenting our model for quantifying the effect of adsorption on this process.

[6] Consider a closed system (a parcel of air) containing fixed numbers of water (component 1) and some trace gas (component 2) molecules, and denote these numbers by N_1 and N_2, respectively. Denote the volume and temperature of the system by V and T. To determine the trace gas uptake by water droplets in equilibrium with the vapor phase, it is necessary to solve the equations reflecting both the equilibrium conditions and mass conservation laws. According to the standard Henry's law, $c = HP_2$, where c is the molarity (moles of solute per liter of solution, units M ≡ mol/L), H is the Henry's law constant (M/atm), and P_2 is the pressure of the trace gas (atm). The Henry's law, coupled with the mass conservation law with respect to component 2 (trace gas), $N_2^{vap} + N_2^{sol} = N_2$ allows one to determine c and P_2.

[7] In the above procedure it is assumed that the adsorption of trace gas molecules at the liquid-vapor interface is negligible and that these molecules partition either into the liquid or into the vapor. Thus, trace gas molecules adsorbed at the air-water interface are not included in the mass conservation law. In the following section we will investigate how adsorption can increase the trace gas uptake in cloud water. In fact under some conditions adsorption can control the overall magnitude of the uptake process.

3. Effect of Adsorption

[8] The effect of adsorption on the overall uptake of a trace gas in cloud water is investigated for two physically different situations. First, the case where the gas molecule is water soluble and surface active (see Figure 1a). In such a system, the partitioning into the interface can occur from both the vapor and liquid phases. Such adsorption can be described by an adsorption isotherm whose parameters are determined by both mechanisms [*Donaldson*, 1999; *Adamson*, 1990]. Second, the case where the gas molecule is water insoluble but surface active (see Figure 1b). In such a system, no partitioning into the liquid phase can occur, but the molecule can adsorb at the droplet interface directly from the gas phase. This process is similar to the adsorption of gas molecule onto a solid substrate, but adsorption parameters can certainly be different for a case where the substrate is liquid [*Adamson*, 1990; *Donaldson*, 1999]. Thus, these two situations differ in that the mass conservation law should be augmented by different equations in order to take the effect of adsorption into account. It should be noted that in both cases the surfactant molecule is removed from the gas phase and is associated with, but not necessarily dissolved in the liquid phase.

[9] Clearly, in the real atmosphere many trace species can be simultaneously present. Some are water-soluble, while others are water-insoluble (see Figure 1c). Thus, the uptake of one species can, in principle, influence the uptake of others. At equilibrium, a multicomponent aqueous droplet may be covered by a thin film of insoluble organics. The transport of water-soluble molecules into and out of the aqueous solution can be impeded or enhanced by factors of

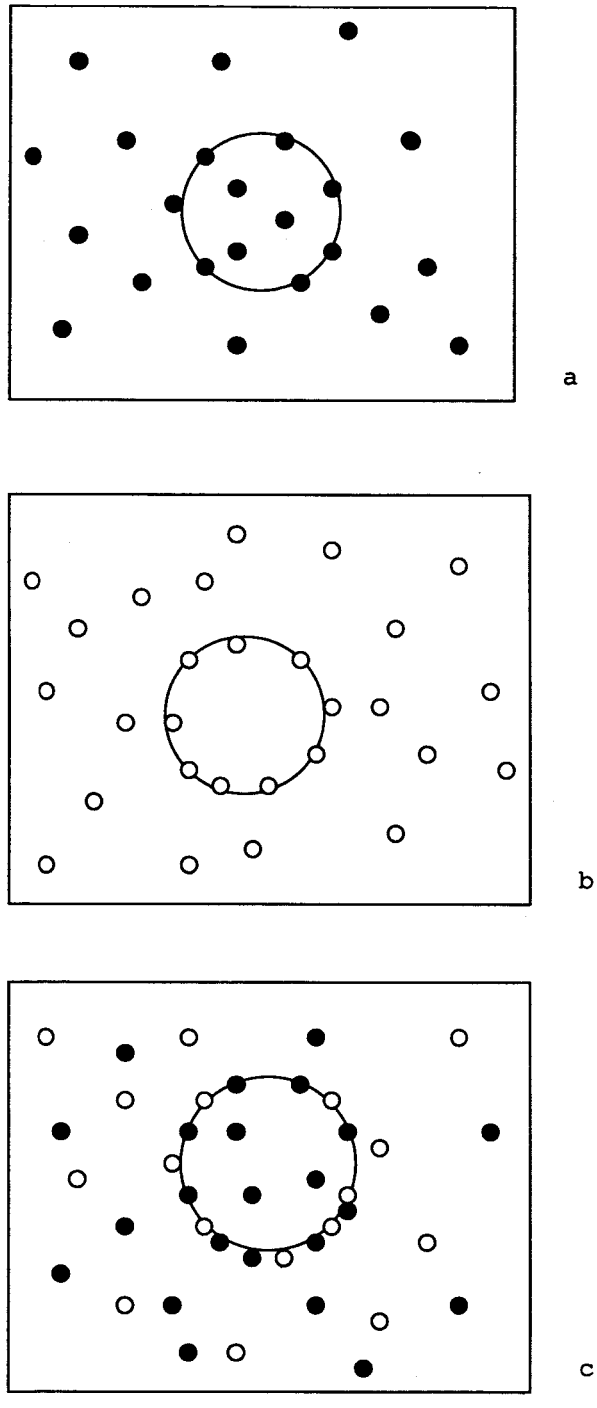

Figure 1. Trace gas uptake by a water droplet in different systems. (a) Uptake of water-soluble trace species (filled circles). (b) Uptake of water-insoluble trace species (open circles). (c) Uptake of simultaneously present water-soluble and water-insoluble species.

Table 1. Parameters H, H^{eff}, Γ_∞, and b for Some Atmospheric Trace Gases[a]

	H, M/atm	H^{eff}, M/atm	Γ_∞, cm^{-2}	b, M
Acetic acid	8.8×10^3	2.4×10^4 (5)	7.5×10^{13}	1.25
Formic acid	3.6×10^3	6.8×10^4 (5)		
1-Butanol	54–140		10.1×10^{13}	0.12
Methanol	140–230		9.2×10^{13}	2.48
Maleic acid	1×10^9			
Malonic acid	2×10^8			
Formaldehyde (methanal)	2.5	6.3×10^3		
Acetaldehyde (ethanal)	1.7–17			
Butyraldehyde (butanal)	5.5–9.6			
Heptanal	2.3–3.7			
Propionic acid	$(2.2–6.2) \times 10^3$		7.7×10^{13}	0.351
Acetone	3–35		6.7×10^{13}	0.423
Nitric acid	2.1×10^5	3.2×10^9 (3)	5×10^{14}	
Hydrogen Chloride	727	1.3×10^{12} (3)		
Ammonia	62	1.1×10^6 (3)	1.2×10^14	1.37

[a]The numbers in parentheses in column 3 indicate the pH of the solution.

several hundred or more when such films are present [*Gill et al.*, 1983; *Mmereki and Donaldson*, 2002]. This situation is not considered in the present work but will be the subject of future research.

3.1. Uptake of a Water-Soluble Trace Gas

[10] Let us consider a trace gas whose solubility in water is arbitrary but non-zero. At equilibrium, its molecules will be distributed between the vapor mixture, liquid solution, and interface. Thus we have to find three unknowns, N_2^{vap}, N_2^{sol}, and N_2^{srf}, which give the numbers of molecules of trace gas in the vapor, liquid, and at the interface. To do so *three* linearly independent equations are needed.

[11] First, there is a mass conservation law, relating all the variables:

$$N_2^{vap} + N_2^{srf} + N_2^{sol} = N_2. \tag{1}$$

Next, the Henry's law, providing a relation between N_2^{vap} and N_2^{sol}. If the solute (trace gas) molecule dissociates in solution, then c in the Henry's law should be treated as the overall molarity (including dissociated molecules) and H should be understood as the effective Henry's law constant [*Seinfeld and Pandis*, 1998]:

$$c = H^{eff} P_2. \tag{2}$$

Clearly, N_2^{sol} should be understood as the overall number of trace gas molecules within the solution. For a solute whose molecules do not dissociate, $H^{eff} = H$. Finally, N_2^{srf} can be expressed as a function of either N_2^{sol} or N_2^{vap} with the help of an adsorption isotherm. The adsorption of many organic species at the interface of their aqueous solutions is often well described by the Langmuir isotherm

$$\Gamma_2 = \Gamma_\infty \frac{c}{b + c}. \tag{3}$$

Here Γ_2 is the excess surface coverage of component 2. The parameter b is related to the rate constants for adsorption and desorption from the surface into the two bulk phases [*Donaldson*, 1999; *Donaldson and Anderson*, 1999], and Γ_∞ is the saturation value of Γ_2.

[12] The molarity c and pressure P_2 can be expressed as $c = (N_2^{sol}/N_A)/(V^{sol}/1000)$ and $P_2 = N_2^{vap} kT/(V^{vap} P_{atm})$, where N_A is the Avogadro number, k is Boltzmann's constant, and the division by $P_{atm} = 1013250$ dynes · cm^2/atm is necessary to obtain the pressure P_2 in units of "atm" (hereafter all other quantities are in CGS units). Thus, Henry's law (2) can be written in the form

$$N_2^{sol} = H^{eff} \frac{N_2^{vap} kT}{P_{atm}} \frac{V^{sol}}{V^{vap}} \frac{N_A}{1000}. \tag{4}$$

[13] Let us assume that the liquid water in the system is monodispersed over n^R droplets of radius R. Then, using the Langmuir adsorption isotherm (3), one can obtain

$$N_2^{srf} = S_n^R \Gamma_\infty \frac{(N_2^{sol}/N_A)/(V^{sol}/1000)}{b + (N_2^{sol}/N_A)/(V^{sol}/1000)}, \tag{5}$$

where $S_n^R = 4\pi R^2 n^R$ is the collective surface area of the ensemble of droplets (the appropriateness of one or another adsorption isotherm is discussed in subsection 3.3).

[14] Equations (1), (4), and (5) form a closed system of simultaneous equations in variables N_2^{vap}, N_2^{sol}, and N_2^{srf}. Its solution can be found analytically:

$$N_2^{vap} = \frac{Q_1 + \sqrt{4 \times 10^3 (P_{atm} V^{vap})^2 b N_2 Q_2 + Q_1^2}}{2Q_2} \tag{6}$$

$$Q_1 = H^{eff} kT P_{atm} V^{vap} \left(10^3 N_2 - 10^3 \Gamma_\infty S_n^R - b N_A V^{sol}\right) - 10^3 b (P_{atm} V^{vap})^2,$$

$$Q_2 = H^{eff} kT \left(H^{eff} kT N_A V^{sol} + 10^3 P_{atm} V^{vap}\right),$$

The quantities N_2^{sol} and N_2^{srf} are then obtained by substituting equation (6) into equation (4) and the result into equation (5).

3.2. Uptake of a Water-Insoluble Trace Gas

[15] Many organic species in the atmosphere are only scarcely soluble in water. Thus it is difficult to experimentally determine parameters b, Γ_∞, and H^{eff} for such species to use in equation (6). Moreover, many volatile organic

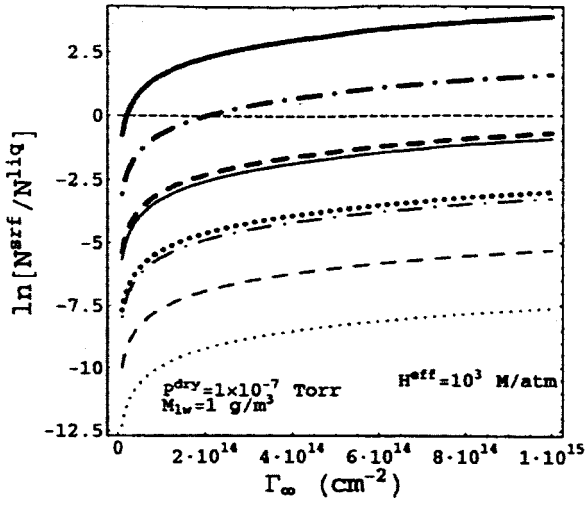

Figure 2. Ratio of the numbers of surface and volume located molecules as a function of Γ_∞. Different line styles correspond to different values of b: dotted curves represent b = 1 M, dashed b = 0.1 M, dot-dashed b = 0.01 M, and solid b = 0.001 M. The thicker (upper) curves are for R = 1 μm while the thinner (lower) ones are for R = 100 μm.

compounds present in the atmosphere are not water soluble, but may be strong surfactants due to the presence of both highly hydrophobic and hydrophilic structural elements. In fact, a variety of such organic compounds have been identified in atmospheric aerosols [*Gill et al.*, 1983; *Däumer et al.*, 1992; *Xiong et al.*, 1998]. These compounds have natural as well as anthropogenic sources and are mainly aliphatic hydrocarbons with C ≥ 10 and their derivatives such as acids, amines, alcohols, aldehydes, ketones, etc. The aliphatics may not have intrinsic surface-active character but can acquire it upon oxidation or amination [*Gill et al.*, 1983]. Among organic surfactants typically found in the atmosphere are alkanes (C_{15}–C_{33}), aromatic acids, fatty acids, polycyclic hydrocarbons, humic acids, proteins and protein breakdown products, etc (for a more detailed information on this issue we refer the reader to *Gill et al.* [1983]). The hydrophobic tail of a surface active molecule prevents it from partitioning into water, but such molecules can adsorb at the aqueous solution-air interface owing to their hydrophilic ends. Thus the partitioning between vapor phase and droplets can occur, although there would be no partitioning into the droplet interior. Therefore, the above adsorption model is not appropriate for this case.

[16] In order to take such adsorption into account, the fixed number of trace gas molecules, N_2, should be distributed between the vapor mixture and aqueous solution-air interface. Thus we need to find only two unknowns, namely, N_2^{vap} and N_2^{srf}, numbers of molecules of trace gas in the vapor and at the interface, respectively. To do so, the mass conservation law relating these variables,

$$N_2^{vap} + N_2^{srf} = N_2, \tag{7}$$

should be augmented by an appropriate adsorption isotherm which describes the adsorption of the trace gas from the vapor phase onto a liquid water surface. Such adsorption is often (but by no means always) well described by the Langmuir isotherm, that can be written in the form

$$\Gamma_2 = \Gamma_\infty \frac{KP_2}{1 + KP_2}, \tag{8}$$

where the parameter K is related to the rate constants for adsorption and desorption from the surface into the vapor phase only [*Adamson*, 1990]. Note that for the adsorption of insoluble species we cannot use the Langmuir adsorption isotherm as given in equation (3), because in this case the concentration of the adsorbate within the solution is zero. For the adsorption of soluble surfactants both equations (3) and (8) can be used, but it is more convenient to use the adsorption isotherm as given in equation (3) (for more detail, see, e.g., *Donaldson* [1999] and *Donaldson and Anderson* [1999]).

[17] For the sake of concreteness, let us choose the Langmuir adsorption isotherm to complete our model. Since $P_2 = kTN_2^{vap}/V^{vap}$, equation (8) can be rewritten in the form

$$N_2^{srf} = S_n^R \Gamma_\infty \frac{kTKN_2^{vap}/V^{vap}}{1 + kTKN_2^{vap}/V^{vap}}. \tag{9}$$

[18] Equations (7) and (9) form a closed system of simultaneous equations in variables N_2^{vap} and N_2^{srf}. Its solution can be found analytically:

$$N_2^{vap} = \frac{Q + \sqrt{4kTKN_2V^{vap} + Q^2}}{2kTK}$$
$$Q = kTK(N_2 - S_n^R\Gamma_\infty) - V^{vap}. \tag{10}$$

The quantity N_2^{srf} is obtained by substituting equation (10) into equation (9).

3.3. Generality and Limitations of the Model

[19] As mentioned above, equations (4)–(6) for the vapor-surface-liquid partitioning and equations (9) and (10) for the vapor-surface partitioning are derived for the case where the adsorption of a trace species follows the Langmuir adsorption isotherm. Clearly, if another adsorption isotherm is known to be more appropriate for a given system, equation (3) or equation (8) should be replaced by that isotherm. For example, in the case of a dissociating solute the Langmuir adsorption isotherm should be slightly modified [*Adamson*, 1990]. Furthermore, the Langmuir adsorption isotherm is inapplicable if the lateral interactions of adsorbate molecules are important, which may be the case, e.g., for "condensed" films [*Gill et al.*, 1983] of long chain hydrocarbons adsorbed on a droplet surface. In this situation the Frumkin adsorption isotherm [*Adamson*, 1990] is more adequate. On the other hand, many organic compounds that do not contain a "water-soluble" group have been observed [*Gill et al.*, 1983; *Bäumer and Findenegg*, 1982; *Hauxwell and Ottewill*, 1970] to form "gaseous" films upon adsorption from the vapor phase. In gaseous films the molecules are relatively far apart and are not steeply oriented (as they are in condensed films) but tend to lie flat on the surface [*Adam*, 1968]. The formation of such films has a multilayer character, and hence the Brunauer-

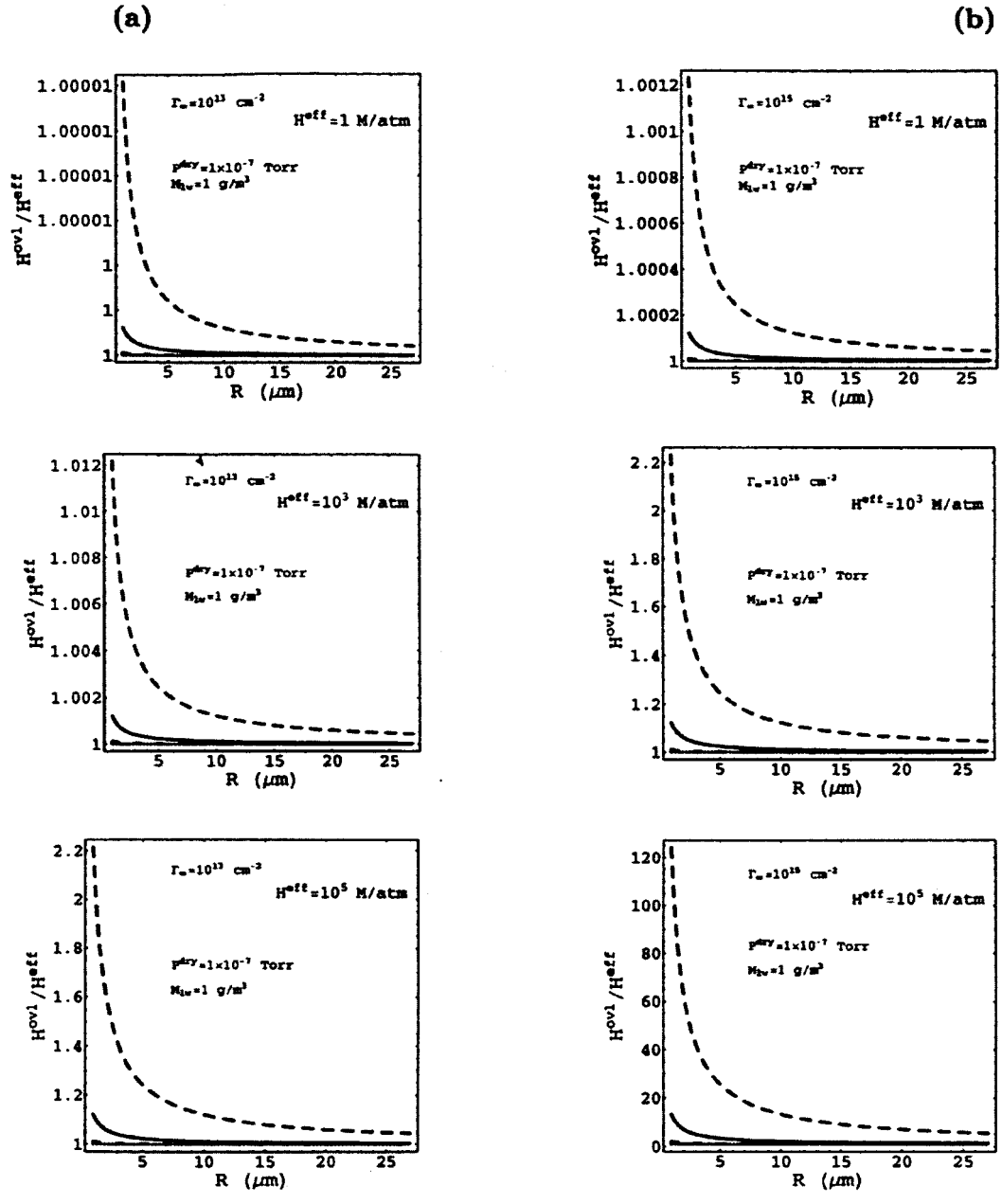

Figure 3. Fractional change in the overall Henry's law constant (volume + surface partitioning) as a function of droplet size. In column (a) $\Gamma_\infty = 10^{13}$ cm^{-2}, and in column (b) $\Gamma_\infty = 10^{15}$ cm^{-2}. The different line styles are for different b's, namely: the dotted curve is for b = 1 M, the dot-dashed curve for b = 0.1 M, the solid curve for b = 0.01 M, and the dashed for b = 0.001 M. The values of the effective Henry's law constant and other parameters are given in the panels themselves.

Emmett-Teller (BET) model of adsorption would be more appropriate [*Adamson*, 1990].

[20] Using any particular adsorption isotherm in the model leads to a set of expressions for N_2^{vap}, N_2^{sol}, and N_2^{srf} that are specific for that isotherm. Nevertheless, the general procedure of deriving these expressions, as outlined in preceding subsections, will remain unchanged.

[21] Although the above model is designed for a binary system "water + trace species", its generalization to multicomponent systems is straightforward. Such a generalization is important because in the real atmosphere many organic compounds are simultaneously present. Thus the adsorption of a given species at the droplet surface is influenced by surface contamination resulting from the adsorption of other species. Extending the model to multicomponent adsorption, for every additional trace species we would have to include another set of equations similar to equations (1)–(3) or (7)–(9). An analytical solution will

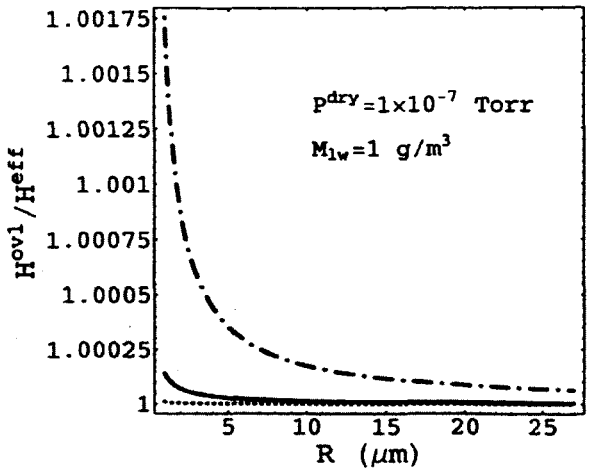

Figure 4. Overall Henry's law constant (volume + surface partitioning) for acetic acid (dot-dashed curve), butanol (solid curve) and methanol (dashed curve). The corresponding parameters are given in the figure panel and Table 1.

probably not always be so simple as for a binary case, due to the fact that the adsorption isotherm will contain the concentrations (in the droplet) or pressures of all trace species. However, numerical solutions of resulting algebraic equations are readily accessible by means of modern computers.

4. Numerical Evaluations

[22] To illustrate the sensitivity of predictions of our model to its different parameters, we carried out numerical evaluations for various H^{eff}, Γ_∞, b, K, and R. This would mimic model predictions in different dispersed systems for different volatile and semi-volatile organic species, whose solubility and surface activity in water would be reflected in varying these parameters. The temperature was taken T = 298.15 K. Table 1 compiles the values of these parameters for some species of atmospheric interest. The choice of parameter K in numerical calculations is discussed below.

[23] The pairs $H - H^{eff}$ in Table 1 were taken from *Seinfeld and Pandis* [1998] with indication of pH (between the parentheses) at which H^{eff} was evaluated (the effective Henry's law constant depends on pH of the solution). The unpaired values for H (the Henry's law constant which does not account for dissociation) were taken from R. Sander's web site (http://www.mpch-mainz.mpg.de/sander/res/henry.html). The data for Γ_∞ and b were provided by J. D. Donaldson from the University of Toronto (private communication, 2002), except for Γ_∞ for nitric acid which was taken from *Hudson et al.* [2002] (some inorganics are included in the table to show how H and H^{eff} can differ from each other). The solubility of a compound decreases with decreasing H^{eff}, while its surface activity increases with decreasing b and increasing Γ_∞.

[24] It should be noted that the parameters b and Γ_∞ in Table 1 are given for pure binary systems (water-trace gas). Clearly, in the atmosphere, there are many organic compounds that are simultaneously present in the air. Thus the adsorption of a given species at the droplet surface in the real atmosphere may not have the same parameters as shown in Table 1, because the droplet surface may be contaminated by other species. Therefore, the above presented models should be further developed to include the possibility of concurrent adsorption [*Adamson*, 1990], and further experimental work needs to be done to determine adsorption parameters for such systems [*Mmereki and Donaldson*, 2002].

[25] In our numerical calculations, the vapor and liquid volumes were taken $V^{vap} = 10^6$ cm^3 and $V^{sol} = 1$ cm^3, respectively. This gives about 1 g of liquid water per 1 m^3 of air, $M_{lw} = 1$ g/m^3, which is rather typical for most clouds although it may be smaller or even greater [*Baumgardner et al.*, 2003] (see below). Results for the adsorption of soluble surfactants are presented in Figures 2–4 while Figure 5 presents results for the adsorption of insoluble surfactants.

[26] Figure 2 shows the logarithm of the ratio N_2^{srf}/N_2^{sol} of surfactant molecules at the surface to that within the droplet interior as a function of parameter Γ_∞ in the range from 10^{13} to 10^{15} cm^{-2}. The horizontal dashed line shows where $N_2^{srf} = N_2^{sol}$ (for more detail see the figure panel and caption). The relative number of surface-located molecules (i.e., the ratio N_2^{srf}/N_2^{sol}) decreases by two orders of magnitude when the droplet radius increases from R = 1 μm to R = 100 μm for a fixed set of adsorption parameters. This occurs due to an increase in the surface-to-volume ratio of droplets with decreasing size. On the other hand, as expected, at a fixed R the ratio N_2^{srf}/N_2^{sol} increases with increasing Γ_∞ and decreasing b. Surprisingly, the N_2^{srf}/N_2^{sol} ratio is quite insensitive to the Henry's law constant, H^{eff}: the lines would remain nearly unchanged for H^{eff} ranging from 1 to 10^{10} M/atm (the calculations shown are for $H^{eff} = 10^3$ M/atm). Furthermore, the predictions of the model are not sensitive to P_2^{dry}, the trace gas pressure in the dry air parcel, at least under typical atmospheric conditions, where the trace gas pressure may vary in the range from 10^{-8} to 10^{-6} torr. According to *Singh et al.* [2001] the total pressure of organic trace species in the atmosphere hardly exceeds 2×10^{-6} torr, with methanol partial pressure being by far the largest of all oxygenated organics.

[27] In order to make a comparison between the predictions of our (modified) uptake model and those of the standard model (without adsorption), we calculated the ratio of the overall (including adsorption) and standard (bulk) effective Henry's law constants, H^{ovl}/H^{eff}. The quantity H^{ovl} was calculated by using the expression $H^{ovl} = P^{new}/c^{ovl}$, where P^{new} is the pressure predicted by our model and $c^{ovl} = 1000 * (N_2^{sol} + N_2^{srf})/(N_A V^{sol})$. Figure 3 shows the dependence of H^{ovl}/H^{eff} on the droplet radius R. The values of the effective Henry's law constant, adsorption parameters, and other details are given in the figure panels and caption. The extreme case $H^{eff} = 0$ and $b = 0$ would correspond to an insoluble surfactant. The specific curves (according to parameters given in Table 1) for acetic acid, butanol, and methanol are shown in Figure 4. As clear, the lines in all the panels converge to 1 with increasing R. Thus, for large droplets the overall partition coefficient, H^{ovl}, is quite insensitive to adsorption parameters and coincides with the standard value, H^{eff}. However, for small droplets the effective partition coefficient strongly depends on adsorption parameters and may significantly differ from

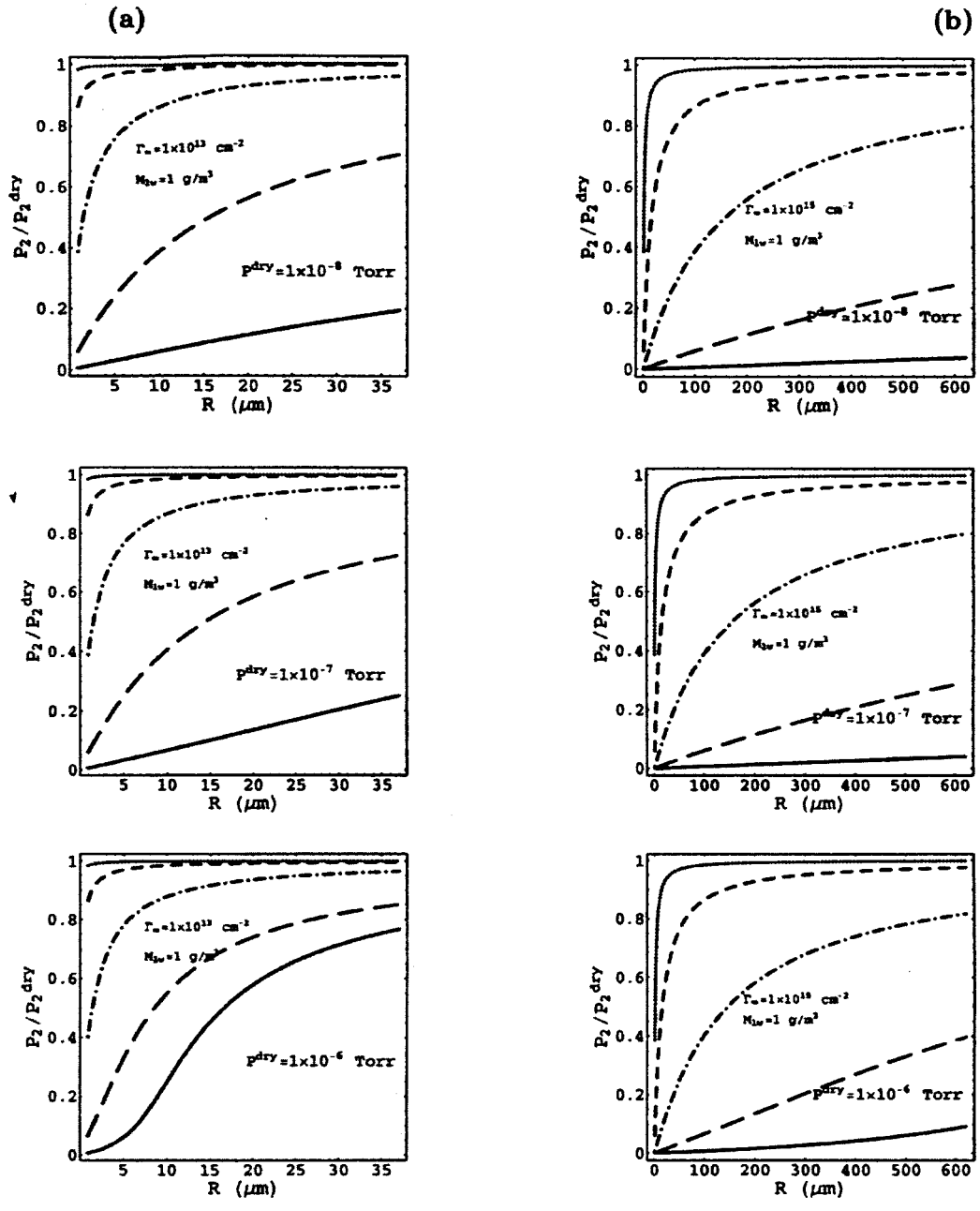

Figure 5. Reduction in the pressure of a trace gas of insoluble surfactant as a function of droplet size. In column (a) $\Gamma_\infty = 10^{13}$ cm^{-2}, and in column (b) $\Gamma_\infty = 10^{15}$ cm^{-2}. The different colors correspond to the different values of K, namely: $K = 1.7 \times 10^3$ Torr^{-1} for the dotted curve, $K = 1.7 \times 10^4$ Torr^{-1} for the short-dashed curve, $K = 1.7 \times 10^5$ Torr^{-1} for the dot-dashed curve, $K = 1.7 \times 10^6$ Torr^{-1} for the long-dashed curve, and $K = 1.7 \times 10^7$ Torr^{-1} for the solid curve.

H^{eff}. Besides, for a given set of adsorption parameters the overall Henry's law constant H^{ovl} strongly depends on the droplet size (this can be explained by the variation of the surface-to-volume ratio of a droplet with variation of its size). These two features could not have been captured within the framework of the standard uptake models, where surface effects are simply neglected.

[28] Finally, Figure 5 illustrates the adsorption behavior of an insoluble surfactant. The plots show P_2/P^{dry}, the ratio of the trace gas pressure in the dispersed system to its "dry" pressure (in the absence of water droplets) as a function of droplet radius R. The adsorption parameters and other details are given in the panels and caption of Figure 5. The K values considered ensure that the inequality $KP_{2e} \gg 1$ (with P_{2e} being the equilibrium vapor pressure of trace gas) holds for most volatile organic compounds of interest. This inequality should hold because if $P_2 = P_{2e}$, the trace gas would be in equilibrium with its pure liquid state. Therefore

a monolayer coverage should be expected to exist at the water surface under such a pressure, i.e., $\Gamma \simeq \Gamma_\infty$ at $P_2 \simeq P_{2e}$, which leads to the condition $KP_{2e} \gg 1$. As clear, even for large droplets the trace gas depletion is quite sensitive to the adsorption parameters K and Γ_∞. Also, for a given set of adsorption parameters, the trace gas depletion depends strongly on the droplet size (again, this is seemingly due to the variation of the surface-to-volume ratio of a droplet with R). Right panels (b) in Figure 3 show the whole range of possible droplet radii (the total liquid volume is 1 cm^3). Even one single water droplet of radius 620 μm can strongly deplete a trace gas of insoluble surfactant, having the adsorption parameters $\Gamma_\infty \approx 10^{15}$ cm^{-2} and $K \gtrsim 5 \times 10^3$ $torr^{-1}$. The existing models of trace gas uptake by clouds are intrinsically unable to capture any of these features because they neglect the process adsorption.

[29] In accordance with Figures 3 and 4, for droplets with $R \lesssim 1$ μm the effect of adsorption on the uptake of a soluble species can become significant for $b \lesssim 1$ M. The smaller H^{eff} is, the more stringent the surface activity requirement is (i.e., the smaller b is required). Furthermore, the adsorption effect can be important for $\Gamma_\infty \gtrsim 10^{12}$ cm^{-2} provided that the corresponding b is small enough. If the liquid water content is reduced to $M_{lw} = 0.1$ g/m^3 (results not shown in figures), the effect of adsorption becomes weaker, especially for ensembles of large droplets, but remains significant for $H^{eff} \gtrsim 10^3$ M/atm and $b \lesssim 0.1$ M. Figure 5 shows that for droplets with $R \lesssim 1$ μm the effect of adsorption on the uptake of an insoluble surfactant can become important when $K \gtrsim 10^4$ $Torr^{-1}$ and $K \gtrsim 10^3$ $Torr^{-1}$ for $\Gamma_\infty \simeq 10^{13}$ cm^{-2} and $\Gamma_\infty \simeq 10^{15}$ cm^{-2}, respectively. For these ranges of adsorption parameters, reducing the liquid water content to $M_{lw} = 0.1$ g/m^3 (results not shown in figure) has a negligible effect on the uptake.

[30] As mentioned above, in the real atmosphere many trace species are simultaneously present. Therefore, their uptake by cloud droplets occurs as a concurrent process conditioned by all compounds. For example, according to *Gill et al.* [1983], *Däumer et al.* [1992], and *Xiong et al.* [1998], the transport of molecules into and out of the aqueous solution is impeded by factors of several hundred or more when organic films are present. Recently, *Mmereki and Donaldson* [2002] have also reported an enhanced adsorption of pyrene at the hexanoic acid-coated water surface, even with sub-monolayer coverages of hexanoic acid. One can expect to observe a similar adsorption effect for many organic molecules present in the atmosphere.

5. Concluding Remarks

[31] We have presented a new model for the uptake of atmospheric trace gases by water droplets in clouds. In our model, the gas adsorption at the droplet-air interface is taken into account. We have investigated how the adsorption of organic molecules at the air-water interface in clouds can increase the amount of trace species found in cloud water. We have shown that for atmospherically relevant cloud surface areas and realistic ranges of adsorption parameters a significant fraction of organic molecules can reside at the surface of cloud droplets. Two different physical situations have been studied, corresponding to the cases where the trace gas is water-soluble and where it is water-insoluble. To analytically describe the adsorption phenomenon, the adsorption isotherm for a given system needs to be known. This can be written in terms of solution composition if the surfactant is water-soluble, or in terms of the pressure if the surfactant is water-insoluble. For the sake of illustration, we have carried out numerical calculations for a wide range of adsorption parameters, effective Henry's law constants (the former case only), and cloud surface areas using the Langmuir adsorption isotherm. For a soluble surfactant, our calculations show that the "overall" Henry's law constant, which takes into account for both adsorption at the droplet surface and partitioning into the droplet interior, can significantly differ from the experimental Henry's law constant. For an insoluble surfactant, our results suggest that an organic trace gas can be strongly depleted by clouds due to mere adsorption onto cloud droplet surfaces.

[32] Both adsorption models that we have presented above are applicable only to pure binary systems (water-trace gas). In the real atmosphere, many types of organic compounds are simultaneously present. Therefore the adsorption of one species at the droplet surface is likely to occur as concurrent adsorption at the surface contaminated by other surfactant(s). Contaminants can either enhance or impede the adsorption of other species. Thus, further work needs to be done to include the possibility of multicomponent adsorption, and more experimental work is needed to determine the corresponding adsorption parameters.

[33] **Acknowledgments.** The work was performed while Y.S.D. held an NRC Research Associateship Award at NASA Ames Research Center. NASA's Atmospheric Chemistry Modeling and Analysis Program also provided support for this project.

References

Abbatt, J. P. D., and G. C. G. Waschewsky, Heterogeneous interactions of HOBr, HNO_3, O_3, and NO_2 with deliquescent NaCl Aerosols at room temperature, *J. Phys. Chem. A*, *102*, 3719–3725, 1998.

Adam, N. K., *The Physics and Chemistry of Surfaces*, Dover, Mineola, N. Y., 1968.

Adamson, A. W., *Physical Chemistry of Surfaces*, John Wiley, Hoboken, N. J., 1990.

Anttila, T., and V. M. Kerminen, Influence of organic compounds on the cloud droplet activation: A model investigation considering the volatility, water solubility, and surface activity of organic matter, *J. Geophys. Res.*, *107*(D22), 4662, doi:10.1029/2001JD001482, 2002.

Bäumer, D., and G. H. Findenegg, Adsorption of hydrocarbon vapors on the surface of water, *J. Colloid Interface Sci.*, *85*, 118–127, 1982.

Baumgardner, R. E., S. S. Isil, T. F. Lavery, C. M. Rogers, and V. A. Mohnen, Estimates of cloud water deposition at mountain acid deposition program sites in the Appalachian Mountains, *J. Air Waste Manage. Assoc.*, *53*, 291–303, 2003.

Bertram, A., A. V. Ivanov, M. Hunter, L. T. Molina, and M. J. Molina, Reaction probability of OH on organic surfaces of tropospheric interest, *J. Phys. Chem. A*, *105*, 9415–9421, 2001.

Capel, P. D., C. Leuenberger, and W. Giger, Hydrophobic organic-chemicals in urban fog, *Atmos. Environ., Part A*, *25*, 1335–1346, 1991.

Däumer, B., R. Niessner, and D. Klockow, Laboratory studies of the influence of thin organic films on the neutralization reaction of H2SO4 aerosol with ammonia, *J. Aerosol Sci.*, *23*, 315–325, 1992.

Decesari, S., M. C. Facchini, S. Fuzzi, and E. Tagliavini, Characterization of water-soluble organic compounds in atmospheric aerosol: A new approach, *J. Geophys. Res.*, *105*(D1), 1481–1489, 2000.

Djikaev, Y. S., A. Tabazadeh, P. Hamill, and H. Reiss, Thermodynamic conditions for the surface stimulated crystallization of atmospheric droplets, *J. Phys. Chem. A*, *106*, 10,247–10,253, 2002.

Djikaev, Y. S., A. Tabazadeh, and H. Reiss, Thermodynamics of crystal nucleation in multicomponent droplets: Adsorption, dissociation, and surface-stimulated nucleation, *J. Chem. Phys.*, *118*, 6572–6581, 2003.

Donaldson, D. J., Adsorption of atmospheric gases at the air-water interface, I, NH_3, *J. Phys. Chem. A*, *103*, 62–70, 1999.

Donaldson, D. J., and D. Anderson, Adsorption of atmospheric gases at the air-water interface, II, C_1-C_4 alcohols, acids, and acetone, *J. Phys. Chem. A*, *103*, 871–876, 1999.

Ellison, G. B., A. F. Tuck, and V. J. Vaida, Atmospheric processing of organic aerosols, *J. Geophys. Res.*, *104*, 11,633–11,641, 1999.

Facchini, M. C., M. Mircea, S. Fuzzi, and R. J. Charlson, Cloud albedo enhancement by surface-active organic solutes in growing droplets, *Nature*, *401*, 257–259, 1999a.

Facchini, M. C., et al., Partitioning of the organic aerosol component between fog droplets and interstitial air, *J. Geophys. Res.*, *104*(D21), 26,821–26,832, 1999b.

Facchini, M. C., S. Decesari, M. Mircea, S. Fuzzi, and G. Loglio, Surface tension of atmospheric wet aerosols and cloud/fog droplets in relation to their organic carbon content and chemical composition, *Atmos. Environ.*, *34*, 4853–4857, 2000.

Fleagle, R., and J. Businger, *An Introduction to Atmospheric Physics*, Academic, San Diego, Calif., 1980.

Gill, P. S., T. E. Graedel, and C. J. Weschler, Organic films on atmospheric aerosol particles: Fog droplets, cloud droplets, raindrops, and snowflakes, *Rev. Geophys.*, *21*, 903–920, 1983.

Glotfelty, D. E., J. N. Seiber, and L. A. Liljedahl, Pesticides in fog, *Nature*, *325*, 602–605, 1987.

Glotfelty, D. E., M. S. Majewski, and J. N. Seiber, Distribution of several organophosphorus insecticides and their oxygen analogs in a foggy atmosphere, *Environ. Sci. Technol.*, *24*, 353–357, 1990.

Hauxwell, F., and R. H. Ottewill, A study of surface of water by hydrocarbon adsorption, *J. Colloid Interface Sci.*, *34*, 473–479, 1970.

Hudson, P. K., J. H. Shilling, M. A. Tolbert, and O. B. Toon, Uptake of nitric acid on ice at stratospheric temperatures: Implications for cirrus clouds, *J. Phys. Chem. A*, *106*, 9874–9882, 2002.

Mmereki, B. T., and D. J. Donaldson, Laser induced fluorescence of pyrene at an organic coated air-water interface, *Phys. Chem. Chem. Phys.*, *4*, 4186–4191, 2002.

Nenes, A., R. J. Charlson, M. C. Facchini, M. Kulmala, A. Laaksonen, and J. H. Seinfeld, Can chemical effects on cloud droplet number rival the first indirect effect?, *Geophys. Res. Lett.*, *29*(17), 1848, doi:10.1029/2002GL015295, 2002.

Sagebiel, J. C., and J. N. Seiber, Studies on the occurrence and distribution of wood smoke marker compounds in foggy atmospheres, *Environ. Toxicol. Chem.*, *12*, 813–822, 1993.

Schomburg, C. J., D. E. Glotfelty, and J. N. Seiber, Pesticide occurrence and distribution in fog collected near Monterey, California, *Environ. Sci. Technol.*, *25*, 155–160, 1991.

Seinfeld, J. H., and S. Pandis, *Atmospheric Chemistry and Physics*, John Wiley, Hoboken, N. J., 1998.

Singh, H., Y. Chen, A. Staudt, D. Jacob, D. Blake, B. Heikes, and J. Snow, Evidence from the Pacific troposphere for large global sources of oxygenated organic compounds, *Nature*, *410*, 1078–1081, 2001.

Tabazadeh, A., Y. S. Djikaev, and H. Reiss, Surface crystallization of supercooled water in clouds, *Proc. Natl. Acad. Sci.*, *99*, 15,873–15,878, 2002a.

Tabazadeh, A., Y. S. Djikaev, P. Hamill, and H. Reiss, Laboratory evidence for surface nucleation of solid polar stratospheric nitric acid, *J. Phys. Chem. A*, *106*, 10,238–10,246, 2002b.

Xiong, J. Q., M. H. Zhong, C. P. Fang, L. C. Chen, and M. Lippmann, Influence of organic films on the hygroscopicity of ultrafine sulfuric acid aerosol, *Environ. Sci. Technol.*, *32*, 3536–3541, 1998.

Y. S. Djikaev, NRC Associateship, NASA Ames Research Center, MS 245-4, Moffett Field, CA 94035, USA. (djikaev@venus.arc.nasa.gov)

A. Tabazadeh, Earth Science Division, NASA Ames Research Center, MS 245-4, Moffett Field, CA 94035, USA. (azadeh.tabazadeh-1@nasa.gov)

Dissolution, Speciation and Reaction of Acetaldehyde in Cold Sulfuric Acid

Rebecca R. Michelsen, Samantha F. M. Ashbourn, and Laura T. Iraci*
Atmospheric Chemistry and Dynamics Branch
NASA Ames Research Center, MS 245-5, Moffett Field, CA 94035

17 May 2004

Submitted to the Journal of Geophysical Research-Atmospheres.
**Author to whom correspondence should be addressed.*

Abstract

The uptake of gas-phase acetaldehyde [CH_3CHO, ethanal] by aqueous sulfuric acid solutions was studied under upper tropospheric/lower stratospheric (UT/LS) conditions. The solubility of acetaldehyde was found to be low, between 2×10^2 M atm^{-1} and 1.5×10^5 M atm^{-1} under the ranges of temperature (211-241 K) and acid composition (39-76 weight percent, wt%, H_2SO_4) studied. Under most conditions, acetaldehyde showed simple solubility behavior when exposed to sulfuric acid. Under moderately acidic conditions (usually 47 wt% H_2SO_4), evidence of reaction was observed. Enhancement of uptake at long times was occasionally detected in conjunction with reaction. The source of these behaviors and the effect of acetaldehyde speciation on solubility are discussed. Implications for the uptake of oxygenated organic compounds by tropospheric aerosols are considered.

Introduction

The importance of acid-catalyzed reactions of carbonyl compounds in and on aerosol particles has garnered a growing amount of attention in recent years. In particular, the accelerated increase of secondary organic aerosol mass due to acid-catalysis has been observed [*Jang and Kamens*, 2001]. These same authors observed that aldehydes are more reactive than ketones in these systems [*Jang et al.*, 2003]. In a different experiment, both aldol condensation and retro-aldol reactions were observed for 2,4-pentanedione in sulfuric acid solutions [*Nozière and Riemer*, 2003], and those authors hypothesize that one of the chemical precursors to these reactions, the enol form of the carbonyl, dictates whether reaction occurs. The importance of the speciation of organic

compounds in solution has been often mentioned, without detailed investigation. One exception is the study of formaldehyde uptake by aqueous sulfuric acid droplets, which considered the formation of hydrated (gem-diol) and protonated formaldehyde [*Jayne et al.*, 1996]. Unlike formaldehyde and acetone, acetaldehyde establishes equilibrium with all these species (enol, gem-diol, and protonated forms) in acidic, aqueous solution.

Field studies have revealed that the vast majority of sulfate particles in the UT/LS have some degree of organic matter, and those below the tropopause contain large amounts of oxygenated organic material [*Murphy et al.*, 1998; *Sheridan et al.*, 1994]. Simple solubility of known UT/LS organic compounds does not account for the abundance of material seen *in situ* [*Iraci et al.*, 2003], but acid-catalyzed organic reactions could provide an alternate pathway for the incorporation of organic material into particles. Laboratory studies have noted reactions of organic compounds taken up from the gas phase under UT/LS conditions, e.g., polymerization of formaldehyde [*Iraci and Tolbert*, 1997] and aldol condensation of acetone [*Duncan et al.*, 1998; *Kane et al.*, 1999]. The behavior of the acetone/sulfuric acid system is particularly interesting since the reaction has only been observed at high acid compositions ($\geq$ 75 wt%). Explanations for this behavior have been hypothesized and include 1) the decreasing concentration of acetone with acid composition reduces the second-order reaction rate [*Michelsen and Roberts*, 2004] and 2) the low enolization constant of acetone precludes reaction [*Nozière and Riemer*, 2003]. Since the acid composition of UT/LS particles is limited to 35-70 wt% H_2SO_4 [*Clegg et al.*, 1998; *Tabazadeh et al.*, 1997], self reaction of acetone is excluded from occurring in the atmosphere. Studying acetaldehyde's reactivity in low-

temperature acid solutions expands our body of atmospheric knowledge of how chemical functionality affects the reactivity of organic compounds in sulfate particles.

In this work, measurements of the solubility of acetaldehyde in low-temperature sulfuric acid are presented. We report evidence of reaction at conditions typical of the upper troposphere. Furthermore, the effects of the chemical speciation of acetaldehyde on its solubility and reactivity in acidic solutions are explored. We briefly discuss the possibility that solubility as observed in our experiments may exceed Henry's law equilibrium. Atmospheric implications of these results are considered.

Experimental

The uptake of acetaldehyde was measured using a classic Knudsen cell apparatus [*Golden et al.*, 1973] which consists of two Teflon-coated Pyrex chambers separated by a valve. The lower chamber was filled with several milliliters of an aqueous sulfuric acid solution of the desired concentration. The lower chamber, which has two thermocouples mounted on the outside of the cell wall to measure the temperature, was suspended in a recirculating cold bath. The temperature of the thermocouple closest to the surface of the acid was calibrated according to the experimentally-determined composition of the acid and the measured vapor pressure of water above the acid [*Zhang et al.*, 1993]. These corrections were usually <1 K. The uncertainty in the temperature measurements is estimated to be no larger than ±1 K. Gaseous water and acetaldehyde were admitted to the upper chamber of the cell through separate capillaries and exited via a calibrated aperture to a differentially pumped mass spectrometer (Balzers QMG 421C electron ionization quadrupole system). The total pressure in the cell was usually ≤ 25 mtorr to

insure that the free mean path of the gas molecules was longer than or comparable to the diameter of the escape aperture. Water vapor was introduced and matched to the vapor pressure of the acid to prevent changes in its composition.

Once a stable flow of acetaldehyde was established in the upper chamber, exposure to the sulfuric acid surface was initiated by opening the valve to the lower chamber. The uptake of acetaldehyde was monitored as m/z = 29 (CHO^+); this fragment was used since the molecular peak (m/z = 44, CH_3CHO^+) coincides with carbon dioxide. Raw data from a typical experiment is shown in Figure 1; the acid was 47 wt% H_2SO_4 and the temperature was 226 K. When exposure begins at t = 0 s, the gas-phase acetaldehyde signal quickly decreases as the gas is taken up by the acid. The signal more slowly returns to its initial intensity as the acid becomes concentrated in acetaldehyde. The time dependence of the signal depends on the solubility and liquid-phase diffusion of acetaldehyde in sulfuric acid (*vide infra*). Exposure was ended at ~260 s by closing the valve to the lower chamber.

The net uptake coefficient (γ), which is defined as the fraction of incident molecules taken up by the surface, can be calculated from the raw data:

$$\gamma = \frac{A_h}{A_s}\left(\frac{F_o - F}{F}\right) \qquad (1)$$

The number of molecules lost to the surface is measured by the change in flow to the mass spectrometer upon exposure, $F_o - F$, where F_o is the flow prior to exposure and F is the time-dependent flow during exposure. Because the mass spectrometer signal is proportional to the flow of molecules out of the cell, the signal can be used directly in the

calculation. A_h is the area of the escape aperture (0.018 or 0.049 cm^2), and A_s is the surface area of the sulfuric acid in the cell (5.7 cm^2). The rate of acetaldehyde diffusion into the bulk liquid, combined with the overall solubility and any reaction which occurs, controls the time dependence of γ according to [*Finlayson-Pitts and Pitts*, 2000]:

$$\frac{1}{\gamma} = \frac{1}{\Gamma_g} + \frac{1}{\alpha} + \frac{\sqrt{\pi}\bar{c}}{4RTH^*\sqrt{D}}\left(\frac{1}{t^{-1/2} + \sqrt{\pi k}}\right) \qquad (2)$$

where t is time, $\bar{c}$ is the average molecular velocity, R is the universal gas constant, T is the absolute temperature, D is the liquid-phase diffusion coefficient, α is the mass accommodation coefficient, k is the pseudo-first-order rate constant, and Γ_g characterizes any limit due to gas-phase diffusion. In equation 2, the *effective* Henry's law solubility coefficient, H^*, is used, since there are a number of equilibrium processes (hydration, enolization, and protonation) expected to contribute to acetaldehyde uptake in addition to molecular solubility [*Solomons*, 1992]. If there is no reaction ($k = 0$), then plotting $1/\gamma$ versus $\sqrt{t}$ yields a straight line; $H^*\sqrt{D}$ can be calculated from the slope and the effective Henry's law coefficient can be determined if the diffusion coefficient is known. Diffusion coefficients were calculated according to $D=cT/\eta$, where the constant c was calculated to be 5.5×10^{-8} mol cm K^{-1} s^{-2} from the Le Bas molecular volume [*Reid et al.*, 1987] and the viscosity of the acid, η, was calculated from the parameterization of Williams [*Klassen et al.*, 1999; *Williams and Long*, 1995].

Sulfuric acid solutions were prepared from 96 wt% stock solution (Merck) and deionized water (Aldrich HPLC-grade). The solution concentrations were measured as 76.2 ± 0.4, 66.3 ± 0.3, 47.3 ± 0.3, 48.7 ± 0.2 and 38.5 ± 0.2 wt% H_2SO_4 by titration with

sodium hydroxide standard. A magnetic stir bar in the acid solution allowed the sample to be mixed between experiments (≥ 15 min). Gas-phase acetaldehyde (Acros 99.5%) and water were taken from the vapor above liquid samples which were purified with at least one freeze-pump-thaw cycle each day. Due to the volatility of acetaldehyde, it was kept in a dry ice/ethanol bath during use. The partial pressure of acetaldehyde used in the experiments ranged from 0.2 to 2.0 mtorr. For several experiments, discussed in the Reaction section, crotonaldehyde [C_4H_6O, 2-butenal] (Aldrich 99+%) was mixed with 49 wt% acid; the solutions were immediately quenched in a dry ice/ethanol bath to prevent evaporation and reaction. It was assumed that the amounts of crotonaldehyde added were small enough that there was no appreciable change in the sulfuric acid concentration. (Microliters of crotonaldehyde were diluted to 50 mL of solution for final concentrations of 10^{-4} to 10^{-3} M.)

Results and Discussion

Solubility Measurements. Uptake experiments were performed in the Knudsen cell over ranges of acid composition (39-76 wt% H_2SO_4) and temperature (211-241 K). The raw data for each experiment were analyzed by the method outlined above; the uptake coefficient was calculated from the acetaldehyde signal (e.g., Figure 1), and its inverse was plotted versus square root of time (see Figure 2). Two distinct behaviors were observed. In the majority of the experiments, the data showed simple solubility, that is, a straight line, as shown in Figure 2a. However, a significant fraction (about one third) of the experiments showed different behavior: the $1/\gamma$ data curved, as shown in Figure 2b. This behavior was observed in two experiments apiece for the 39 wt% and 66 wt% acids,

and for all but the coldest 47 wt% acid (indicated by "rxn" Table I). The curvature is an indication of reaction, and is discussed below. For those experiments which exhibited linear $1/\gamma$ data, the Henry's law coefficient was determined from the slope according to equation 2 with $k = 0$. For example, under the conditions of 66 wt% H_2SO_4 at 221 K in Figure 2a, H^* was calculated to be 6.7×10^3 M atm^{-1}. The data at $\sqrt{t} < 3.5\ \sqrt{s}$ were not included because equation 2 does not reproduce at early times the coupled differential equations which describe the uptake processes. For $1/\gamma$ data that deviated from linearity (Figure 2b), the Henry's law coefficient was also calculated. Clearly, the curved section of the data could not be used in this case, but inverse uptake during earlier times ($3.5\ \sqrt{s} < \sqrt{t} < 7$ to $12\ \sqrt{s}$, depending on when curvature became apparent) appeared to be linear. In Figure 2b, the data points used for the linear fit are indicated by closed circles. In this case, the acid composition was 47 wt%, and the temperature was 236 K; H^* was calculated to be 2.9×10^2 M atm^{-1}. We are confident that this method results in reasonable measurements of solubility for data exhibiting curvature since the resulting values are not significantly different from those calculated with linear data sets. In particular, in the 39 and 66 wt% acids, there were pairs of experiments under nearly identical conditions (the same acid composition and less than 0.3 K temperature difference) where one data set was curved and one was linear over the time of the experiment. In both of these cases, the measured H^* values differed by less than 16%, which is significantly less than the scatter (65%) in all the H^* values derived from strictly linear data (see Figure 3). We have not identified why the data were curved in only one of a pair of experiments under nearly identical conditions; deviation from linearity does not depend on acetaldehyde pressure or other experimental variables.

A summary of the measurements of the solubility of acetaldehyde in low-temperature sulfuric acid is given in Table I, along with experimental conditions and the calculated D values. The main sources of uncertainty in H^* are the uncertainty in the diffusion coefficient, commonly ~10% but up to 30% for the most viscous solutions, and the error in determining the slope of the $1/\gamma$ data. The error inherent in data analysis was also ~20%, but could be as high as 60% for curved data, since there were fewer data points included in these regressions. Thus the overall uncertainty in H* is usually ~25% and ~60% for data exhibiting reaction.

The Henry's law coefficients are also shown in a van't Hoff plot in Figure 3. For the conditions studied (39 to 76 wt% H_2SO_4, 210-240 K), the solubility of acetaldehyde varies from ~10^2 to 10^5 M atm^{-1}. These values demonstrate the low solubility of acetaldehyde in aqueous sulfuric acid solutions compared to other small organics studied under similar conditions. For example, acetone is approximately two orders of magnitude more soluble, [*Klassen et al.*, 1999] and methanol is about three orders of magnitude more soluble [*Iraci et al.*, 2002] than acetaldehyde. There are two interesting features of acetaldehyde solubility in sulfuric acid evident in Figure 3. First, acetaldehyde's solubility in 39 wt% H_2SO_4 is experimentally indistinguishable from its solubility in 47 wt% H_2SO_4. Otherwise, the solubility increases with solvent acidity as is typical for small, oxygenated organics. Secondly, with the exception of the most concentrated acid, acetaldehyde is considerably *less soluble* in mildly acidic solutions than in pure water (extrapolated from measurements made between 0 and 25°C [*Benkelberg et al.*, 1995]). This result is in direct contrast to other compounds, e.g., acetone [*Duncan et al.*, 1999; *Imamura and Akiyoshi*, 2000; *Kane et al.*, 1999; *Klassen et*

al., 1999] and methanol [*Iraci et al.*, 2002; *Kane and Leu*, 2001], which exhibit increased solubility in cold acid solutions relative to water, even at <50 wt% H_2SO_4. However, decreased solubility in mildly acidic solutions versus water has been observed for some organic compounds (e.g., cyclohexane, isobutane, 2,5-pentanedione) at room temperature. The minimum solubility is typically 35 to 45% of the value for dissolution in water, at around 40-45 wt% H_2SO_4 [*Nozière and Riemer*, 2003; *Rudakov and Lutsyk*, 1979; *Rudakov et al.*, 1987]. Our measurements indicate a minimum solubility in 47 wt% acid which is 15% of the value for solubility in water. We believe the speciation of acetaldehyde in solution contributes to this effect, as discussed in the next section.

The measurements of acetaldehyde dissolution in cold, aqueous H_2SO_4 also provide thermodynamic information about this process. From the slope of the lines in Figure 3, the enthalpy of solvation ($\Delta H°$) can be determined [*Klassen et al.*, 1999].

$$\log H^* = A + 1000B/T \tag{3}$$

$$A = \Delta S^\circ / 2.303R + \log M_{solv} \tag{4}$$

$$B = -\Delta H^\circ / 2.303R \tag{5}$$

where A and B are the intercept and slope, respectively, $\Delta S°$ is the entropy of solvation, and M_{solv} is the molarity of water in the solutions, calculated for 220 K [*Myhre et al.*, 2003]. The thermodynamic parameters are reported in Table II. Since large changes in dissolution entropy relative to water are not expected, we have fixed the value of $\Delta S°$ equal to that for acetaldehyde dissolution in water, -171 J mol^{-1} K^{-1} [*Benkelberg et al.*, 1995]. For the 76, 66, and 47 wt% acids, the difference this fixed entropy value makes in the calculation of the enthalpy of dissolution is minimal, ≤ 9%. However, in the 39 wt%

acid, a larger deviation from the best fit, 40%, is observed. In Figure 3, both the fixed-entropy best fit (solid grey line) and the best fit allowing $\Delta S°$ to vary (dashed grey line) are shown. This behavior—an apparently more negative entropy of dissolution for the most dilute acid studied—was also seen for methanol [*Iraci et al.*, 2002]. It is not clear whether this observation is significant or merely an artifact of the restricted accessible temperature range for the more dilute solutions. The measured enthalpies of solution for the 76, 66, 47, and 39 wt% acids are, respectively, -51.4, -47.6, -44.1, and -44.2 kJ mol^{-1}. Enthalpies of solution calculated by allowing $\Delta S°$ to vary are also given in Table II. If the entropy (i.e., the intercept) is allowed to vary in the fitting of the data for the 39 wt% acid, then the enthalpy is -62.0 kJ mol^{-1}. We have no physical explanation for why the enthalpy of dissolution for acetaldehyde should be significantly more negative in 39 wt% H_2SO_4 than in both water ($\Delta H°$ = -47.4 kJ mol^{-1}) [*Benkelberg et al.*, 1995] and the most acidic solution.

In order to determine the solubility of acetaldehyde (eq. 3) at conditions other than those studied herein, A can be calculated from equation 4 with $\Delta S°$ = -171 J mol^{-1} K^{-1} and B can be calculated from the following empirical relation:

$$B = -20.98(x_{H_2SO_4})^3 + 18.32(x_{H_2SO_4})^2 - 3.344(x_{H_2SO_4}) + 2.477 \qquad (6)$$

where $x_{H_2SO_4}$ is the mole fraction of sulfuric acid in the solution. The equation fits the data well, including acetaldehyde solubility in water [*Benkelberg et al.*, 1995]. This parameterization of acetaldehyde solubility is plotted versus acid composition in Figure 4; the experimentally measured solubilities (at 220 K) are shown as black

diamonds. It should not be extrapolated to more concentrated acid solutions (> 80 wt%), since there is no reason this third-order equation should apply outside the range of available data.

Effect of Speciation on Solubility. The overall solubility measurements reported herein are not simply due to physical dissolution, but also several fast equilibria common to oxygenated organic compounds. In order to explore how these different chemical processes affect uptake, we have thermodynamically modeled four concurrent dissolution pathways for acetaldehyde in aqueous sulfuric acid solutions. These processes and the literature values used in the model are summarized in Table III. They are simple physical dissolution, hydration (addition of a water molecule to the carbonyl group), protonation (addition of a proton to the carbonyl oxygen), and enolization (effectively a transfer of an alpha proton to the carbonyl oxygen). The solubility of each form of acetaldehyde is defined as its solution-phase concentration divided by the pressure of gas-phase acetaldehyde over the solution: molecular (H_{mol}), hydrated (or gem-diol) (H_h), protonated (H_a), and enolized (H_e) acetaldehyde. The total, or effective, solubility is therefore a sum of the solubility of the four species: $H^* = H_{mol} + H_h + H_a + H_e$. Only H^* is experimentally accessible with our technique.

Since the ionic strength of aqueous sulfuric acid is high, the physical dissolution of volatile solutes in aqueous sulfuric acid solutions has been treated with a "salting-out" effect, using the Setchenow equation [*Huthwelker et al.*, 1995; *Jayne et al.*, 1996; *Sander et al.*, 2003]. The form of Setchenow's approach (a negative exponential) dictates that solubility decreases as ionic strength increases. However, it is more appropriate to treat

sulfuric acid as a distinct solvent as opposed to a salt, at least when the solute is an organic compound [*Sanders*, 1985]. Data on the solubility of alkanes in aqueous H_2SO_4 favors this view: their solubility has been observed to decrease, pass through a minimum around 30-40 wt% H_2SO_4, and then increase again as acid content varies from 0 to 100 wt% [*Rudakov and Lutsyk*, 1979; *Rudakov et al.*, 1987]. Oxygenated organics (4-methyl-2-pentanone and 2,4-pentanedione) also show this trend [*Munro*, 1968; *Nozière and Riemer*, 2003], but those data are not readily available to adapt to our model and likely reflect solution-phase equilibria in addition to molecular solubility. We therefore base the *molecular* solubility of acetaldehyde on the solubility data of a non-oxygenated compound: cyclohexane in H_2SO_4 [*Rudakov and Lutsyk*, 1979]. The shape of these data (which varied little from other organic compounds) was incorporated into H_{mol} as a piece-wise linear function starting at the solubility of acetaldehyde in water. The form of this function is given in the footnote to Table III.

Where available, equilibrium constants and enthalpies from the literature for the other three equilibrium processes were used. The activity of water in and the density of aqueous H_2SO_4 solutions at low temperature were taken from the most recent parameterizations of these variables [*Knopf et al.*, 2003; *Myhre et al.*, 2003]. Equilibrium constants were adjusted to 220 K using available enthalpy values. The protonation of acetaldehyde was treated with the excess acidity method [*Cox*, 2000]. This approach to strongly acidic solutions depends upon two variables: the excess acidity, X, and the slope factor, m^*. X is defined as the ratio of activity coefficients for a theoretical reference base B*, $\log\left(\gamma_{B^*}\gamma_{H^+}/\gamma_{B^*H^+}\right)$, and is a measure of how much more acidic the solution is than the stoichiometric acidity. The slope factor is constant for a class of compounds

(e.g., aliphatic ketones) and quantifies the hydrogen bonding of the solvent to the protonated base [*Bagno et al.*, 1991]. Notably, neither the excess acidity slope factor, m^*, nor the enthalpy of protonation have been measured for small aldehydes, so the values for acetone were used [*Bagno et al.*, 1991]. Furthermore, the only available measurement of the acidity of protonated acetaldehyde used the Hammett acidity scale [*Levy et al.*, 1970]. Following the lead of Baigrie [1985], the pK_a measured on the Hammett scale was multiplied by m^* to give an approximation of the pK_a on the excess acidity scale.

The model is neither exhaustive (it does not include the protonation of hydrated acetaldehyde, for example) nor definitive (due to lack of experimental measurements and conflicting values in the literature). Nevertheless, it is a reasonable expression of the interaction among the primary equilibria at play in the system. Solubility versus acid composition at 220 K as defined by the speciation model is plotted in Figure 4. The total acetaldehyde solubility (H^*) is shown as a thin black line, while the individual species' contributions are shown as grey dashed and/or dotted lines as indicated. While the overall solubility does not precisely match the parameterization of our experimental values, it is correct both in order of magnitude and that it passes through a minimum. The difference between experimental values and the model may be due to one or more factors; protonation or molecular dissolution might be underestimated by the model, hydration could be overestimated at the low temperature due to significant temperature dependence of the enthalpy value, or perhaps there is an unidentified process at high acidities not included in our model. It should be noted, though, that the most uncertain value in the model is the pK_a of protonated acetaldehyde. The only available

measurement must be converted to the excess acidity scale with m^*, which is not available for aldehydes. Measured values of m^* for acetone vary widely, giving an enormous range of -8.7 to -3.6 for the pK_a of protonated acetaldehyde. In fact, if we instead arbitrarily set the pK_a to -1.7, then the total acetaldehyde solubility of the model overlays our data beautifully. However, we believe the most reasonable value is -3.6 (the most recent measurement of m^* for acetone [*Bagno et al.*, 1991] multiplied by the experimental measurement on the Hammett acidity scale [*Levy et al.*, 1970]), since this value means acetaldehyde is somewhat more basic than acetone (pK_a=-3.06 [*Bagno et al.*, 1991]).

Uncertainties aside, the behavior of the individual dissolution pathways as predicted by the model is instructive. When the water content of the solvent is high (<60 wt% H_2SO_4), the gem-diol is readily formed and significantly enhances acetaldehyde solubility (e.g., by a factor of 11 at 40 wt% H_2SO_4). As the water activity decreases with increasing acid content, formation of the gem-diol becomes less important. Conversely, as the acid content increases, the protonated form dominates (>75 wt% H_2SO_4). At 80 wt% H_2SO_4, acetaldehyde solubility is increased due to protonation by a factor of four. In between these extremes, molecular acetaldehyde is the dominant form. Enolized acetaldehyde is always a minute fraction of total dissolved acetaldehyde, since its equilibrium constant is so small ($\sim 10^{-6}$). Therefore, we interpret the variation of solubility exhibited by acetaldehyde as acid content changes as due to the competing dissolution channels available via speciation. In particular, the solubility of acetaldehyde is lower in dilute acid than in pure water because the availability of water to form the gem-diol decreases as water is displaced by acid. At higher acid composition

(>70 wt%), the protonation channel becomes important enough to enhance solubility. The enol form, though it may be an important precursor to reaction, has no appreciable effect on overall solubility.

Reaction. The curvature observed in a third of the $1/\gamma$ versus $\sqrt{t}$ plots (12 out of 38) is indicative of an additional loss channel beyond simple dissolution. Acetaldehyde is known to undergo aldol condensation-dehydration in sulfuric acid [*Baigrie et al.*, 1985] to form crotonaldehyde,

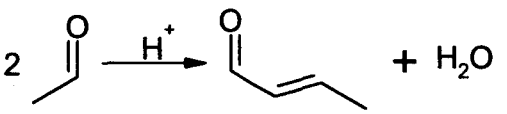

(7)

and we therefore believe this process to be responsible for the observed loss. The reaction was only observed under very specific conditions in our system: all experiments in 47 wt% acid, with the exception of one at the coldest temperature (216 K). Deviation from linearity was also seen infrequently for the 39 wt% and 66 wt% acids: at 216 and 222 K, and 223 and 231 K, respectively. (See Table I.) We were not able to quantify loss rates (pseudo-first order conditions do not apply), however, the deviation from linearity is more pronounced at warmer temperatures.

The aldol condensation-dehydration product of acetaldehyde is crotonaldehyde, so the mass fragments of this compound were monitored during experiments. Neither crotonaldehyde nor any other product was detected in the gas phase. Ternary solutions of sulfuric acid, water, and crotonaldehyde were mixed (49 wt% H_2SO_4; 1.4×10^{-3} M and 1.4×10^{-4} M crotonaldehyde) and placed in the Knudsen cell. Crotonaldehyde was

detected as m/z = 70. From the signal-to-noise ratios at different temperatures, we estimate that our detection limit (a signal-to-noise ratio of 2:1) for crotonaldehyde ranges from ~5×10^{-5} M at 238 K to ~2×10^{-4} M at 224 K in 49 wt% acid. According to the average length of our experiments (5 min), and the room temperature rate constant for crotonaldehyde production (2×10^{-5} M^{-1} s^{-1}; 298 K, 48 wt% H_2SO_4 [*Baigrie et al.*, 1985]), the concentration would be ~3×10^{-9} M at the end of the experiment. Clearly, any product formed is far below our detection limit. Infrared spectroscopy is currently being employed in detection of reaction products in the condensed phase.

The observation of reaction exclusively in the middle range of acidities is curious, since at room temperature the reaction proceeds in solutions with 9 to 90 wt% acid. In fact, the data of Baigrie [1985] show that the observed rate of the aldol condensation increases by four orders of magnitude with increasing acidity. Conversely, our observations suggest that the rate for aldol condensation is fastest at 47 wt% H_2SO_4, and slower at both higher and lower acidities. Could the dependence of the reaction rate on acidity change so much between 298 and 240 K? According to Baigrie [1985], the mechanism for aldol condensation of acetaldehyde involves three species: enolized acetaldehyde, protonated acetaldehyde, and a water molecule of the solvation shell. According to our thermodynamic model (discussed in the previous section), the solubility of enolized acetaldehyde (H_e) decreases slightly from 298 to 220 K, and so does the activity of water. (Note that the activity of water at 298 K is from Cox [2000], while the values at 220 K are from Knopf [2003].) The solubility of protonated acetaldehyde (H_a), however, is higher by almost three orders of magnitude at the lower temperature. This change in H_a seems not to be driven by changes in the pK_a (which exhibits only slight

variation with temperature), but mostly by changes in the excess acidity, *X*. Presumably, then, the colder solution is more acidic than the same stoichiometric concentration of H_2SO_4 at 298 K. Taking the temperature changes of the three species involved in the transition state into account, we predict that the projected rate of aldol condensation at 220 K will have a local maximum at around 60-65 wt% H_2SO_4. Thus the rate of acetaldehyde aldol condensation may be fastest in the middle acidity range at cold temperatures, in contrast to room temperature measurements.

Most of our data sets exhibiting reaction approach a steady-state loss, that is, the data tend toward the limit of a straight line with a slope ≥ 0. However, a small subset of these data sets (3 out of 12) shows somewhat different behavior: the $1/\gamma$ versus $\sqrt{t}$ data taper downward at long times. That is, the net uptake is mildly *increasing* with time. We have attempted to fit these data to equation 2 and conclude that such behavior cannot be explained by the combination of second-order reaction and constant solubility. Instead, we propose that this increasing uptake is due to a deviation from Henry's law solubility, which has been observed in other organic solute-aqueous solvent systems. For example, benzene shows increased solubility in water due to pairing at very low concentrations, $\sim 10^{-4}$ mole fraction ($\sim 6 \times 10^{-3}$ M) [*Tucker and Christian*, 1979]. In fact, for several organic compounds in aqueous solutions, Henry's law does not apply even as low as $\sim 10^{-5}$ mole fraction [*Westh et al.*, 1998]. We estimate that the near-surface concentration of acetaldehyde in our experiments generally reaches 10^{-4} to 10^{-3} M. A deviation from Henry's law implies that even at such low acetaldehyde concentrations, the solution is not ideally-dilute, and therefore the acetaldehyde molecules affect each other in solution.

Presumably, organic compounds of different types in mixed solutions would affect each other too. Clearly, further investigation into this possible effect is warranted.

Conclusions and Implications

The solubility of acetaldehyde was measured in aqueous sulfuric acid solutions representative of particles in the upper troposphere and lower stratosphere. It was found to be low: between 2×10^2 M atm^{-1} and 1.5×10^5 M atm^{-1} for the ranges of temperature (211-241 K) and acid composition (39-76 wt% H_2SO_4) studied. Reaction of an organic compound in moderately acidic sulfate solutions (38-67 wt% H_2SO_4) under atmospheric conditions was reported for the first time.

The importance of this particular reaction in the atmosphere is negligible. If we consider a characteristic sulfate particle which is ~50 wt% H_2SO_4, (at ~5 km, 267 K and 30% relative humidity, if unneutralized), and a typical remote concentration of acetaldehyde of 100 ppt [*Singh et al.*, 2001], we find that on average, a 0.1-μm particle will contain no acetaldehyde. Even if we assume that a more urban concentration of 10 ppb applies, there will be on average less than one molecule per particle. Ignoring the improbability of two acetaldehyde molecules inhabiting the same particle at the same time by considering a continuous aerosol volume in 1 L of air and using the room-temperature reaction rate, the reaction is still extremely unlikely. This result is due to both the slow rate of reaction (even at room temperature) and the second-order dependence on acetaldehyde, which has a low solution-phase concentration (i.e., mathematically squaring a very small number). Dissolution and reaction of acetaldehyde

in the upper troposphere/lower stratosphere are therefore inconsequential processes in terms of a sink for acetaldehyde, or accumulation of organic material in sulfate particles.

Even though processing of acetaldehyde by UT/LS sulfate is not atmospherically significant, this study has implications for atmospheric chemistry. First of all, solubility of oxygenated organic compounds can be significantly enhanced by solution-phase equilibria. Secondly, aldol condensation-dehydration can take place at middle acidities, cold temperatures, and via uptake from the gas phase. A high enolization constant is not a requirement for reaction, but both water and proton activities are necessary components for aldol condensation. This study shows that a better candidate as a gaseous precursor to accumulation of organic material in upper tropospheric sulfate particles via dissolution and reaction would have either a much faster reaction rate, be first order in the organic species, or both. Finally, Henry's law may be an insufficient description of the dissolution process. In fact, small amounts of organic content in a sulfate particle may increase the uptake of more organics. This possibility is currently under study in our laboratory.

Acknowledgements

This work was performed while R. R. Michelsen held a National Research Council Associateship Award at NASA Ames Research Center. S. F. M. Ashbourn was supported through the Camille and Henry Dreyfus Foundation Postdoctoral Program in Environmental Chemistry. The authors thank D. Knopf and B. P. Luo for values from their sulfuric acid model, and the NASA Upper Atmosphere Research and New Investigators Programs for funding.

References

Bagno, A., V. Lucchini, and G. Scorrano (1991), Thermodynamics of protonation of ketones and esters and energies of hydration of their conjugate acids, *J. Phys. Chem.*, *95*(1), 345-352.

Baigrie, L. M., R. A. Cox, H. Slebocka-Tilk, M. Tencer, and T. T. Tidwell (1985), Acid-catalyzed enolization and aldol condensation of acetaldehyde, *J. Amer. Chem. Soc.*, *107*(12), 3640-3645.

Benkelberg, H.-J., S. Hamm, and P. Warneck (1995), Henry's law coefficients for aqueous solutions of acetone, acetaldehyde and acetonitrile, and equilibrium constants for the addition compounds of acetone and acetaldehyde with bisulfite, *J. Atmos. Chem.*, *20*, 17-34.

Chiang, Y., M. Hojatti, J. R. Keeffe, A. J. Kresge, N. P. Schepp, and J. Wirz (1987), Vinyl alcohol: generation and decay kinetics in aqueous solution and determination of the tautomerization equilibrium constant and acid dissociation constants of the aldehyde and enol forms, *J. Amer. Chem. Soc.*, *109*(13), 4000-4009.

Clegg, S. L., P. Brimblecombe, and A. S. Wexler (1998), A thermodynamic model of the system H-NH_4-SO_4-NO_3-H_2O at tropospheric temperatures., *J. Phys. Chem. A*, *102*, 2137-2154.

Cox, R. A. (2000), Excess acidities, *Adv. Phys. Org. Chem.*, *35*, 1-66.

Duncan, J. L., L. R. Schindler, and J. T. Roberts (1998), A new sulfate-mediated reaction: Conversion of acetone to trimethylbenzene in the presence of liquid sulfuric acid, *Geophys. Res. Lett.*, *25*(5), 631-634.

Duncan, J. L., L. R. Schindler, and J. T. Roberts (1999), Chemistry at and near the surface of liquid sulfuric acid: A kinetic, thermodynamic, and mechanistic analysis of heterogeneous reactions of acetone, *J. Phys. Chem. B*, *103*(34), 7247-7259.

Finlayson-Pitts, B. J., and J. Pitts (2000), *Chemistry of the Upper and Lower Atmosphere*, 969 pp., Academic Press, San Diego.

Fujiwara, Y., and S. Fujiwara (1963), Nuclear magnetic resonance study of acetaldehyde aqueous solution, *Bull. Chem. Soc. Japan*, *36*(5), 574-578.

Golden, D. M., G. N. Spokes, and S. W. Benson (1973), Very low-pressure pyrolysis (VLPP): A versatile kinetic tool, *Ang. Chem.*, *12*(7), 534-546.

Guthrie, J. P. (1990), Thermodynamics of enols, in *The Chemistry of Enols*, edited by Z. Rappaport, pp. 75-93, John Wiley & Sons, New York.

Huthwelker, T., T. Peter, B. P. Luo, S. L. Clegg, K. S. Carslaw, and P. Brimblecombe (1995), Solubility of HOCl in water and aqeous H_2SO_4 to stratospheric temperatures, *J. Atmos. Chem.*, *21*, 81-95.

Imamura, T., and H. Akiyoshi (2000), Uptake of acetone into sulfuric-acid solutions, *Geophys. Res. Lett.*, *27*(9), 1419-1422.

Iraci, L. T., A. M. Essen, and D. M. Golden (2002), Solubility of methanol in low-temperature aqueous sulfuric acid and implications for atmospheric particle composition, *J. Phys. Chem. A*, *106*, 4054-4060.

Iraci, L. T., R. R. Michelsen, S. F. M. Ashbourn, and S. J. R. Staton (2003), Estimating uptake of small organic compounds by UT/LS aerosols: Dissolution and reaction, paper presented at *Gordon Conference on Atmospheric Chemistry*, Big Sky, Montana, USA.

Iraci, L. T., and M. A. Tolbert (1997), Heterogeneous interaction of formaldehyde with cold sulfuric acid: Implications for the upper troposphere and lower stratosphere, *J. Geophys. Res.*, *102*(D13), 16099-16107.

Jang, M., B. Carrol, B. Chandramouli, and R. M. Kamens (2003), Particle growth by acid-catalyzed heterogeneous reactions of organic carbonyls on preexisting aerosols, *Environ. Sci. Tech.*, *37*, 3828-3837.

Jang, M., and R. M. Kamens (2001), Atmospheric secondary aerosol formation by heterogeneous reactions of aldehydes in the presence of a sulfuric acid aerosol catalyst, *Environ. Sci. Tech.*, *35*, 4758-4766.

Jayne, J. T., D. R. Worsnop, C. E. Kolb, E. Swartz, and P. Davidovits (1996), Uptake of gas-phase formaldehyde by aqueous acid surfaces, *J. Phys. Chem.*, *100*(19), 8015-8022.

Kane, S. M., and M. T. Leu (2001), Uptake of methanol vapor in sulfuric acid solutions, *J. Phys. Chem. A*, *105*(9), 1411-1415.

Kane, S. M., R. S. Timonen, and M. T. Leu (1999), Heterogeneous chemistry of acetone in sulfuric acid solutions: Implications for the upper troposphere, *J. Phys. Chem. A*, *103*(46), 9259-9265.

Klassen, J. K., J. Lynton, D. M. Golden, and L. R. Williams (1999), Solubility of acetone in low-temperature (210 - 240 K) sulfuric acid solutions, *J. Geophys. Res.*, *104*(D21), 26355-26361.

Knopf, D. A., B. P. Luo, U. K. Krieger, and T. Koop (2003), Thermodynamic dissociation constant of the bisulfate ion from Raman and ion interaction modeling studies of aqueous sulfuric acid at low temperatures, *J. Phys. Chem. A*, *107*(21), 4322-4332.

Levy, G. C., J. D. Cargioli, and W. Racela (1970), Nuclear magnetic resonance determination of ketone basicity and the use of ketones as indicators for evaluation of medium acidity, *J. Amer. Chem. Soc.*, *92*(21), 6238-6246.

Michelsen, R. R., and J. T. Roberts (2004), The pressure-dependent kinetics of acetone uptake by sulfuric acid: evidence of a second-order heterogeneous reaction, *Atmos. Environ.*, in press.

Munro, D. C. (1968), Effects of acidity and extraction ratio in a solvent-extraction procedure for atomic absorption flame spectrophotometry, *Appl. Spectr.*, *22*(3), 199-200.

Murphy, D. M., D. S. Thompson, and M. J. Mahoney (1998), In situ measurements of organics, meteoritic material, mercury, and other elements in aerosols at 5 to 19 kilometers, *Science*, *282*(27 November), 1664-1669.

Myhre, C. E. L., D. H. Christensen, F. M. Nicolaisen, and C. J. Nielsen (2003), Spectroscopic study of aqueous H_2SO_4 at different temperatures and compositions: Variations in dissociation and optical properties, *J. Phys. Chem. A*, *107*(12), 1979-1991.

Nozière, B., and D. D. Riemer (2003), The chemical processing of gas-phase carbonyl compounds by sulfuric acid aerosols: 2,4-pentanedione, *Atmos. Environ.*, *37*(6), 841-851.

Reid, R. C., J. M. Prausnitz, and B. E. Poling (1987), *The Properties of Gases and Liquids*, 741 pp., McGraw-Hill Book Co., New York.

Rudakov, E. S., and A. I. Lutsyk (1979), The solubility of saturated hydrocarbons in aqueous sulphuric acid, *Russ. J. Phys. Chem.*, *53*(5), 731-733.

Rudakov, E. S., A. I. Lutsyk, and S. Y. Suikov (1987), Extremal change in solubility of non-electrolytes in the water-sulphuric acid system (0-100% H_2SO_4). modification of the sechenov equation, *Russ. J. Phys. Chem.*, *61*(5), 601-607.

Sander, S. P., R. R. Friedl, A. R. Ravishankara, D. M. Golden, C. E. Kolb, M. J. Kurylo, R. E. Huie, V. L. Orkin, M. J. Molina, G. K. Moortgat, and B. J. Finlayson-Pitts (2003), Chemical kinetics and photochemical data for use in atmospheric studies, report 02-25, Jet Propulsion Laboratory, Pasadena, CA.

Sanders, S. J. (1985), Modeling organics in aqueous sulfuric acid solutions, *Ind. Eng. Chem. Process Des. Dev.*, *24*, 942-948.

Sheridan, P. J., C. A. Brock, and J. C. Wilson (1994), Aerosol particles in the upper troposphere and lower stratosphere: Elemental composition and morphology of individual particles in northern midlatitudes, *Geophys. Res. Lett.*, *21*(23), 2587-2590.

Singh, H. B., Y. Chen, A. C. Staudt, D. J. Jacob, D. R. Blake, B. Heikes, and J. Snow (2001), Evidence from the Pacific tropopshere for large global sources of oxgenated organic compounds, *Nature*, *410*, 1078-1081.

Solomons, T. W. (1992), *Organic Chemistry*, John Wiley & Sons, New York.

Tabazadeh, A., O. B. Toon, S. L. Clegg, and P. Hamill (1997), A new parameterization of H_2SO_4/H_2O aerosol composition: Atmospheric implications, *Geophys. Res. Lett.*, *24*(15), 1931-1934.

Tucker, E. E., and S. D. Christian (1979), A prototype hydrophobic interaction. The dimerization of benzene in water, *J. Phys. Chem.*, *83*(3), 426-427.

Westh, P., C. A. Haynes, and Y. Koga (1998), How dilute is the Henry's law region? II, *J. Phys. Chem. B*, *102*(25), 4982-4987.

Williams, L. R., and F. S. Long (1995), Viscosity of supercooled sulfuric acid solutions, *J. Phys. Chem. B*, *99*, 3748-3751.

Zhang, R., P. J. Woolridge, J. P. D. Abbatt, and M. J. Molina (1993), Physical chemistry of the sulfuric acid/water binary system at low temperatures: stratospheric implications, *J. Phys. Chem.*, *97*, 7351-7358.

Figure 1. A typical uptake experiment at 226 K, 47 wt% H_2SO_4. Gas-phase acetaldehyde was detected as $m/z = 29$. Exposure to sulfuric acid begins at 0 s and ends at ~260 s as indicated.

Figure 2. Data analysis shows two types of behavior: a) linear, indicating simple solubility and b) curved, indicating steady-state loss. In experiment a, $T = 221$ K, the acid was 66 wt%, and $H^* = 6.7 \times 10^3$ M atm^{-1}. In experiment b, $T = 236$ K, the acid was 47 wt%, and $H^* = 2.9 \times 10^2$ M atm^{-1}. The open circles are data points, while the solid lines are best fits to the data. In b, the closed circles indicate data included in the linear fit.

Figure 3. A van't Hoff plot of the solubility measurements of acetaldehyde in cold sulfuric acid solutions. Solid triangles represent 76 wt% H_2SO_4, asterisks represent 66 wt% H_2SO_4, solid circles represent 47 wt%, and open grey squares represent 39 wt% H_2SO_4. The solid lines are linear best fits to the data with $\Delta S°$ fixed at -171 J mol^{-1} K^{-1}. The dotted line is an extrapolation of the solubility of acetaldehyde in water measured between 273 and 298 K from Benkelberg [1995]. The dashed line is a linear best fit for the 39 wt% acid allowing $\Delta S°$ to vary. See text for discussion.

Figure 4. A thermodynamic model of the speciation of acetaldehyde in sulfuric acid at 220 K. Our data are indicated by triangles, and the parameterization of the data is shown as a thick black line. The thin black line indicates the total acetaldehyde solubility according to the model. Contributions to overall solubility by molecular, hydrated and protonated acetaldehyde are shown as dashed and/or dotted grey lines and labeled. Enolized acetaldehyde does not appear on this scale as its solubility is $\sim 10^{-4}$ mol L^{-1} atm^{-1}, but it follows the shape of molecular acetaldehyde.

Table I. Measured Effective Henry's Law Coefficients for Uptake of Acetaldehyde into Sulfuric Acid

H_2SO_4 composition	T (K)	$H^*\sqrt{D}$ (M cm atm^{-1} s$^{-1/2}$)	D (cm^2 s^{-1})	H^* (M atm^{-1})	reaction observed?
76.2 wt%	211.4	3.437	5.88×10^{-10}	1.42×10^5	
	212.1	3.846	6.99×10^{-10}	1.45×10^5	
	220.9	2.534	4.37×10^{-9}	3.83×10^4	
	225.1	2.192	8.24×10^{-9}	2.41×10^4	
	225.5	2.080	8.74×10^{-9}	2.22×10^4	
	227.0	2.559	1.10×10^{-8}	2.44×10^4	
	227.2	0.918	1.13×10^{-8}	8.62×10^3	
	229.1	1.230	1.47×10^{-8}	1.01×10^4	
	231.3	2.159	1.92×10^{-8}	1.56×10^4	
	231.4	1.653	1.95×10^{-8}	1.18×10^4	
	240.7	0.967	5.14×10^{-8}	4.27×10^3	
	240.9	0.903	5.24×10^{-8}	3.95×10^3	
66.3 wt%	216.5	1.376	2.08×10^{-8}	9.54×10^3	
	219.6	1.202	3.00×10^{-8}	6.94×10^3	
	220.6	1.232	3.35×10^{-8}	6.73×10^3	
	223.2	1.257	4.32×10^{-8}	6.05×10^3	rxn
	223.5	1.085	4.45×10^{-8}	5.14×10^3	
	231.0	0.346	9.06×10^{-8}	1.15×10^3	rxn
	231.3	0.701	9.28×10^{-8}	2.30×10^3	
	239.1	0.462	1.66×10^{-7}	1.13×10^3	
	239.2	0.372	1.67×10^{-7}	9.11×10^2	
	239.3	0.541	1.68×10^{-7}	1.32×10^3	
47.3 wt%	216.7	0.410	1.24×10^{-7}	1.17×10^3	
	219.7	0.967	1.61×10^{-7}	2.41×10^3	rxn
	223.5	0.548	2.17×10^{-7}	1.17×10^3	rxn
	225.7	0.575	2.57×10^{-7}	1.13×10^3	rxn
	226.2	0.329	2.66×10^{-7}	6.38×10^2	rxn
	229.7	0.283	3.40×10^{-7}	4.85×10^2	rxn
	236.1	0.203	5.08×10^{-7}	2.85×10^2	rxn
	239.9	0.159	6.31×10^{-7}	2.00×10^2	rxn
38.5 wt%	214.5	1.074	1.27×10^{-7}	3.01×10^3	
	215.5	1.896	1.39×10^{-7}	5.08×10^3	
	215.6	1.602	1.40×10^{-7}	4.28×10^3	rxn
	218.4	0.724	1.79×10^{-7}	1.71×10^3	
	219.7	0.529	2.01×10^{-7}	1.18×10^3	
	220.5	0.615	2.15×10^{-7}	1.33×10^3	
	222.0	0.580	2.48×10^{-7}	1.17×10^3	rxn
	228.1	0.370	3.88×10^{-7}	5.94×10^2	

Table II. Thermodynamic Parameters for Acetaldehyde Dissolution in Aqueous Sulfuric Acid

H_2SO_4 composition	$x_{H_2SO_4}$	M_{solv}[a] (mol L^{-1})	$\Delta H°$ (kJ mol^{-1})	$\Delta S°$ (J $mol^{-1} K^{-1}$)
water	0.00	55.6	-47.4	-171
38.5 wt%	0.10	46.0	-62.0	-252
47.3 wt%	0.14	41.9	-42.1	-162
66.3 wt%	0.27	30.7	-43.3	-152
76.2 wt%	0.37	23.3	-51.6	-172
38.5 wt%	0.10	46.0	-44.2	-171
47.3 wt%	0.14	41.9	-44.1	-171
66.3 wt%	0.27	30.7	-47.6	-171
76.2 wt%	0.37	23.3	-51.4	-171

[a]Calculated at 220 K.

Table III. Model of Acetaldehyde Speciation in Cold H_2SO_4[a]

Process	*Reaction*	*Definitions*	*Literature Values*
dissolution[b]	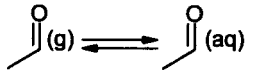	$H_{mol} = \frac{H_{mol}^{H_2O}}{f}$	
hydration	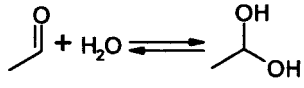	$H_h = H_{mol} K_h a_w$	$K_h = 0.0221$[c] $\Delta H_h^\circ = -20.5$ kJ/mol[c]
protonation[d]	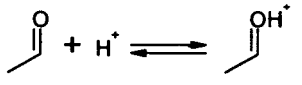	$H_a = H_{mol} \cdot [H^+] \cdot 10\text{^}(pK_a + m^* X)$	$pK_a = -3.57$[e] $m^* = 0.35$[f] $\Delta H_a^\circ = 0.837$ kJ/mol[f]
enolization	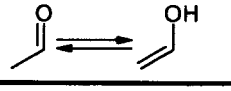	$H_e = H_{mol} K_e$	$pK_e = 6.23$[g] $\Delta H_e^\circ = 38.1$ kJ/mol[h]

[a]For each process, H is the solubility, K is the equilibrium constant, and $\Delta H°$ is the enthalpy. Water activity is indicated as a_w, and X and m^* are excess acidity and slope, respectively. See text for definitions. [b]The solubility of molecular acetaldehyde in water, $H_{mol}^{H_2O} = H^* / (1 + K_h a_w)$ where H^* is the value from [*Benkelberg et al.*, 1995]; the activity coefficient f is a piece-wise function based on the solubility of cyclohexane in H_2SO_4 [*Rudakov and Lutsyk*, 1979]. From 0-30 wt% H_2SO_4, $f = 16.7x+1$ and from 35 to 80 wt% H_2SO_4, $f = -4.2x+2.8$, where x is the mole fraction of acid. [c]Value from [*Fujiwara and Fujiwara*, 1963] divided by 55.6 M. [d]Treated with the excess acidity method [*Cox*, 2000]. [e]Hammett acidity at half protonation [*Levy et al.*, 1970], multiplied by m^* to convert to the excess acidity scale. [f]Values for acetone [*Bagno et al.*, 1991]. [g][*Chiang et al.*, 1987]. [h][*Guthrie*, 1990].

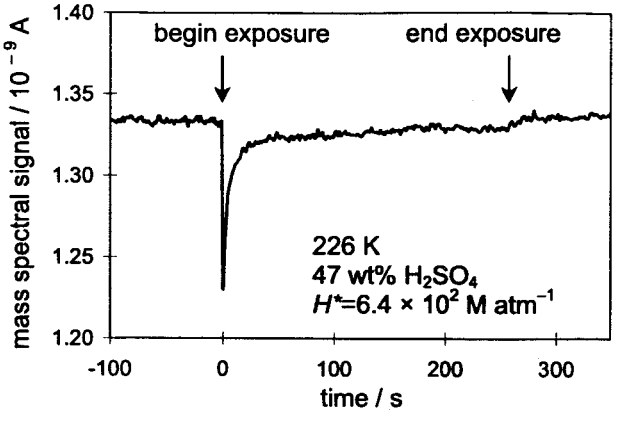

Figure 1. A typical uptake experiment at 226 K, 47 wt% H_2SO_4. Gas-phase acetaldehyde was detected as m/z = 29. Exposure to sulfuric acid begins at 0 s and ends at ~260 s as indicated.

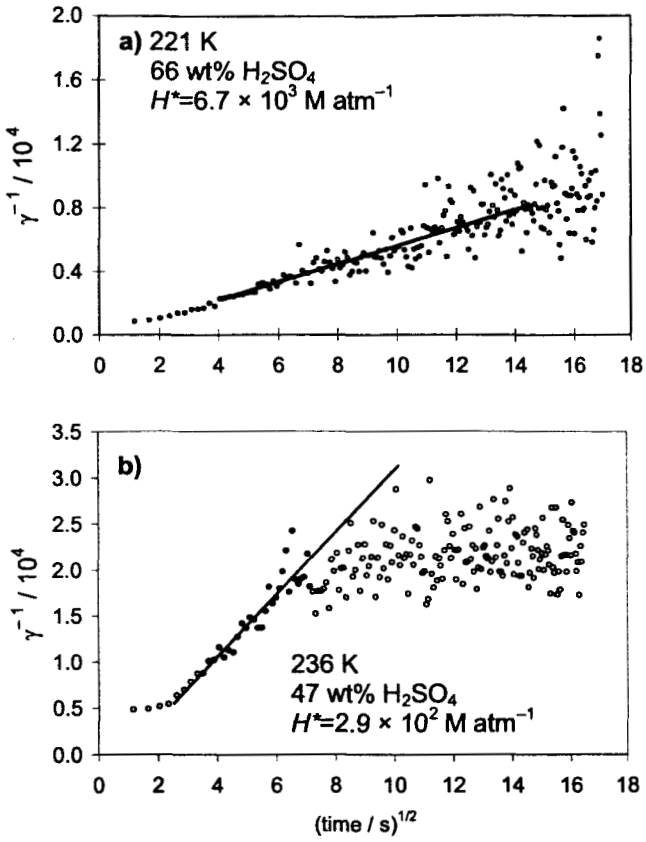

Figure 2. Data analysis shows two types of behavior: a) linear, indicating simple solubility and b) curved, indicating steady-state loss. In experiment a, $T = 221$ K, the acid was 66 wt%, and $H^* = 6.7 \times 10^3$ M atm^{-1}. In experiment b, $T = 236$ K, the acid was 47 wt%, and $H^* = 2.9 \times 10^2$ M atm^{-1}. The open circles are data points, while the solid lines are best fits to the data. In b, the closed circles indicate data included in the linear fit.

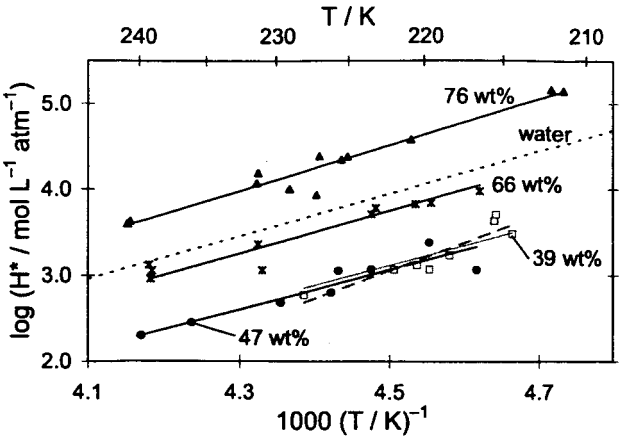

Figure 3. A van't Hoff plot of the solubility measurements of acetaldehyde in cold sulfuric acid solutions. Solid triangles represent 76 wt% H_2SO_4, asterisks represent 66 wt% H_2SO_4, solid circles represent 47 wt%, and open grey squares represent 39 wt% H_2SO_4. The solid lines are linear best fits to the data with $\Delta S°$ fixed at -171 J mol^{-1} K^{-1}. The dotted line is an extrapolation of the solubility of acetaldehyde in water measured between 273 and 298 K from Benkelberg [1995]. The dashed line is a linear best fit for the 39 wt% acid allowing $\Delta S°$ to vary. See text for discussion.

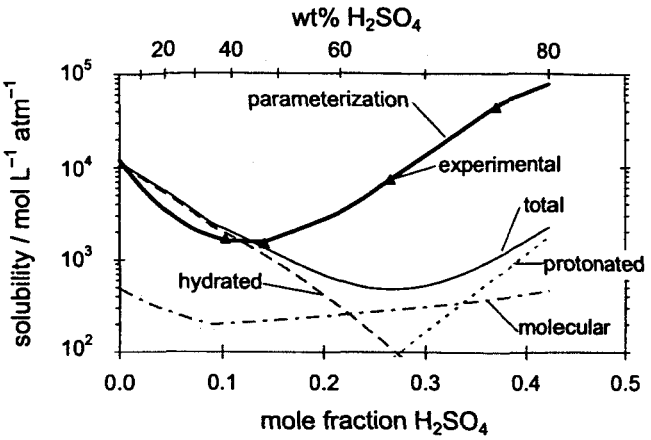

Figure 4. A thermodynamic model of the speciation of acetaldehyde in sulfuric acid at 220 K. Our data are indicated by triangles, and the parameterization of the data is shown as a thick black line. The thin black line indicates the total acetaldehyde solubility according to the model. Contributions to overall solubility by molecular, hydrated and protonated acetaldehyde are shown as dashed and/or dotted grey lines and labeled. Enolized acetaldehyde does not appear on this scale as its solubility is ~10^{-4} mol L^{-1} atm^{-1}, but it follows the shape of molecular acetaldehyde.

Abstract

Primary biogenic emissions of methanol are estimated to provide more than 25% of the global sources of this oxygenated VOC, and methanol emissions represent ~ 6% of identified terrestrial biogenic organic carbon sources to the atmosphere. Typical surface concentrations of 10 ppbv in forested regions, as compared to 2 ppbv in remote continental areas, highlight the importance of biogenic sources of methanol (CH_3OH).

With an atmospheric lifetime on the order of 10 days, methanol is the dominant oxygenated organic compound in the background mid to upper troposphere (0.2 - 1 ppbv). It is soluble in acidic solutions and water, which make up the majority of particles in the upper troposphere. Thus, the chemical behavior of methanol in aerosol particles and cloud droplets warrants consideration.

Methanol reacts with nitric acid (HNO_3) in concentrated sulfuric acid solutions, and we wish to understand the possible role of this reaction under atmospheric conditions. Thus, we have begun studies of the temperature and acidity dependence of the reaction to form *methyl nitrate*:

$$CH_3OH + HNO_3 \rightarrow CH_3ONO_2 + H_2O.$$

Methyl nitrate production would be followed in the atmosphere by photolysis to yield NO_2. This conversion of HNO_3 back to NO_2 may suggest that some fraction of NO_x can be liberated by aerosol reactions before nitric acid is removed from the atmosphere by wet deposition.

Experimental Design

$$HNO_3 + CH_3OH \rightarrow CH_3ONO_2 + H_2O$$

- Estimate upper troposphere/lower stratosphere (UT/LS) conditions and aerosol composition
- Initiate methanol and acid reaction, varying reactant concentrations, acidity and temperature independently
- Monitor product production using IR spectroscopy—compare results to reactant spectra
  - IR radiation excites molecular vibrations and can be used to identify products
  - Kinetic data can be derived by monitoring peak height vs. time
- Quantify product using known cross-sections
- Derive rate constants and energy of activation
- Explore effect of acidity on rate of reaction

Schematic of Apparatus

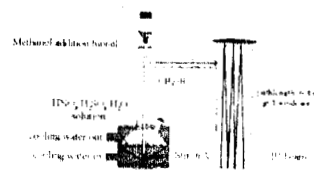

Reactant Spectra

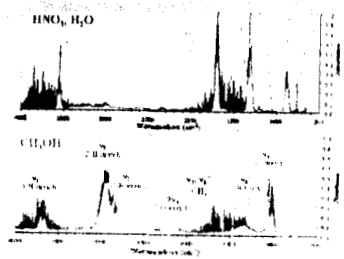

Product Spectra after 314 min—50 wt% H_2SO_4 at 20°C

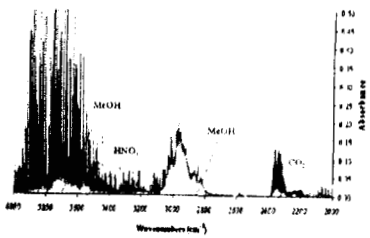

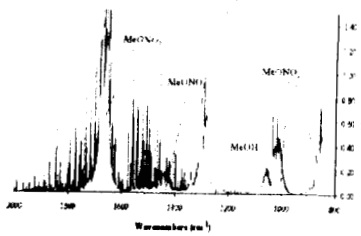

Observations

50 wt% H_2SO_4

- Same products at all temperatures observed
- CH_3ONO_2 is dominant gas phase product
- HNO_3 and CH_3OH concentrations do not depreciate detectably over 3 hours
- All bands identifiable

- Growth starts later when reaction temperature is reduced
- 0.01-0.4% yield of CH_3ONO_2 over 10-30°C after 160 min when 0.1 ml methanol reacted

60 wt% H_2SO_4

- Same products at all temperatures observed
- CH_3ONO_2 is dominant gas phase product
- HNO_3 and CH_3OH concentrations decreased appreciably during experiment
- A set of unidentified bands grows in at 2459 cm^{-1}, 2260 cm^{-1} and elsewhere
  - May be harmonics of fundamentals
- Growth starts later when reaction temperature is reduced
- 0.03-0.3% yield of CH_3ONO_2 over 10-20°C after 160 min when 1.0 ml methanol reacted
- NO_2 observed at later stages of reaction
- No apparent dependence on initial reactant concentration

Determining Reaction Order

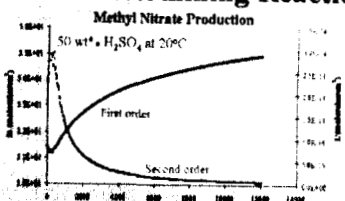

- If methyl nitrate formation were a first order process, ln(concentration) vs. time would be linear
- If methyl nitrate formation were a second order process, 1/(concentration) vs. time would be linear

Zeroth Order Rate Constants

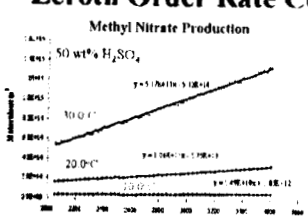

- Zeroth order plot, concentration vs. time, is linear
- Rate constant k is slope of best fit line
- k increases by a factor of 7 when T is raised from 10°C to 20°C
- k increases by a factor of 5 when T is raised from 20°C to 30°C

Arrhenius Plot

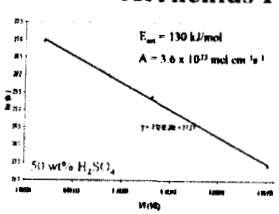

- The energy of activation for the reaction, E_{act} is calculated from the slope of best fit line
- The pre-exponential factor, A, is given by the intercept
- E_{act} for 60 wt% solution is 210 kJ/mol

Effect of Acidity on Methyl Nitrate Production

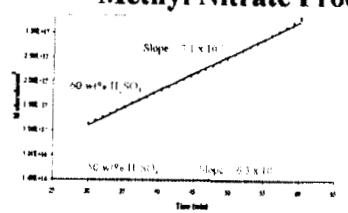

- Reaction rate is very sensitive to pH
- Rate in 50 wt% H_2SO_4 is 1000 times slower than in 60 wt%

Conclusions

- The reaction of methanol with nitric acid to produce methyl nitrate appears to be zeroth order
  - Concentration of product vs. time is linear
  - Product formation is independent of reactant concentration
- Rate increases dramatically with temperature
- Rate constant is very sensitive to solution composition
- Activation energy for reaction in 60 wt % H_2SO_4 is almost twice that in 50%

Implications

Understanding and implementation of HNO_3 processing in atmospheric models remains problematic. Rarely do models reproduce HNO_3/NO_y partitioning correctly when compared to field measurements, and different processes are commonly invoked to explain these discrepancies. While several recent studies attribute overestimates of HNO_3/NO_y to formation of NO_x by lightning, precipitation scavenging of HNO_3, and gas-aerosol partitioning (*Staudt et al.*, 2003; *Bey et al.*, 2001), others find that multiphase chemical processes could explain some or all of the discrepancies (*Olson et al.*, 2001; *Schultz et al.*, 2000). If the reaction of methanol with nitric acid discussed here is shown to occur under conditions of the UT/LS, it may provide a nitric acid sink with slow release of NO_x, as advocated by *Wang et al.* (1998). Further experiments which probe the reactivity of methanol in partially or fully neutralized solutions (as well as those with low ionic strength) are clearly warranted if the importance of this reaction under a variety of tropospheric conditions is to be assessed.

Future Work

- Conduct experiments over a variety of solution compositions
- Explore other temperatures
- Compare dependence of rate on concentrations of NO^+ and other reactive species present in $H_2SO_4/HNO_3/H_2O$ solutions
- Monitor liquid phase IR
- Optimize reaction conditions to allow monitoring of methanol consumption

Bibliography

Acknowledgements

- The authors would like to thank for their support:
- NASA New Investigator Program
- NASA Upper Atmosphere Research Program
- John Orlando for providing methyl nitrate cross-sections

The Acid Catalyzed Nitration of Methanol:

Brent Riffel, Rebecca Michelsen and Laura Iraci

Background

Abstract

The liquid phase acid catalyzed reaction of methanol (CH_3OH) with nitric acid (HNO_3) to yield methyl nitrate (CH_3ONO_2) under atmospheric conditions has been investigated using gas phase infrared spectroscopy. This nitration reaction is expected to occur in acidic aerosol particles found in the upper troposphere/lower stratosphere as highly soluble methanol and nitric acid diffuse into these aerosols. Gaseous methyl nitrate is released upon formation, suggesting that some fraction of NO_x may be liberated from nitric acid (methyl nitrate is later photolyzed to NO_x) before it is removed from the atmosphere by wet deposition. Thus, this reaction may have important implications for the NO_x budget.

Reactions have been initiated in 45-64 wt% H_2SO_4 solutions at 283K. Methyl nitrate production rates increased exponentially with acidity within the acidity regime studied. Calculations suggest that the nitronium ion (NO_2^+) is the active nitrating agent under these conditions. The nitration is first order in nitronium and methanol at all acidities investigated.

Under conditions with high relative methanol concentrations, a second order rate constant, k_2, has been calculated to be 5 x 10^7 $M^{-1}s^{-1}$; when the methanol concentration is low a rate constant of 1 x 10^8 $M^{-1}s^{-1}$ is observed. Although the reason for this observation is still unclear, the larger rate constant is more applicable for this reaction in the troposphere. The very small percentage of nitric acid in the nitronium ion form probably makes this reaction insignificant for the upper troposphere. This nitration may become significant in the mid-stratosphere where colder temperatures increase nitric acid solubility and higher sulfuric acid content shifts nitric acid speciation toward the nitronium ion.

Experimental Design

$HNO_3 + CH_3OH \rightarrow CH_3ONO_2 + H_2O$

- Estimate upper troposphere/lower stratosphere (UT/LS) conditions and aerosol composition
  - Free tropospheric aerosols are 40-70 wt% H_2SO_4
  - 800-1200 ppt CH_3OH
  - 100-600 ppt HNO_3
- Initiate methanol and nitric acid reaction, varying reactant concentrations, acidity and temperature independently
- Monitor product yield using infrared spectroscopy—compare results to reactant spectra
  - IR spectroscopy examines molecular vibrations and can be used to identify products
  - Kinetic data can be derived by monitoring peak height vs. time
  - Rate of reaction calculated as moles of methyl nitrate produced per liter per min (M/min)
- Quantify product using literature cross-section data
- Calculate speciation of nitric acid and methanol in H_2SO_4
- Derive second order rate constants, k_2 = rate/reactant concentrations
- Explore effect of acidity on rate of reaction
- Investigate rate dependence on reactant concentration
- Calculate methyl nitrate production rate under tropospheric conditions

Wt % H_2SO_4	Mol Fraction H_2SO_4	$[CH_3OH]_{init}$	$[HNO_3]_{init}$
44.3	0.128	0.21	0.01
49.3	0.152	0.20	0.01
54.7	0.183	0.19	0.02
58.5	0.207	0.18	0.02
59.5	0.214	0.17	0.02
61.9	0.231	0.17	0.02
61.9	0.231	3.3E-04	0.02
61.9	0.231	1.3E-03	0.02
61.9	0.231	2.0E-03	0.02
61.9	0.231	2.7E-03	0.02
61.9	0.231	3.3E-03	0.02
61.9	0.231	0.05	0.02
61.9	0.231	0.10	0.02
59.5	0.214	3.5E-03	0.20
59.5	0.214	0.02	0.20
59.5	0.214	0.17	0.20
49.3	0.152	4.0E-03	0.11
49.3	0.152	0.12	0.11
49.3	0.152	0.20	0.11
[illegible]	[illegible]	[illegible]	[illegible]
44.2	0.142	0.04	0.10

The data sets are color coded according to the changing variable as follows. All other variables are held constant. This color scheme is consistent throughout the poster.

Varying acidity—constant CH_3OH

Varying CH_3OH:

– 62 wt% H_2SO_4

– 60 wt% H_2SO_4

– 47 wt% H_2SO_4

Varying HNO_3: [illegible] wt% H_2SO_4

50 wt% H_2SO_4 – 10x more HNO_3 than all others

Concentrations in table are calculated molecular concentrations, not analytical

Apparatus

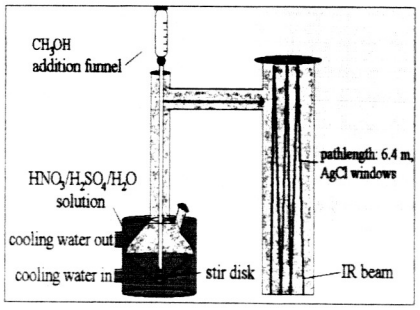

HNO_3 and CH_3OH Speciation in H_2SO_4

$H_2SO_4 \rightleftharpoons HSO_4^- + H^+$ $\quad$ $HNO_3 + H_2O \rightleftharpoons NO_3^- + H_3O^+$

$H^+ + CH_3OH \rightleftharpoons HSO_4^- + CH_3OH_2^+$ $\quad$ $H^+ + HNO_3 \rightleftharpoons NO_2^+ + H_2O$

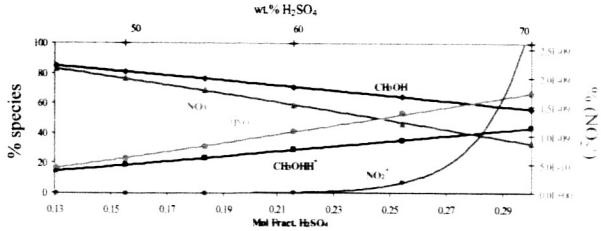

Percent speciation for ionic species present. Calculated* percentages are out of the total stoichiometric quantities of the respective parent compound.

Based on pKa and m values from:
Sampoli et al. *J. Phys. Chem.*, 1985, Vol. 89, Number 13, pp. 2864-9
Cox, R. *Advances in Physical Organic Chemistry*, Vol. 35, pp. 1 – 59.

Atmospheric Implications

Free tropospheric aerosols are 40 – 70 wt% H_2SO_4. In this acidity regime, the percentage of nitrogen in the form NO_2^+ (the likely nitrating agent) is extremely low—1 x 10^{-13} – 3 x 10^{-9}%. Appreciable quantities of NO_2^+ are not prevalent until about 80 wt% H_2SO_4. Thus, NO_2^+ is the limiting reagent under atmospheric conditions and methyl nitrate formation will be enhanced as the acidity increases, converting more HNO_3 to NO_2^+. The exponential nature of this speciation suggests it will control NO_2^+ concentrations, despite decreasing overall HNO_3 solubility as acidity increases.

Three different sets of free tropospheric conditions are tabulated to the right. Condition C was chosen to investigate the perturbed layer observed by Brock *et al.* (J. Geophys. Res., in press). The plot to the right shows the calculated ppt/min. of methyl nitrate released by this reaction for these calculated conditions as a function of wt% H_2SO_4 solution. This reaction may be important in the mid-stratosphere where colder temperatures enhance HNO_3 solubility, leading to aerosols containing up to 10 wt% nitric acid. Additionally, the increased acidity (up to 80 wt% H_2SO_4) of stratospheric aerosols shifts the speciation of HNO_3 towards NO_2^+.

Conditions	ppt CH_3OH	ppt HNO_3	Aerosol volume ($\mu m^3/cm^3$)	T (K)
A	800	100	0.5	280
B	800	100	2	280
C	1200	600	4	280

Conditions	Wt% H_2SO_4	$[HNO_3]$	$[NO_2^+]$	$[CH_3OH]$
A				
B	44.2	7.4E-09	3.6E-24	4.8E-10
	49.3	4.8E-09	1.3E-23	5.8E-10
	54.7	2.1E-09	4.5E-23	7.8E-10
	58.5	1.3E-09	1.4E-22	1.1E-09
	59.5	1.2E-09	2.0E-22	1.2E-09
	61.9	7.9E-10	4.1E-22	1.5E-09
	65.0	3.8E-10	1.0E-21	2.5E-09
	70.0	2.0E-10	1.1E-20	7.7E-09
C	44.2	4.4E-08	4.3E-23	7.2E-10
	49.3	2.9E-08	1.6E-22	8.6E-10
	54.7	1.3E-08	5.4E-22	1.2E-09
	58.5	8.1E-09	1.7E-21	1.6E-09
	59.5	7.2E-09	2.4E-21	1.8E-09
	61.9	4.7E-09	4.9E-21	2.3E-09
	65.0	2.3E-09	1.3E-20	3.7E-09
	70.0	1.2E-09	1.3E-19	1.2E-08

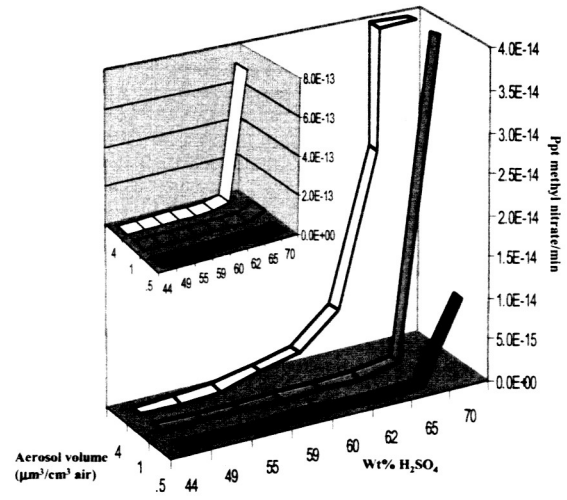

The plots above show the predicted production rates of methyl nitrate in ppt/min under three different atmospheric conditions. The blue trace is calculated for conditions A (tabulated to the left), the red trace shows conditions B and the yellow trace shows conditions C. These calculations use the second order rate constant calculated at 10°C. This plot clearly shows the sensitivity of the reaction to acidity and to the aerosol volume.

Formation of Methyl Nitrate via Aerosol Chemistry

NASA Ames Research Center, Moffett Field, CA 94035

Results and Analysis

Reaction Progression

Reaction progression shown for 62wt% H_2SO_4 experiment at 283K. Analytical reactant concentrations are as follows: $[CH_3OH]_{in}$ = .005 M and $[HNO_3]_{in}$ = .048 M.

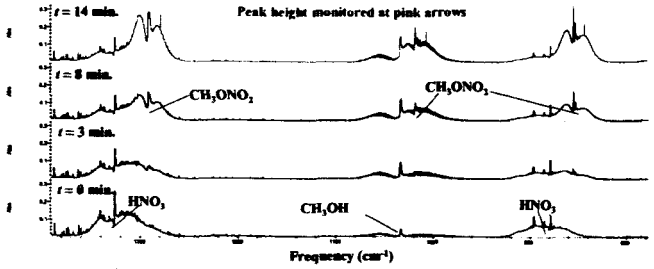

Acidity Dependence

The nitration rate of methanol increases exponentially with mole fraction sulfuric acid. Thus, the rate of methyl nitrate formation is extremely sensitive to acidity.

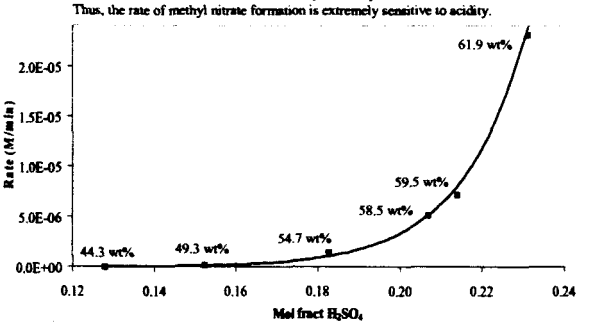

$[HNO_3]$ Dependence

If molecular HNO_3 is the active nitrating agent, then the rate law should be:

Rate=$k_2[CH_3OH][HNO_3]$ (assuming methanol is first order—this is discussed under $[CH_3OH]$ dependence) and rate = M/min.

Rate/$[CH_3OH]$ vs. $[HNO_3]$ should be linear. As can be seen below, the relationship is not linear, suggesting that the mechanism is more complicated than that shown in the experimental design.

Note: $[HNO_3]$ is calculated molecular nitric acid, not the total HNO_3 added

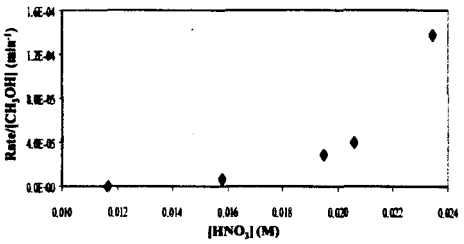

$[NO_2^+]$ Dependence

Rate/$[CH_3OH]$ vs. $[NO_2^+]_{calc.}$ is linear, suggesting that NO_2^+ is the active nitrating agent. The reason that the observed nitration rate increases exponentially with acidity is that $[NO_2^+]$ increases exponentially with acidity (see speciation plot left).

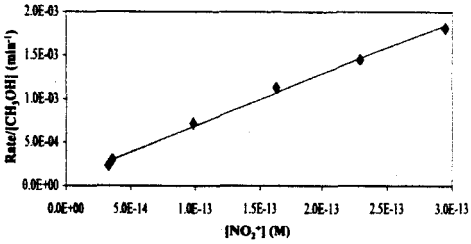

CH_3OH Dependence

If the reaction is first order in methanol, then a plot of rate/$[NO_2^+]$ vs. $[CH_3OH]$ should be linear. The 62 wt% data (pink) shows first order (linear) behavior in methanol for low methanol concentrations and it begins to flatten at larger concentrations—The large plot below is a blowup of the inset plot at low concentrations. The 50 wt% solutions (blue data in inset), which contain much more water than the 60 and 62 wt% solutions, show curved behavior as well at large relative methanol. It is presently unclear why deviation from linearity is observed at large relative methanol concentrations, but the plot below left shows that the reaction is still first order methanol in this regime.

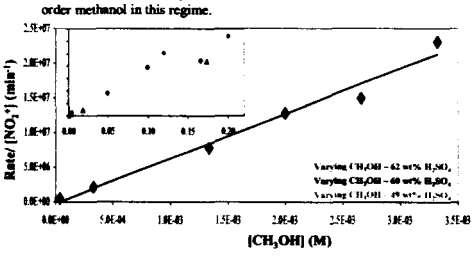

Reaction Order With Large $[CH_3OH]$

Even though the rate behavior in methanol changes from small methanol concentrations to large concentrations, a plot of Log $[CH_3OH]$ vs. Log (Rate/$[NO_2^+]$) for larger concentrations shows that the reaction is still first order in methanol at the larger concentrations (assuming first order in NO_2^+). This plot gives the order in CH_3OH as the slope and the second order rate constant as 10^b, where b is the intercept. It can be seen below for all of the experiments where $[CH_3OH]$ > 0.01 M, the order in methanol is one and the rate constant is $10^{7.8}$ = 6 x 10^7 $M^{-1}s^{-1}$. This differs significantly from the second order constant calculated above and to the right of 1 x 10^8 $M^{-1}s^{-1}$ for $[CH_3OH] \leq 0.004$ M. The reason for this behavior is still unclear.

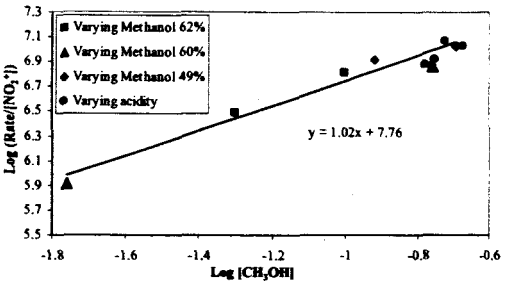

Rate vs. Reactants

This plot shows the different, but self-consistently linear behavior of the experiments with low methanol and those with high methanol. The slopes of the lines give the second order rate constants. It can be seen that the low methanol experiments in 62% H_2SO_4 and the varying nitric experiments (all use small methanol) obey the same rate law, while all other experiments with large methanol have the same smaller rate constant.

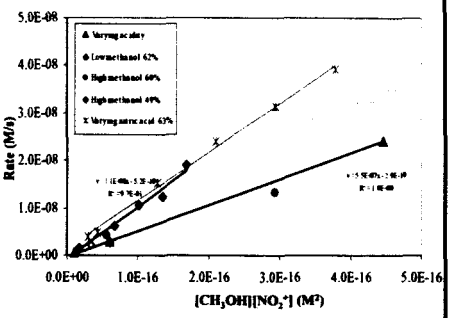

Discussion

Conclusions

- An acid catalyzed aqueous phase reaction between HNO_3 and CH_3OH in H_2SO_4 solutions has been observed using infrared spectroscopy. CH_3ONO_2 has been observed in the gas phase.
- Reaction rates increase exponentially with acidity
- Calculations suggest that NO_2^+ is the active nitrating reagent
- The reaction appears to be first order in NO_2^+ and CH_3OH
- A second order rate constant, k_2, has been calculated to be 1 x 10^8 $M^{-1}s^{-1}$
- Tropospheric calculations based on k_2 suggest that this nitration reaction is insignificant under UT/LS conditions
- Reaction may be important in the stratosphere where lower temperatures increase HNO_3 solubility and increased $[H_2SO_4]$ enhances the speciation of HNO_3 toward NO_2^+

Future Work

- Vary temperature at constant acidity and reactant concentration to determine temperature dependence and calculate activation energies
- Investigate cause of different kinetic behavior at high $[CH_3OH]$
- Explore diffusion behavior in IR cell to determine possible influence on monitoring kinetic behavior

Acknowledgements

- NASA New Investigator Program
- NASA Upper Atmosphere Research Program
- John Orlando for providing methyl nitrate cross-sections

Ames Research Center

NASA

Dissolution and Speciation of Oxygenated Organic Compounds in Sulfate Particles: Acetaldehyde

R. R. Michelsen, S. F. M. Ashbourn, and L. T. Iraci

NASA Ames Research Center

AGU Fall Meeting 2003

Overview & Focus

- Where is the organic content in upper tropospheric sulfate particles coming from?
- How does chemistry affect the solubility of oxygenated organic compounds?

- Experimental approach: Knudsen cell studies
- Results: acetaldehyde solubility in low-temperature H_2SO_4
- Speciation & effect on solubility
- Unexpected results: uptake enhancement
- Reaction, surface effect, and/or Henry's law deviation?

Experimental Approach: Knudsen Cell Studies

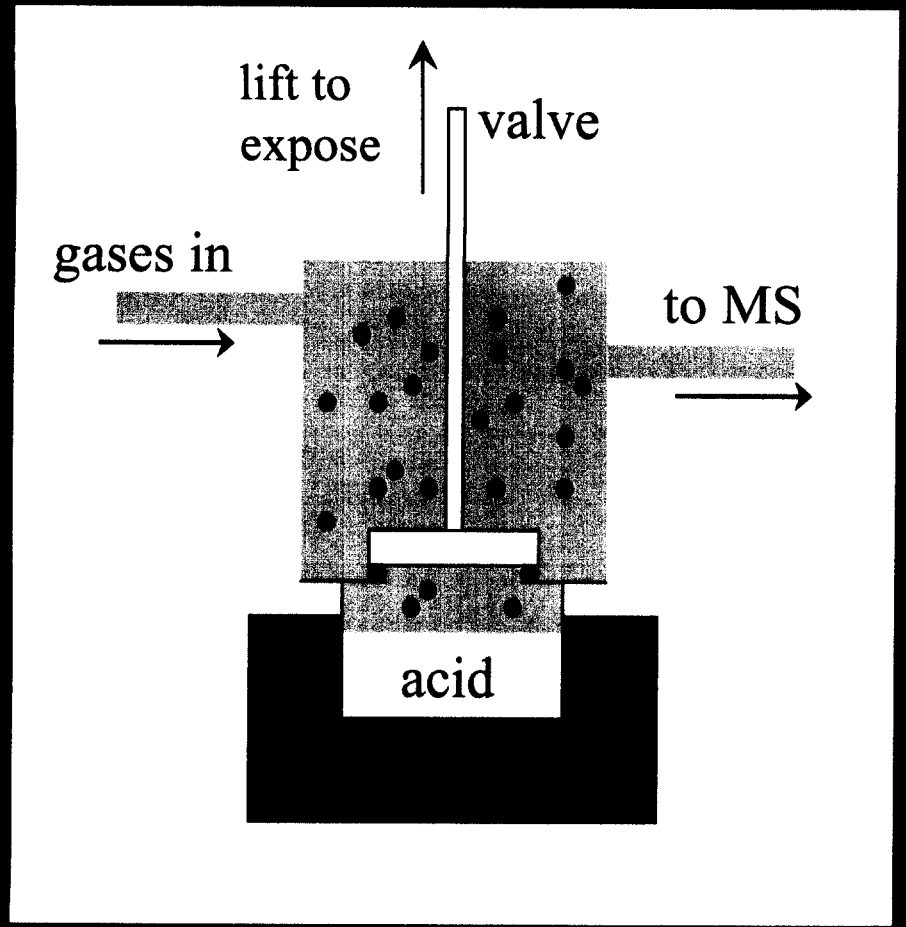

Analysis of Knudsen Cell Data

- The signal for gas-phase acetaldehyde ($m/z = 29$) drops when exposed to the acid.
- The fraction of molecules lost to the surface, γ, can be calculated from the data.

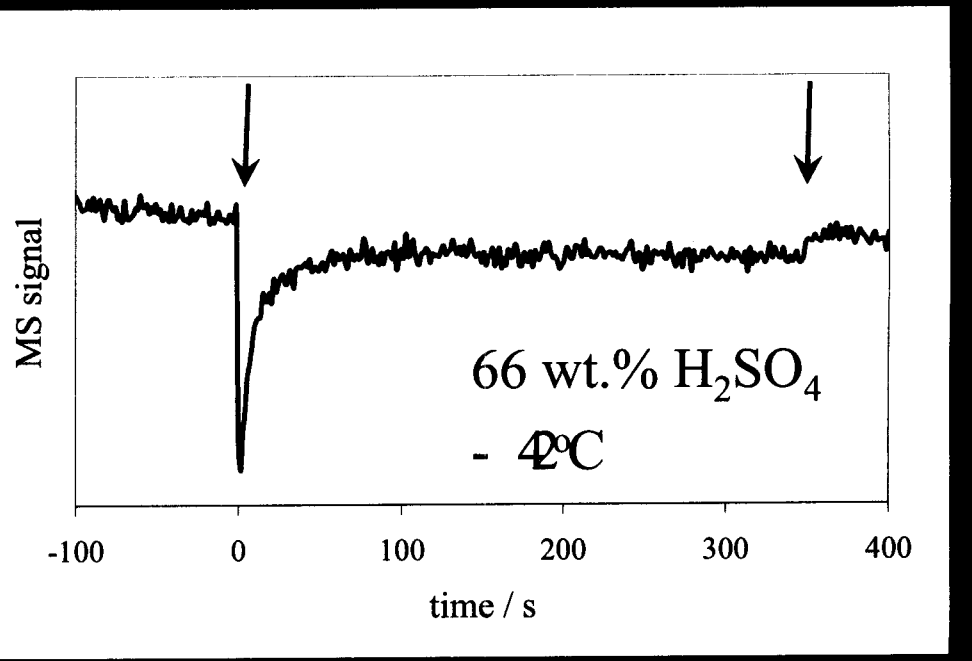

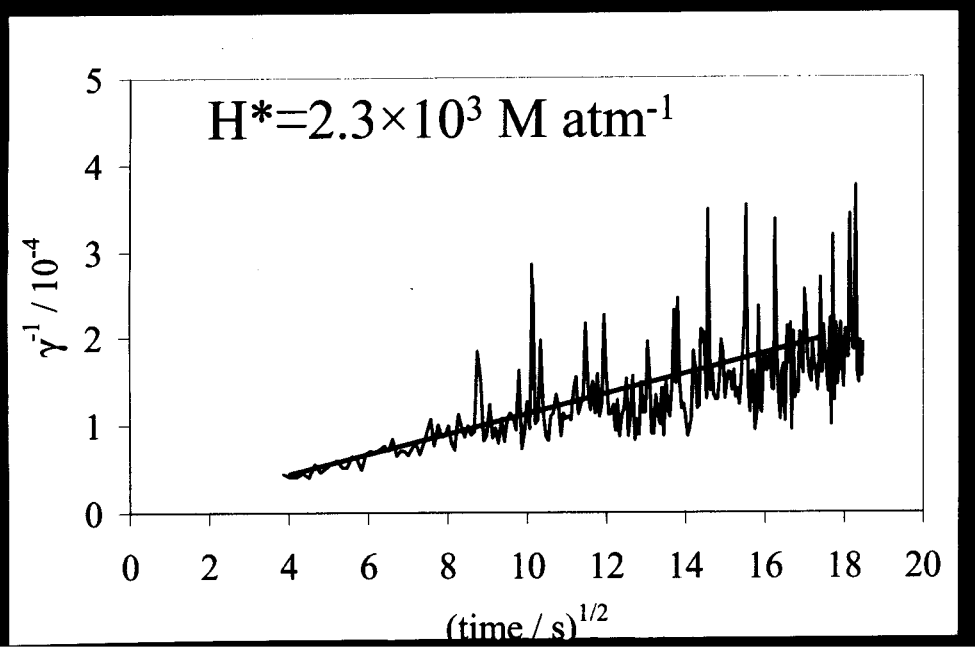

- For no reaction, plotting inverse γ versus $\sqrt{t}$ results in a straight line; H* can be calculated from the slope.

Acetaldehyde Solubility

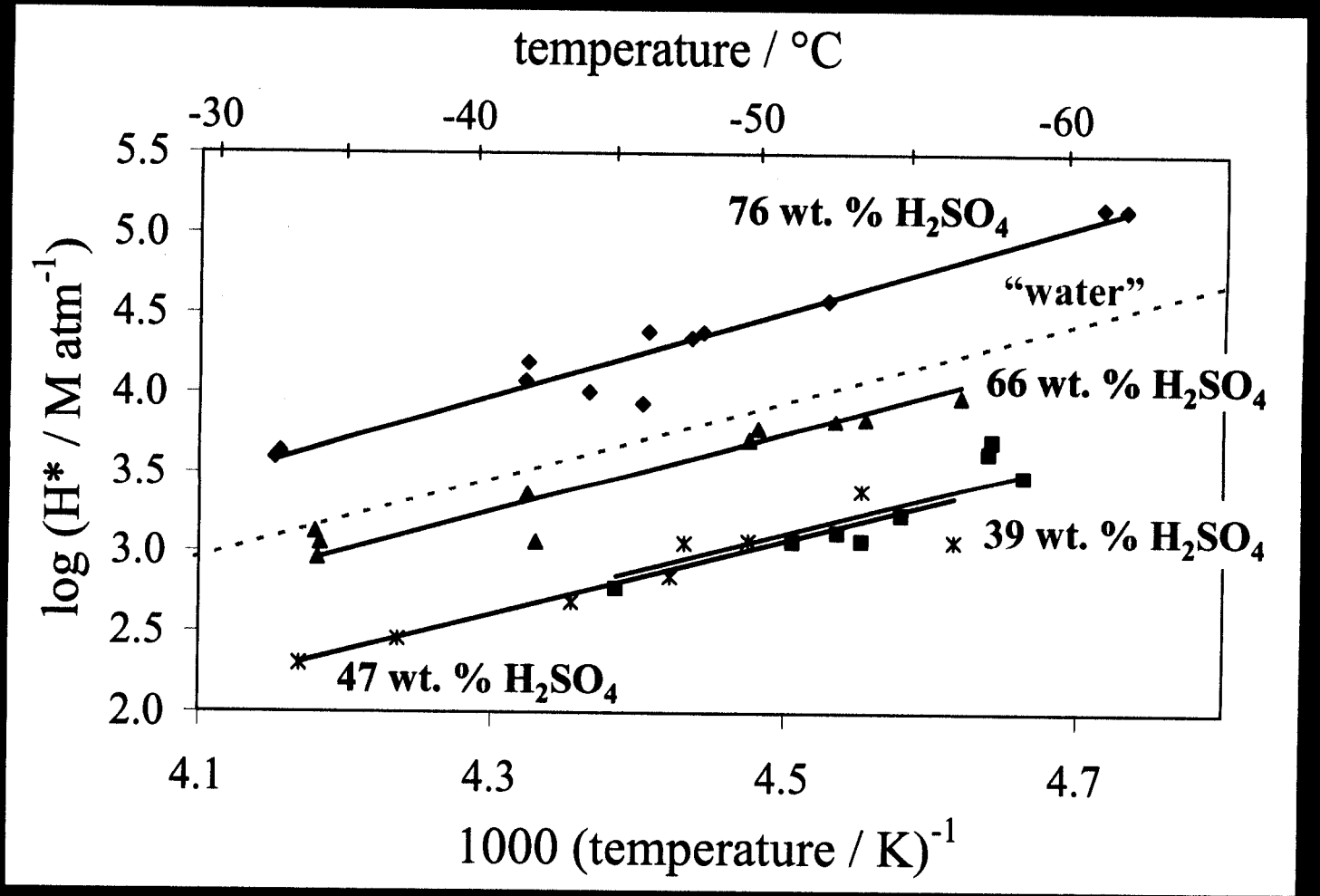

- Sparingly soluble under these conditions
- Solubility is less than in water, except for the most acidic solution

Equilibria in Acidic Media

dissolution

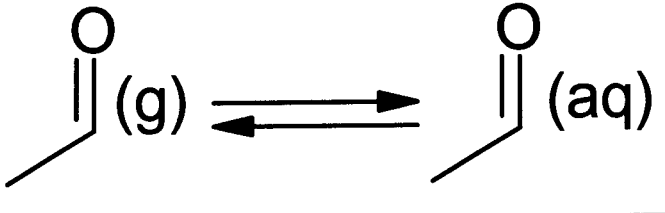

$$H_{mol} = H_{mol}^{H_2O} \cdot \frac{1}{f}$$

activity *f* based on cyclohexane data

hydration

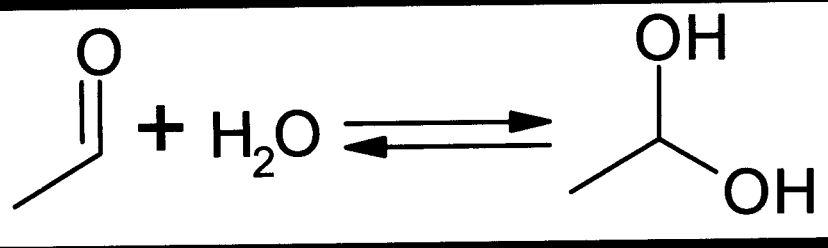

$$H_H = H_{mol} \cdot K_H a_w$$

K_H=1.2/55.6 M ΔH^o=20.5 kJ/mol

protonation

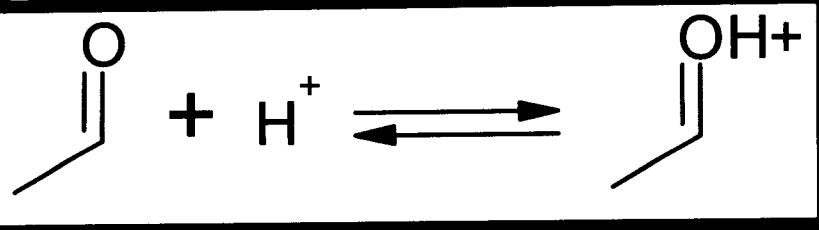

$$H_a = H_{mol} \cdot [\mathrm{H}^+] \cdot 10^{(m^* X + pK_a)}$$

pK_a= -10.2 *m**

*m**=0.35 ΔH^o=0.84 kJ/mol

enolization

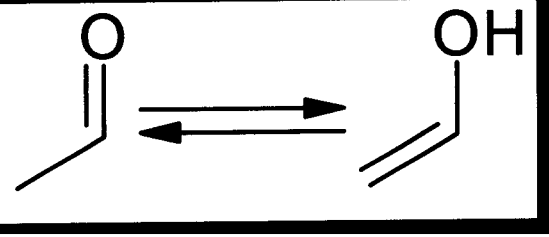

$$H_E = H_{mol} \cdot K_E$$

K_E=5.9×10^{-7}

ΔH^o=38.1 kJ/mol

Solubility of Acetaldehyde in H_2SO_4 at 220 K

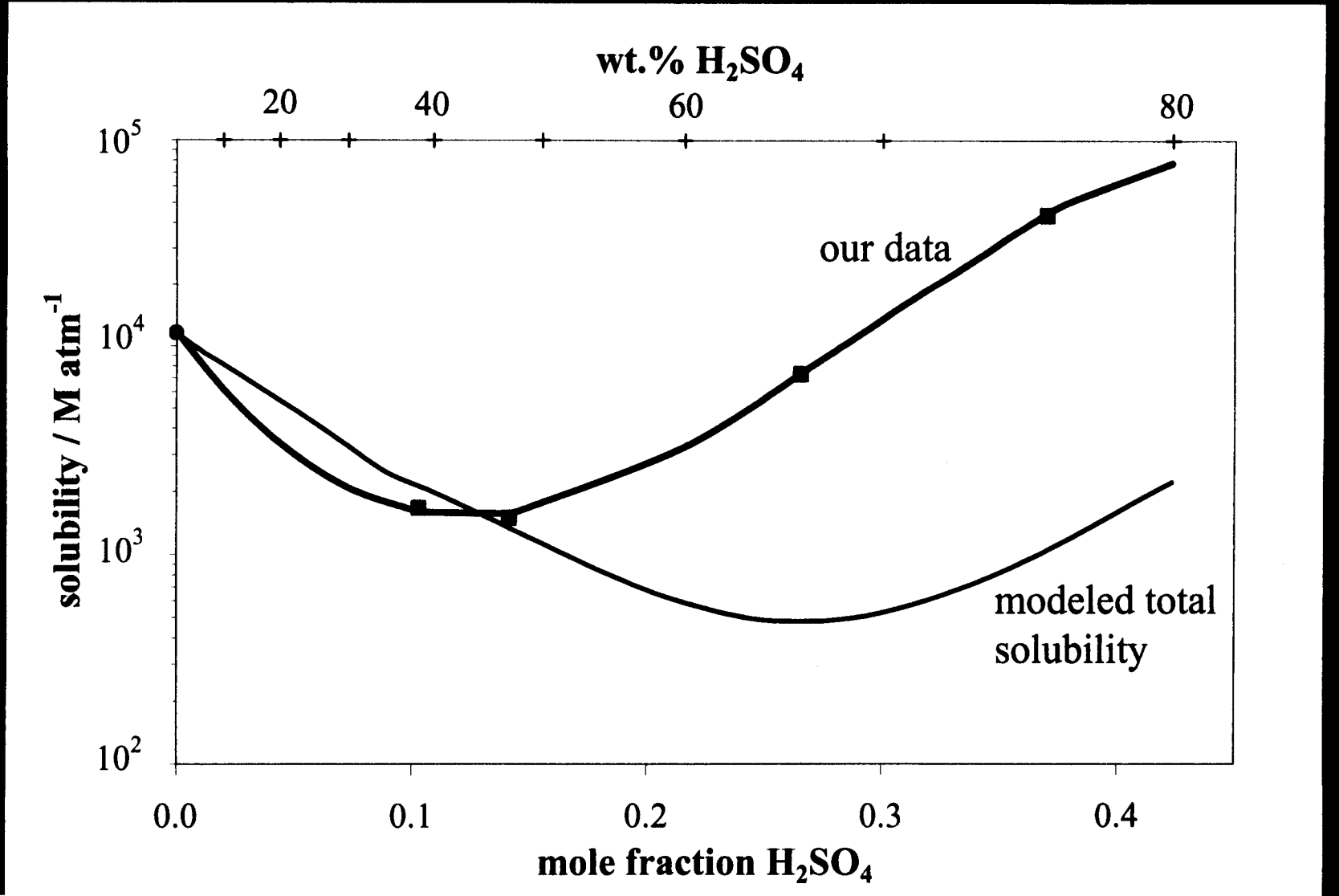

How Speciation Affects Solubility

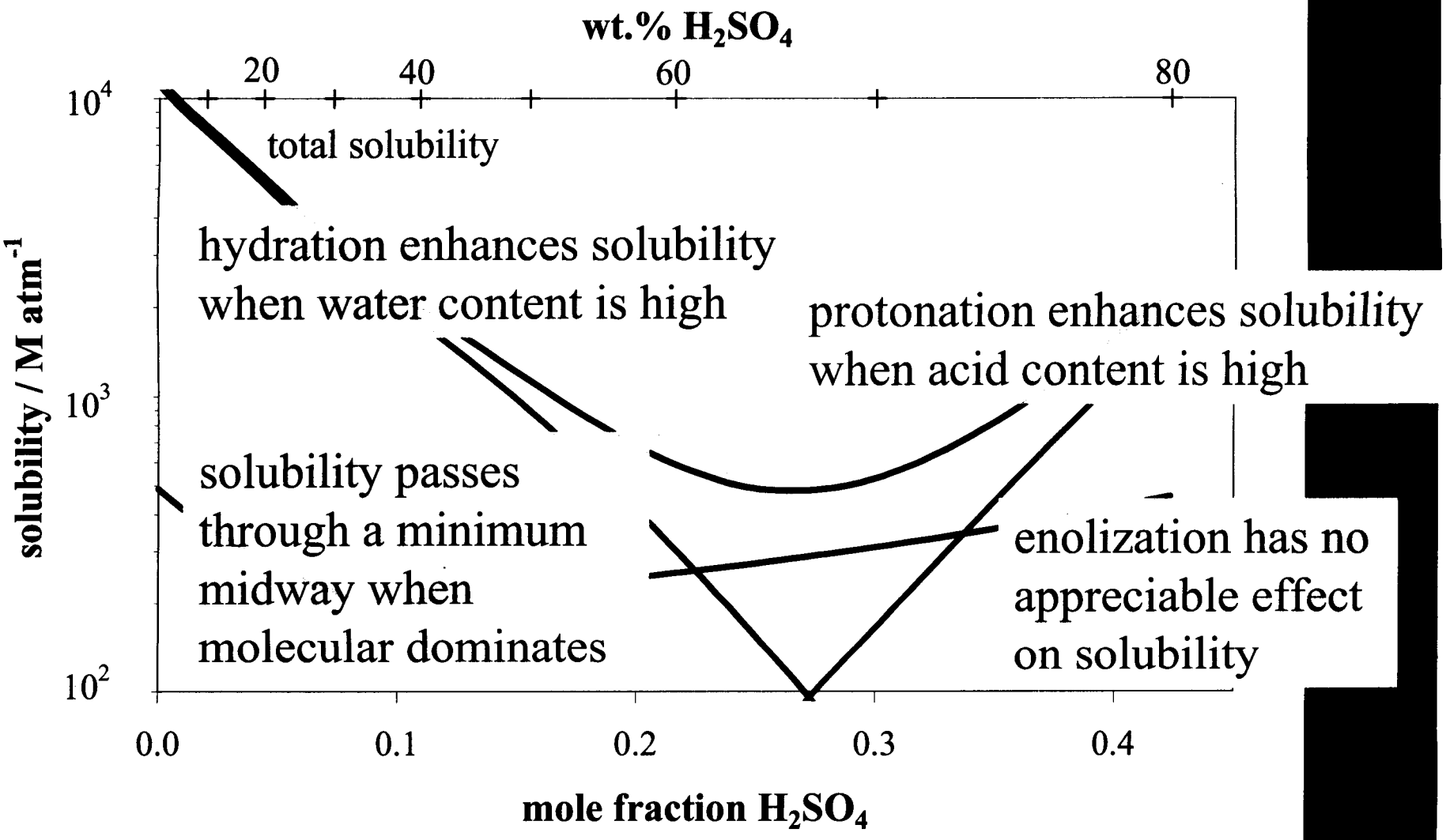

Linear Data: Solubility Only

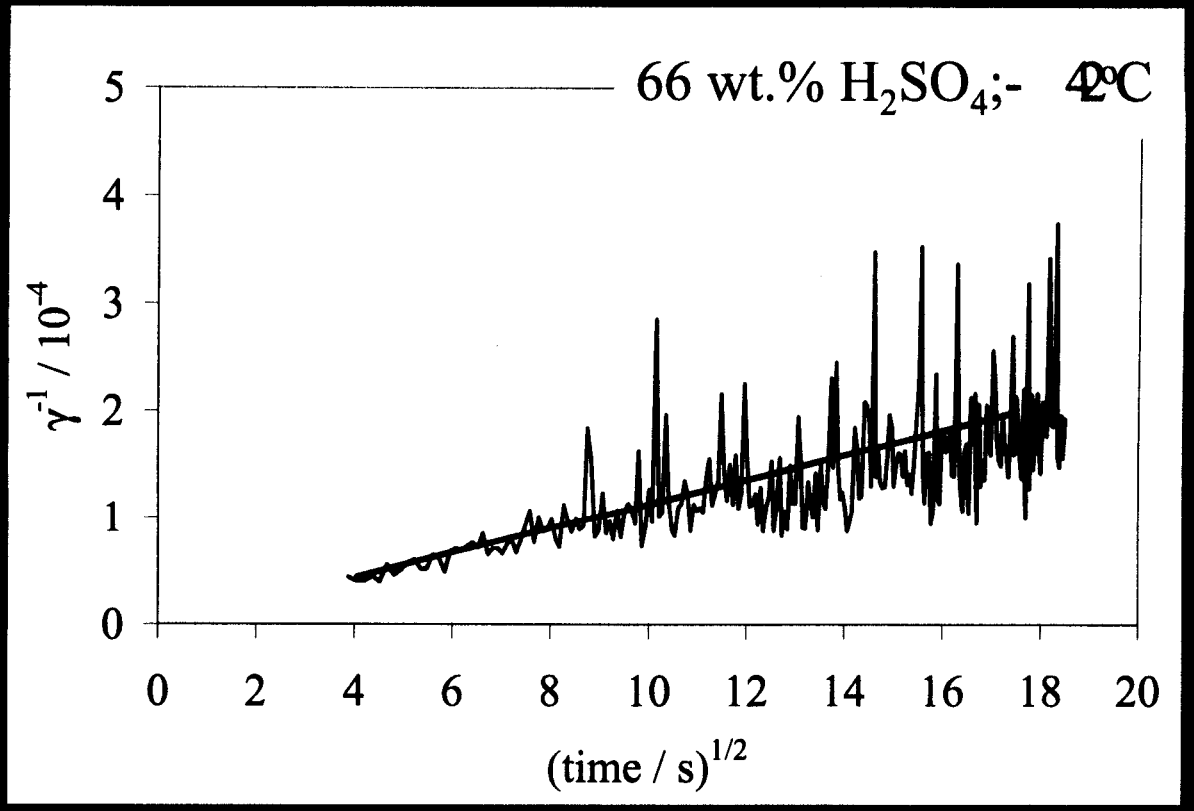

Henry's law solubility

$$\frac{1}{\gamma} = \frac{1}{\Gamma} + \left[\frac{4H^* RT}{\bar{c}} \left(\sqrt{\frac{D_l}{\pi \cdot t}} + \sqrt{D_l k} \right) \right]^{-1}$$

time

first-order rate constant

Acetaldehyde Self-Reaction?

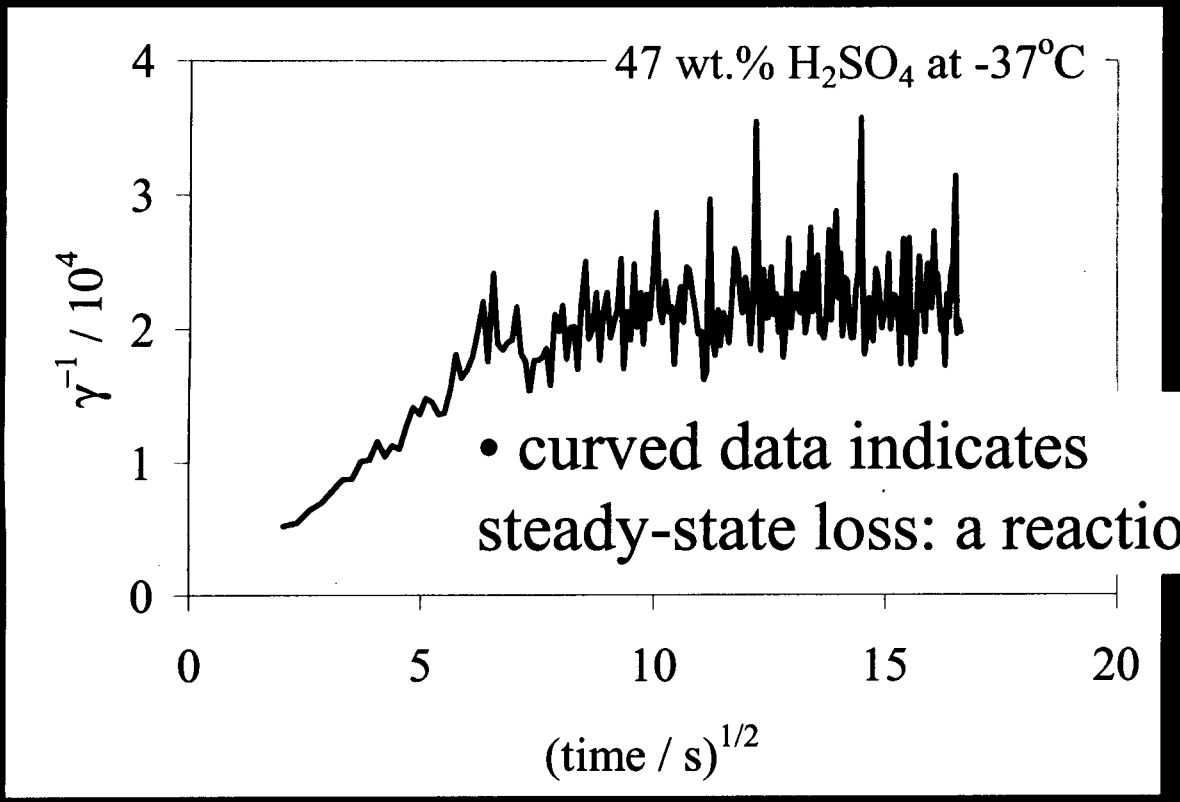

- A likely candidate is aldol condensation-dehydration:

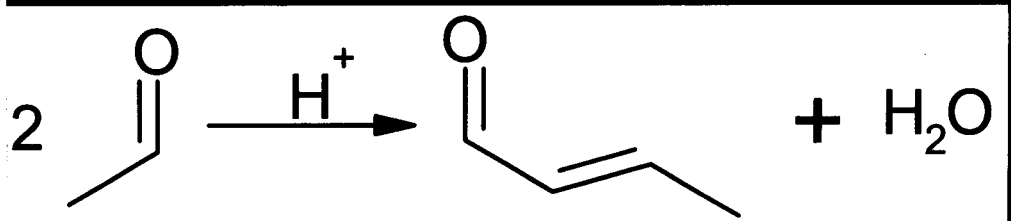

$k_{II} = 2 \times 10^5\ M^{-1}\ s^{-1}$
in 48 wt.% H_2SO_4 at 25°C

Acetaldehyde Self-Reaction?

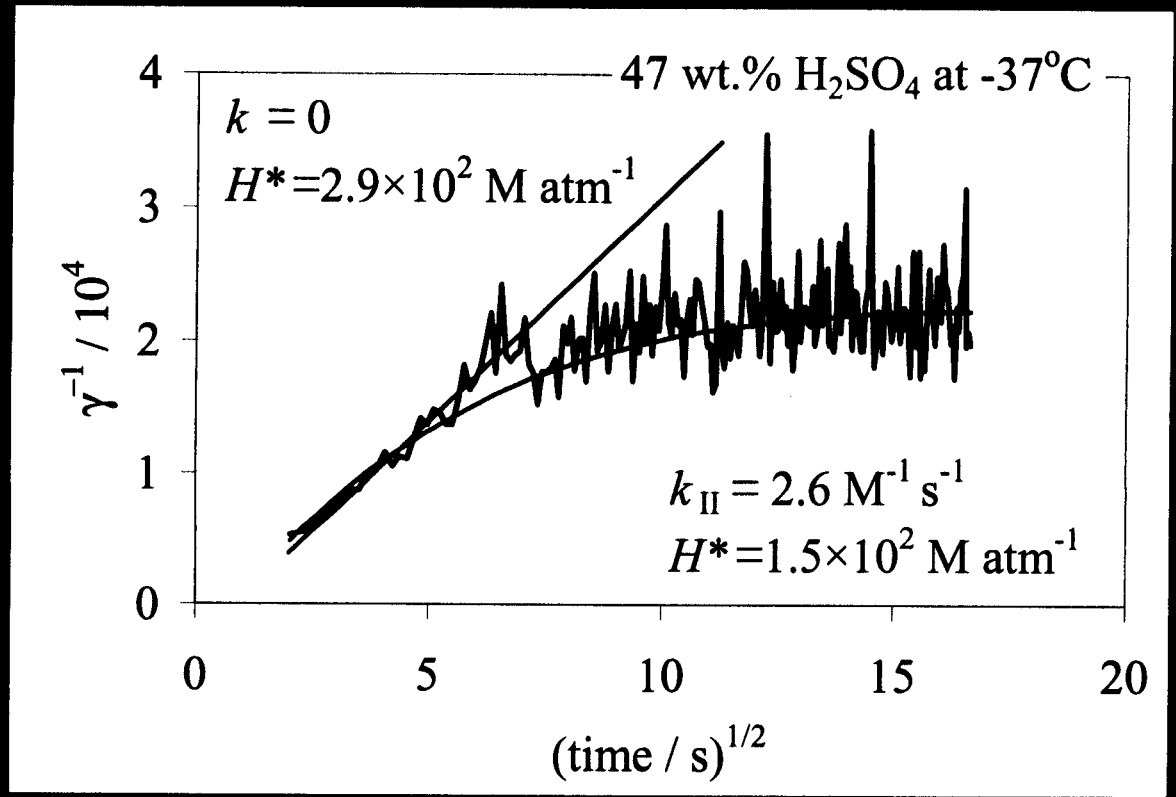

- $k_{II} = 2.6$ M^{-1} s^{-1} (compare to 2×10^5 M^{-1} s^{-1} in 48 wt.% H_2SO_4 at 25°C)
- Second-order rate constant from fit is plausible
- No product was detected in the gas phase

Unexpected Behavior

- Curvature seen in ~1/3 of experiments, mostly in the 47 wt.% acid
- Some of these show a downward taper at long times:

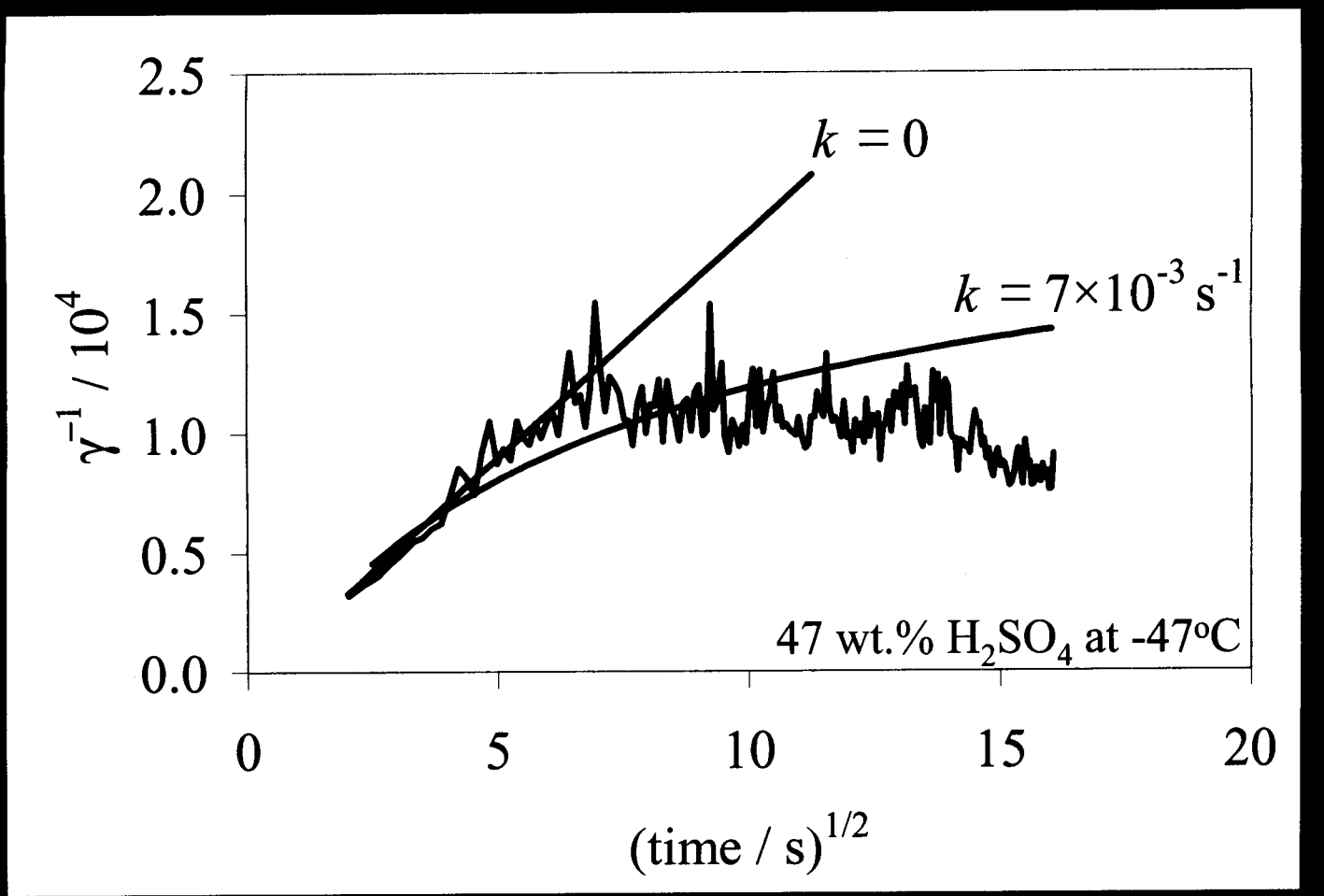

Uptake Enhancement

- Uptake increases with time!
- Cannot be reproduced by solubility + reactivity

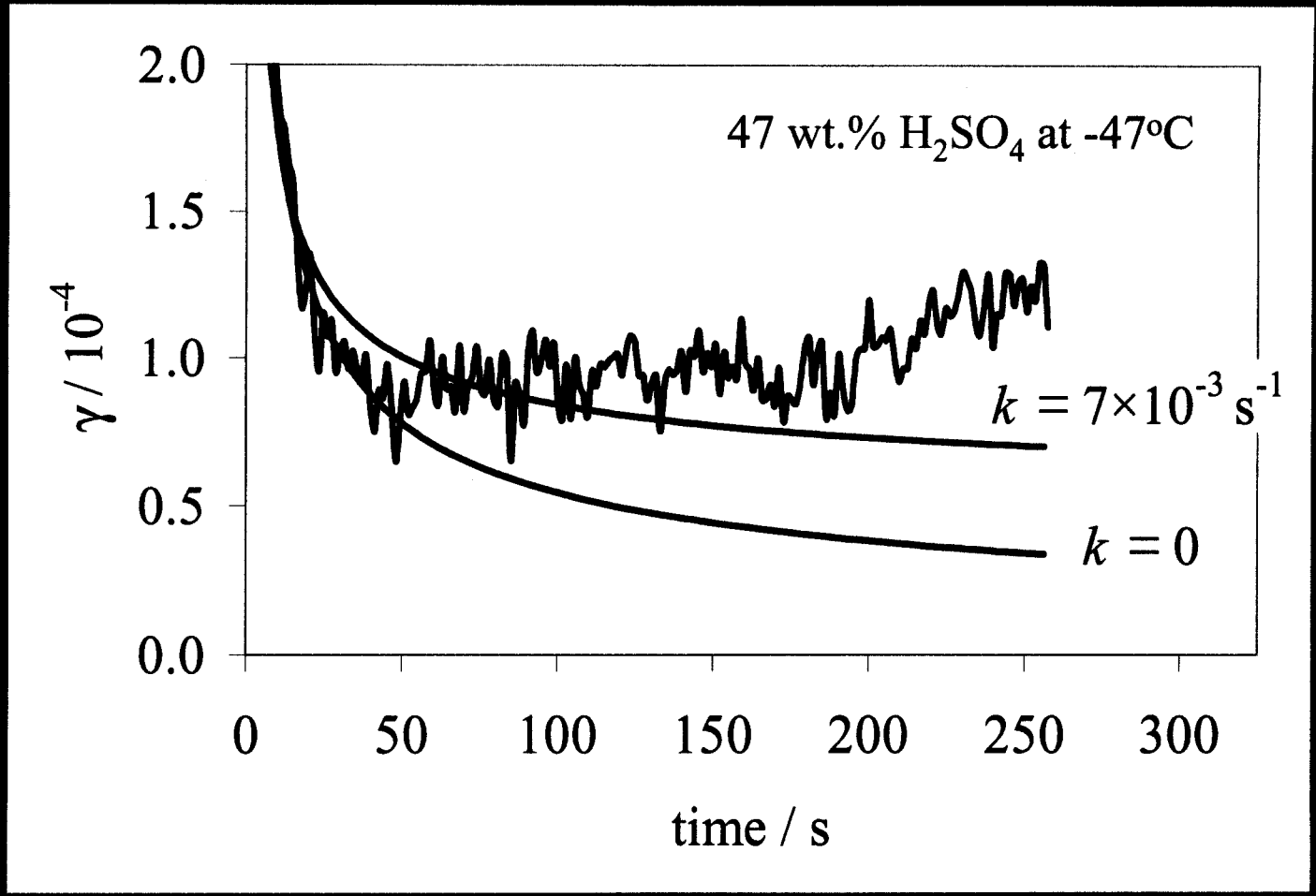

Source of Uptake Enhancement?

- Reaction
  - -continuing loss of gas phase
  - -reasonable estimated rate
  - -no products observed
  - -fit cannot reproduce data

  ➞ IR spectroscopy of condensed phase should confirm or rule out
- Surface effect: reaction or structural change

  ➞ Needs further experimental investigation, such as longer exposure times
- Deviations from Henry's law (solubility is increasing)
  - -concentrations reasonable
  - -direction is correct for system
  - -deviation seems large
- Other?

Conclusions

- Acetaldehyde is sparingly soluble in sulfuric acid solutions under upper tropospheric conditions

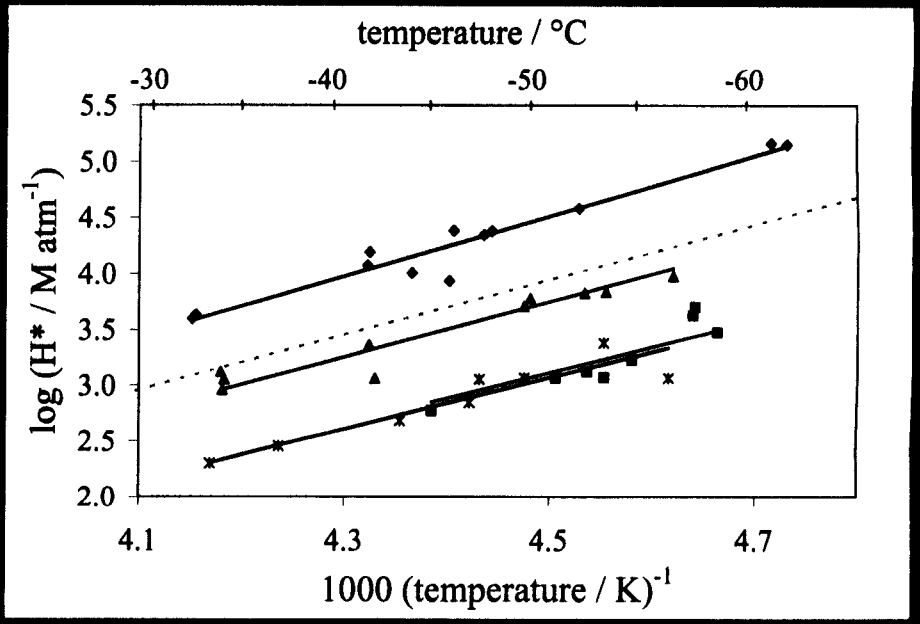

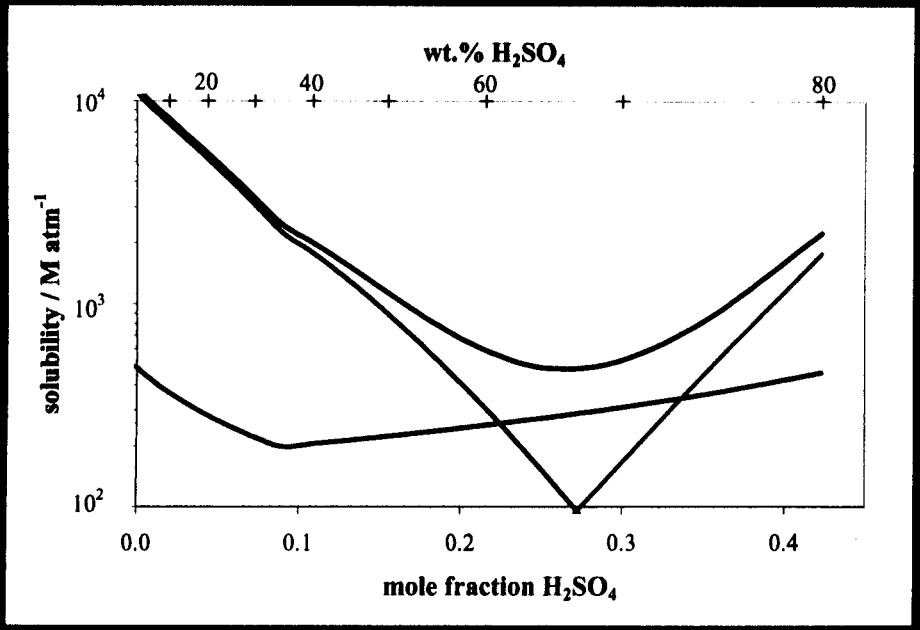

- Solubility is enhanced by the hydration channel at low acid content, and by the protonation channel at high acid content

More Conclusions

- Uptake of acetaldehyde by sulfuric acid is enhanced at long times under some conditions

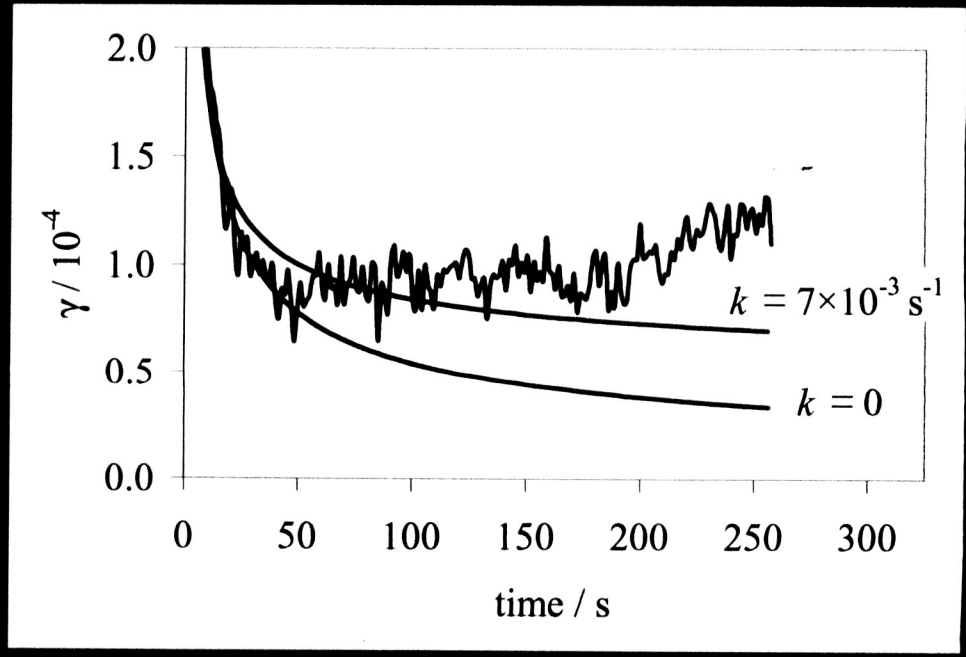

- Possible sources of this behavior have significant atmospheric implications:

Reaction ⟹ condensed-phase accumulation of organic material of low solubility and mixing ratio

Henry's law deviation ⟹ the more organic material present, the more uptake occurs

Acknowledgements

Laura T. Iraci

Samantha F. M. Ashbourn

Daniel Knopf & Bei Ping Luo
The National Research Council
The Dreyfus Foundation
NASA Upper Atmosphere Research Program
NASA New Investigators Program

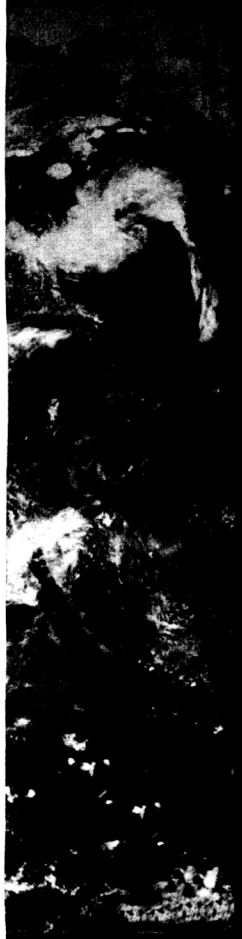

AGU
Fall
Meeting
2003

Deviation from Henry's Law

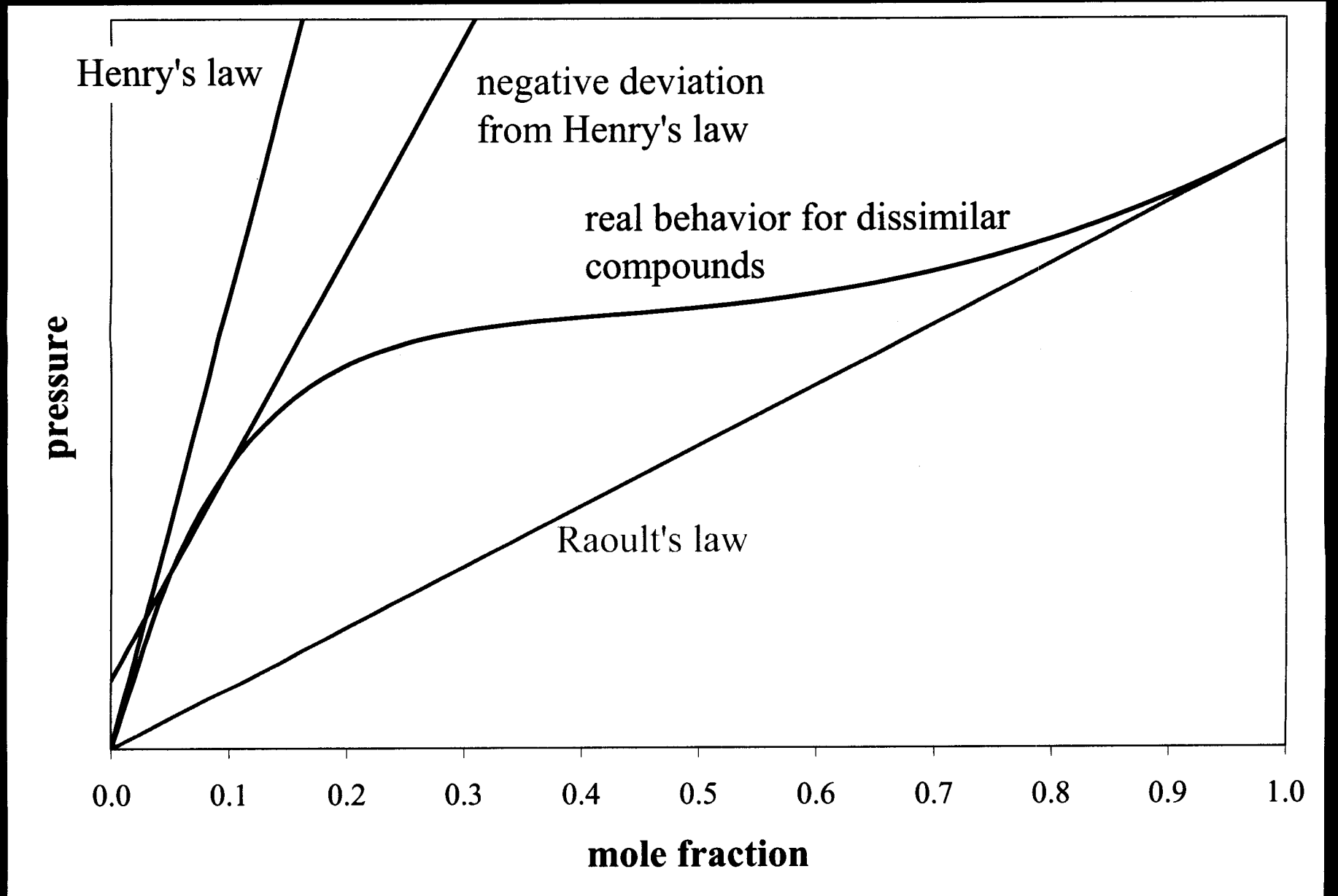

Deviation from Henry's Law

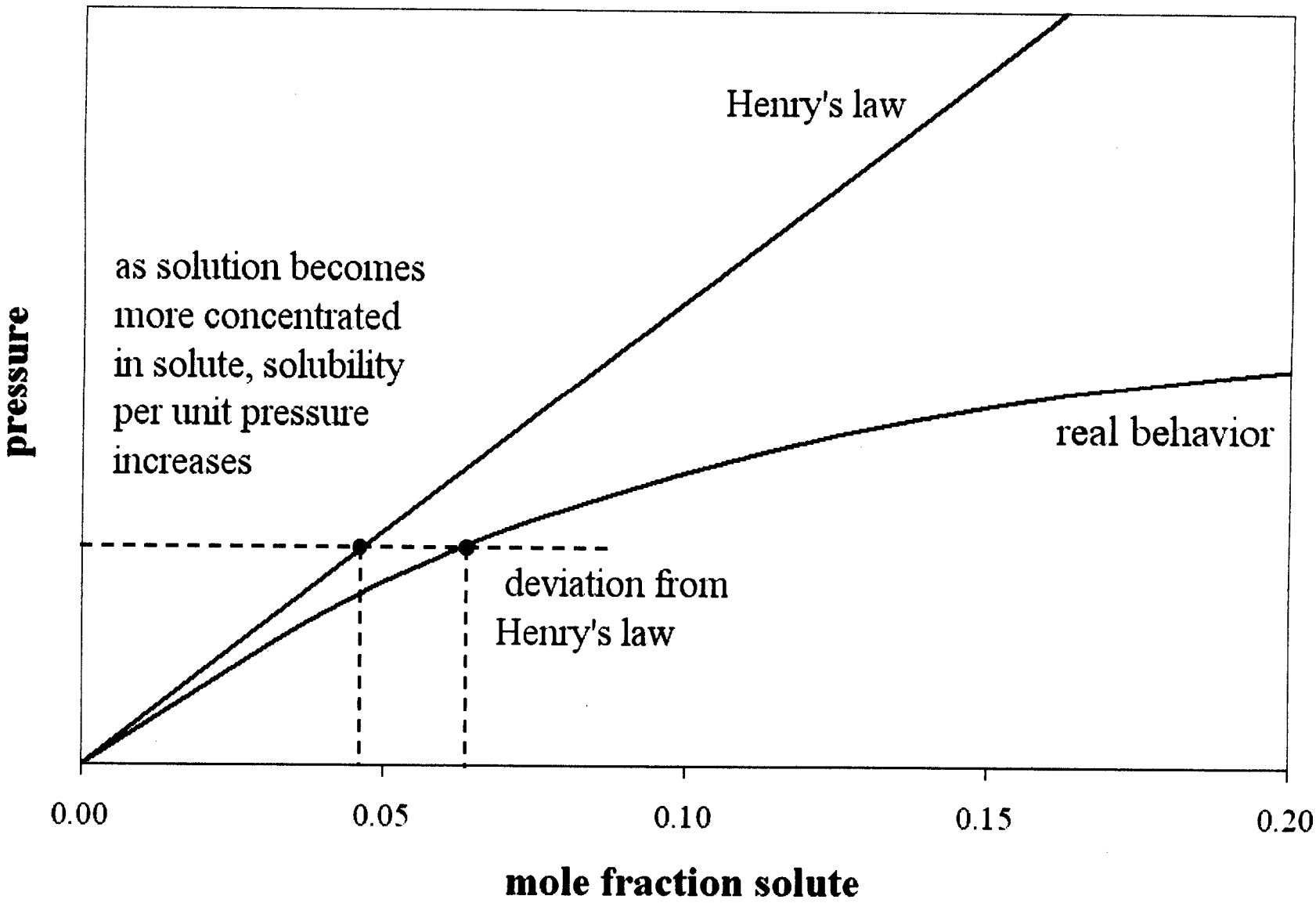

Varying Activity Versus Sestchenow Dependence

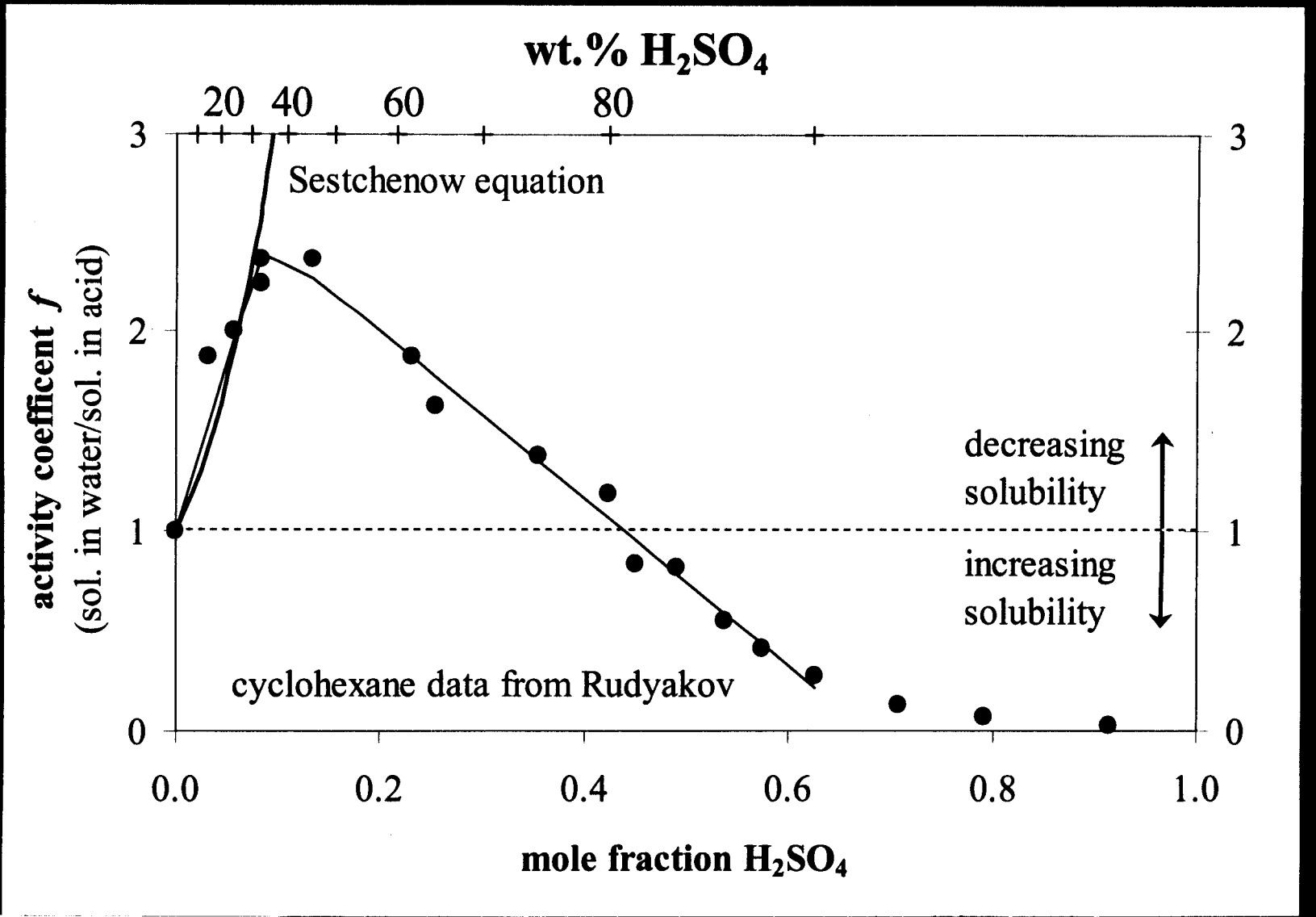

"Curved" Data

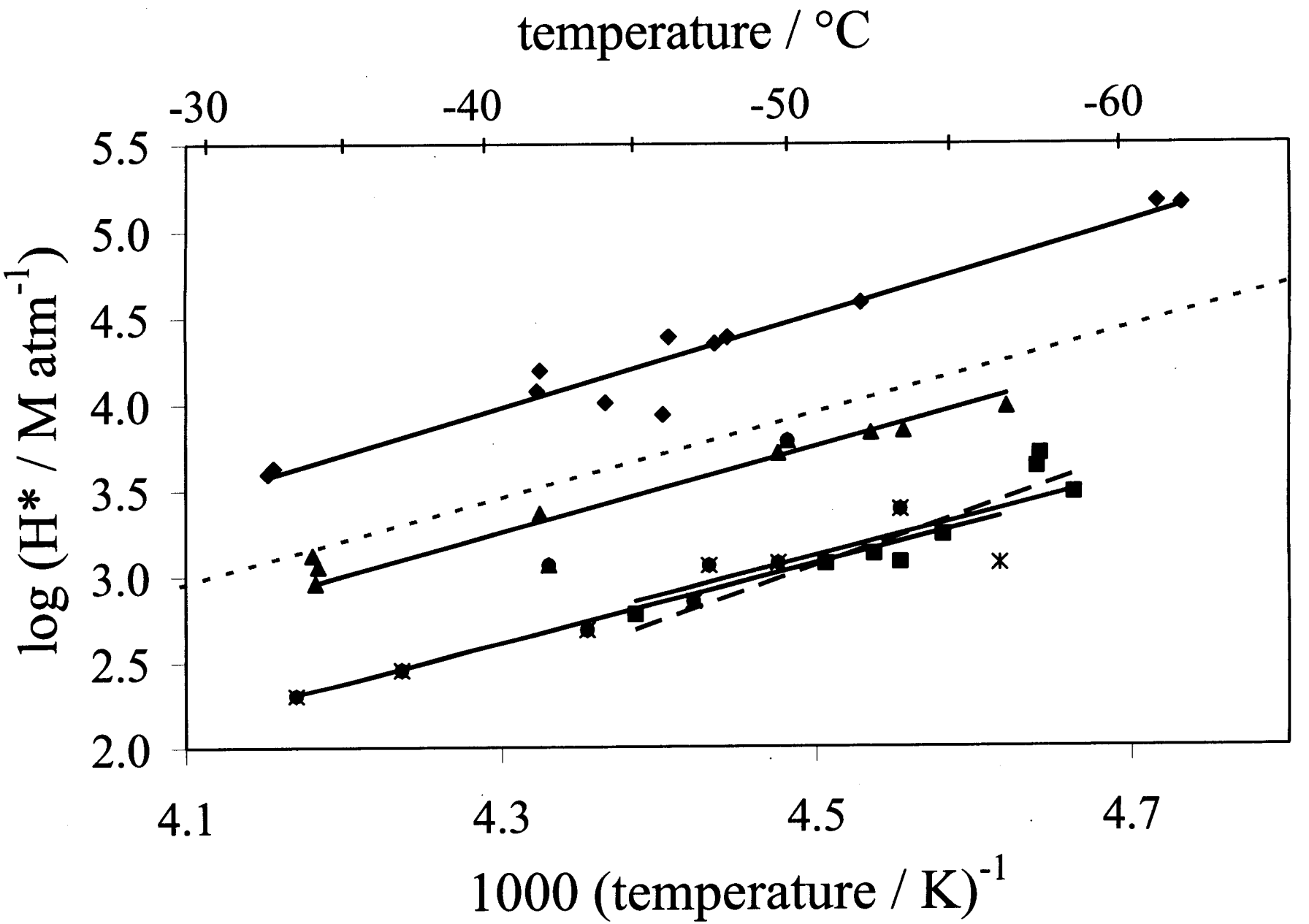
temperature / °C
-30
-40
-50
-60
5.5
5.0
4.5
4.0
3.5
3.0
2.5
2.0
log (H* / M atm^{-1})
4.1
4.3
4.5
4.7
1000 (temperature / K)$^{-1}$

Molecular Solubility Versus Sestchenow Dependence

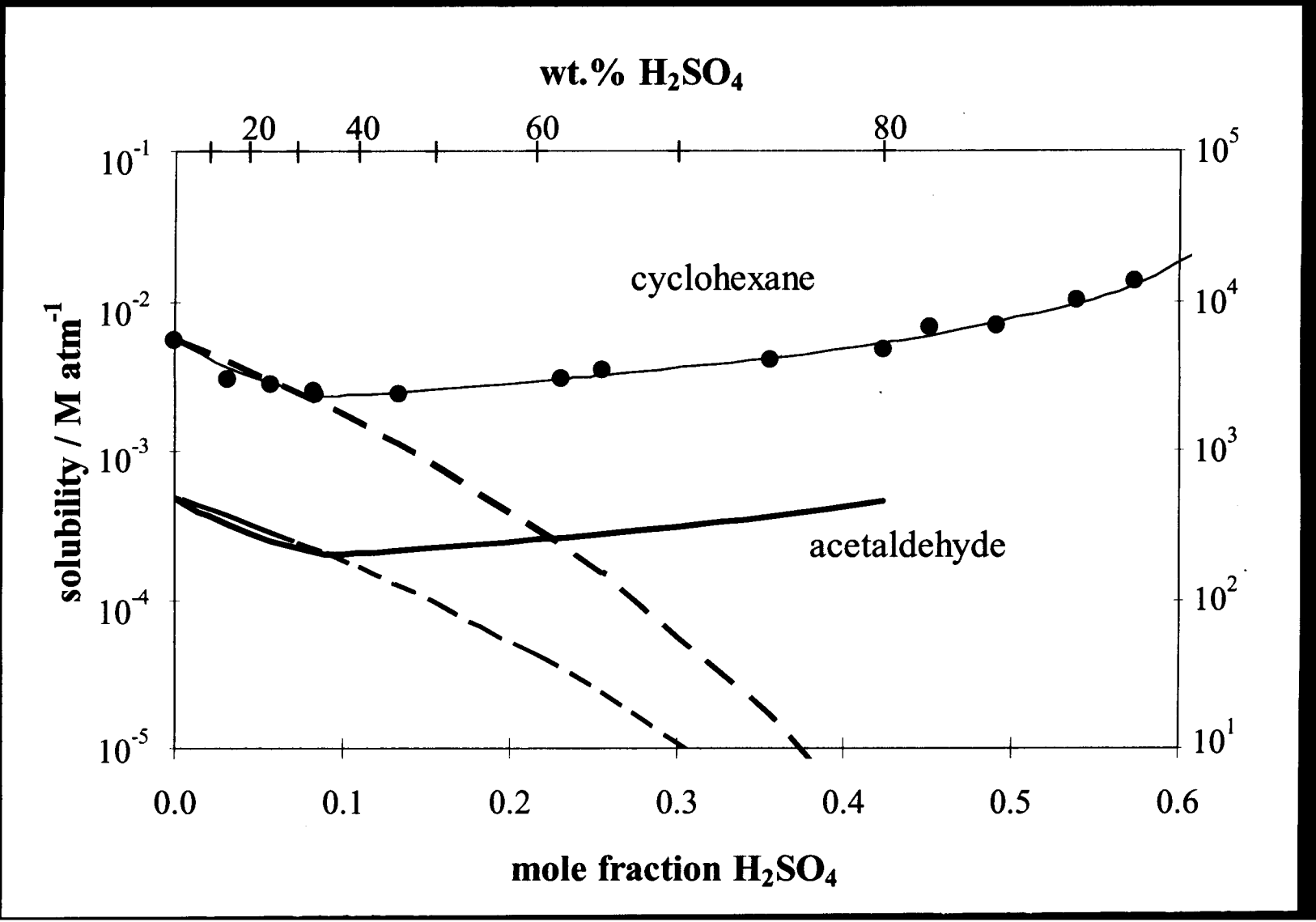

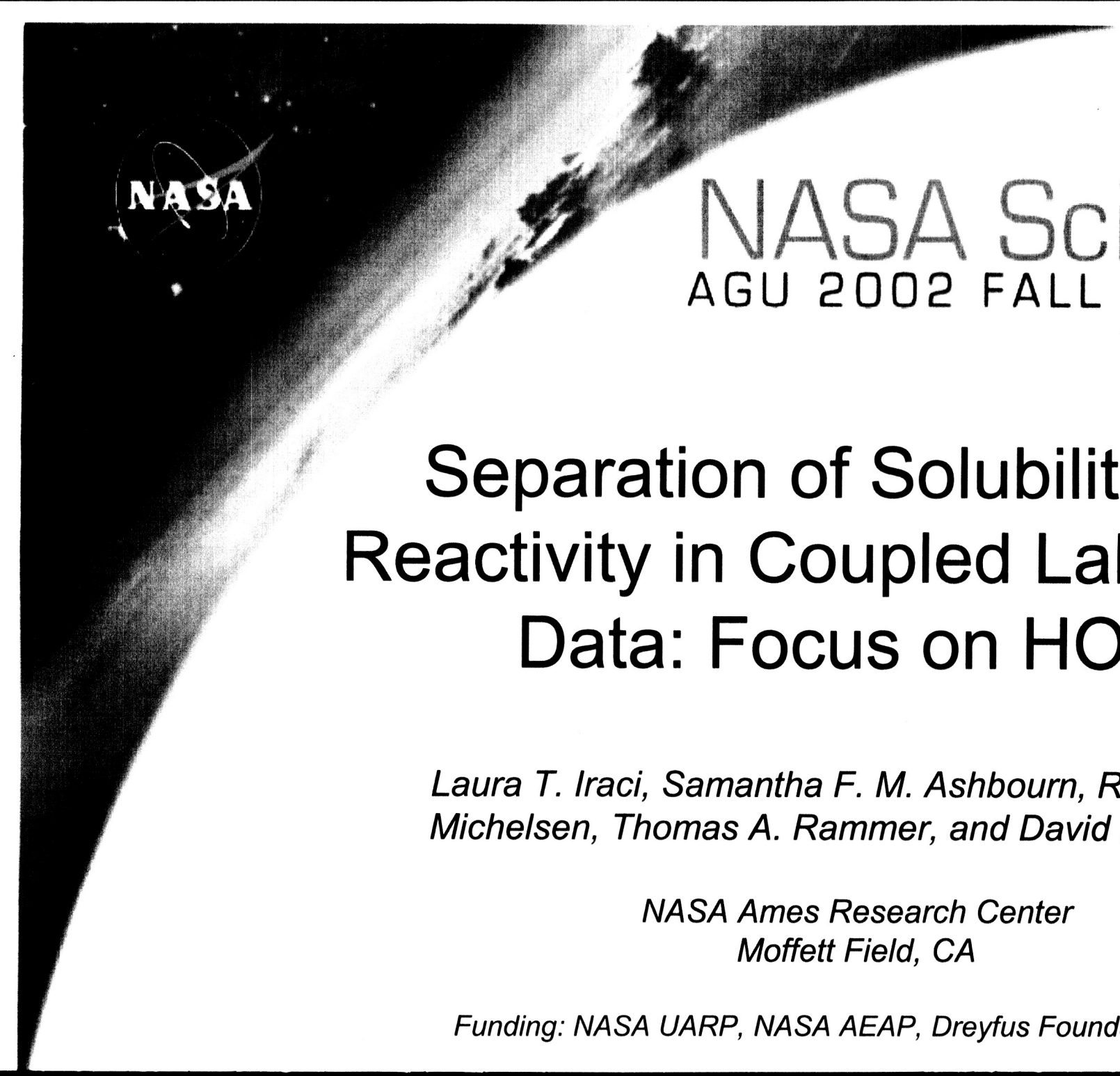

NASA Science

AGU 2002 FALL MEETING

Separation of Solubility and Reactivity in Coupled Laboratory Data: Focus on HOBr

Laura T. Iraci, Samantha F. M. Ashbourn, Rebecca R. Michelsen, Thomas A. Rammer, and David M. Golden

NASA Ames Research Center
Moffett Field, CA

Funding: NASA UARP, NASA AEAP, Dreyfus Foundation, NRC

Uptake of Gas into Planar Liquid

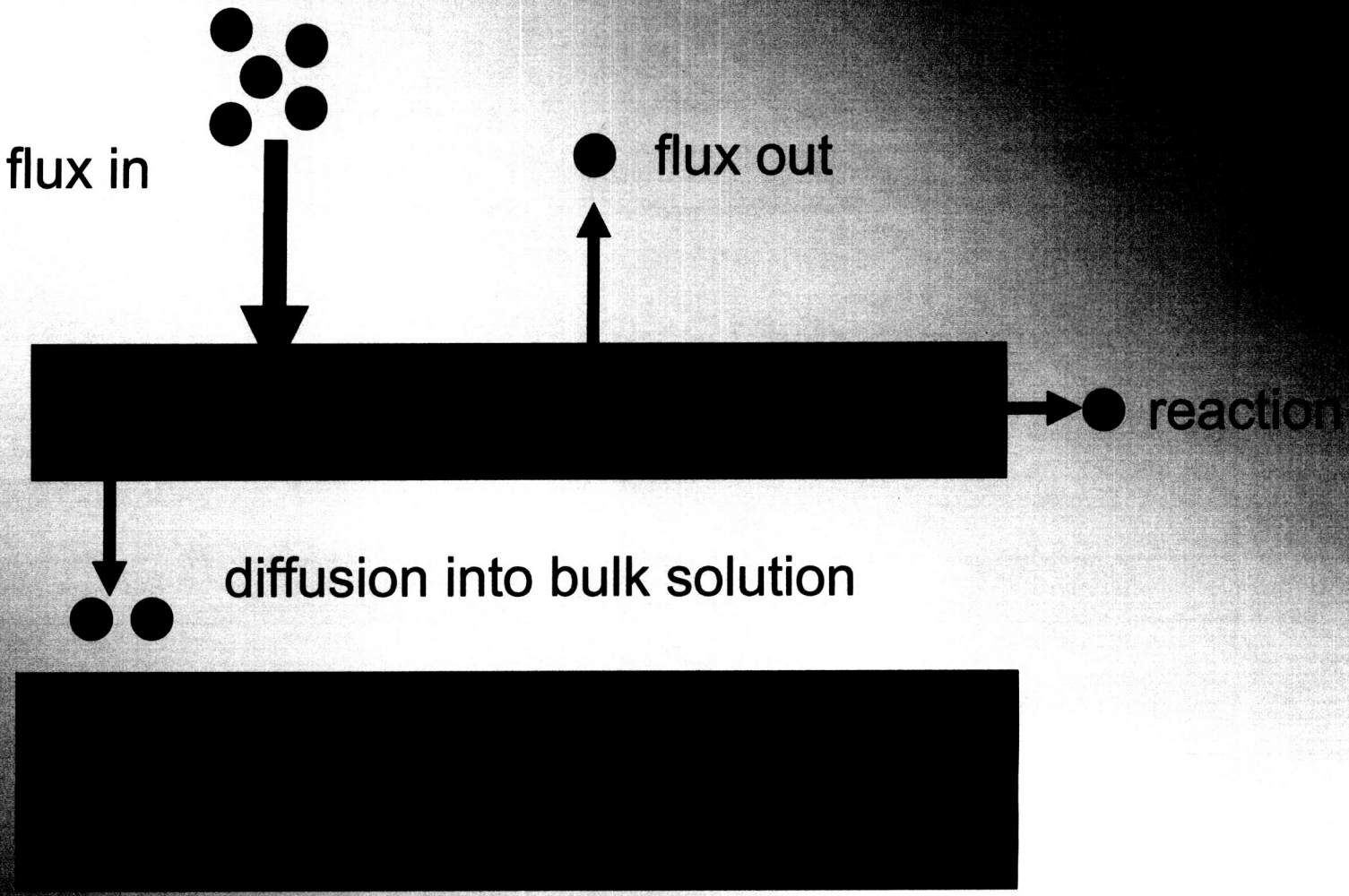

...rvable quantity: NET flux of gas into liquid

...determine γ = probability of uptake

Examples of Extremes

- Solubility only

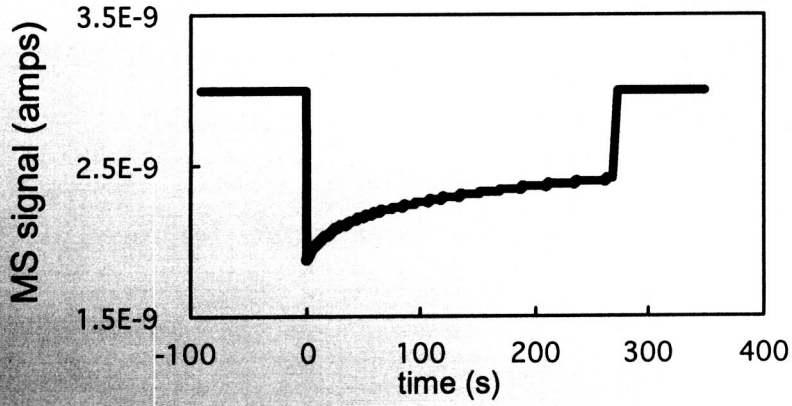

$$\frac{1}{\gamma(t)} = \beta + \left(\frac{\bar{c}\sqrt{\pi}}{4RTH^{*}\sqrt{D}}\right)\cdot\sqrt{t}$$

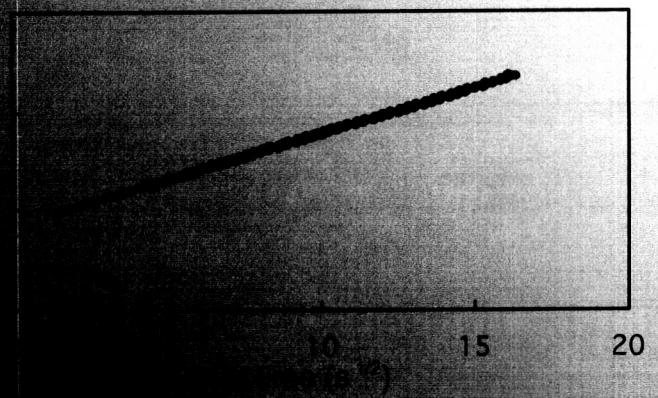

- Reaction

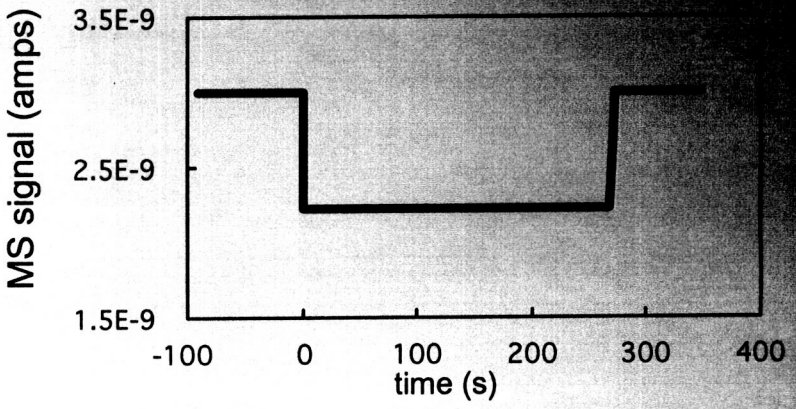

$$\frac{1}{\gamma(t)} = \beta + \left(\frac{\bar{c}}{4RTH^{*}\sqrt{D}}\right)\cdot\left(\frac{1}{\sqrt{k}}\right)$$

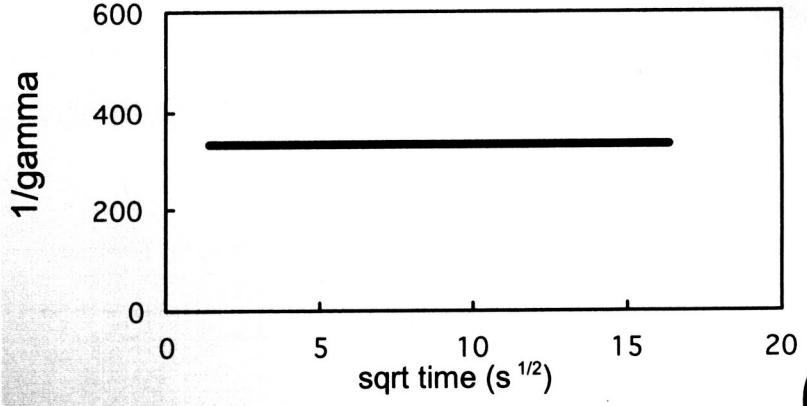

NASA

Mathematical Treatment of Uptake

- flux in $= \alpha \frac{\bar{c} n_g}{4}$ □□□□□□ $\alpha \frac{\bar{c} n_l(t)}{4RTH^*}$
- diffusion $n_l(t) = J\sqrt{\frac{t\pi}{D_l}}$
- reaction $rate = \frac{-d[A]}{dt} = k_{II}[A][B] \Rightarrow k[A]$
- overall equation:

$$\frac{1}{\gamma(t)} = \left(\frac{1}{\Gamma_g} + \frac{1}{\alpha}\right) + \left(\frac{\bar{c}\sqrt{\pi}}{4RTH^*\sqrt{D}}\right) \cdot \left(\frac{1}{t^{-1/2} + \sqrt{\pi k}}\right)$$

- generally study systems where either solubility or reaction dominates

NASA

Examples of Extremes

- Solubility only

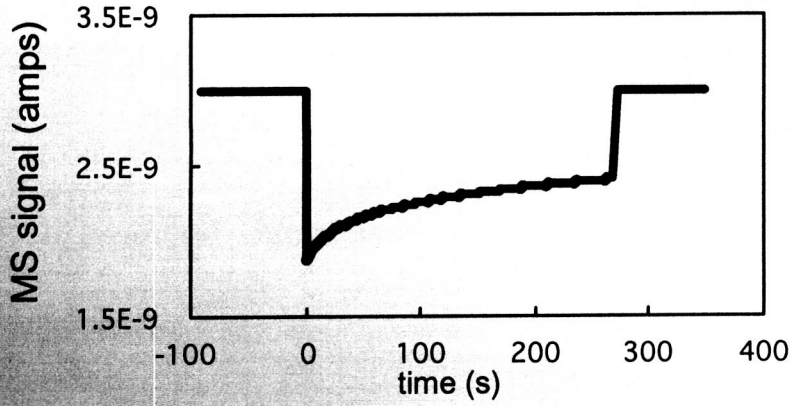

$$\frac{1}{\gamma(t)} = \beta + \left(\frac{\bar{c}\sqrt{\pi}}{4RTH^{*}\sqrt{D}}\right)\cdot\sqrt{t}$$

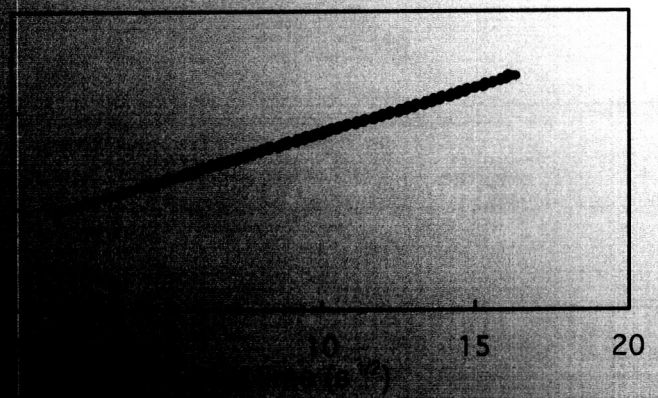

- Reaction

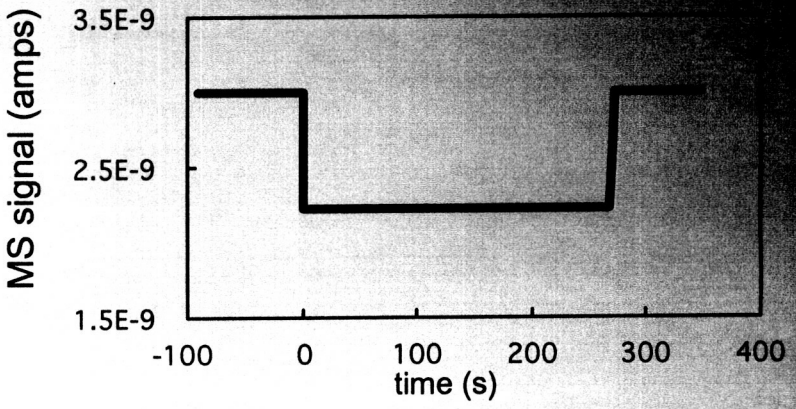

$$\frac{1}{\gamma(t)} = \beta + \left(\frac{\bar{c}}{4RTH^{*}\sqrt{D}}\right)\cdot\left(\frac{1}{\sqrt{k}}\right)$$

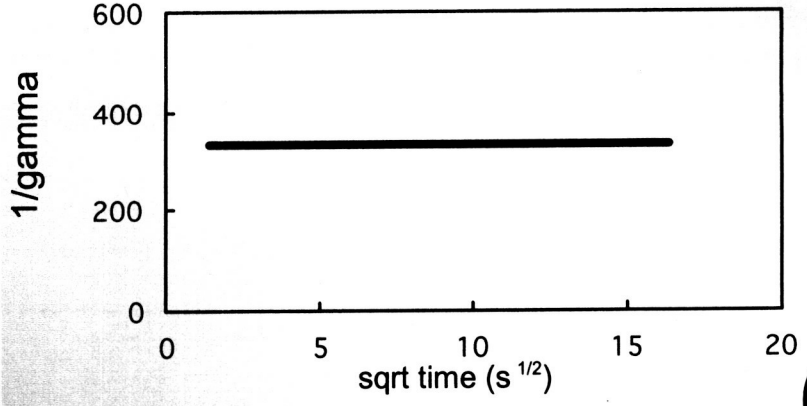

NASA

When Solubility and Reaction Compete

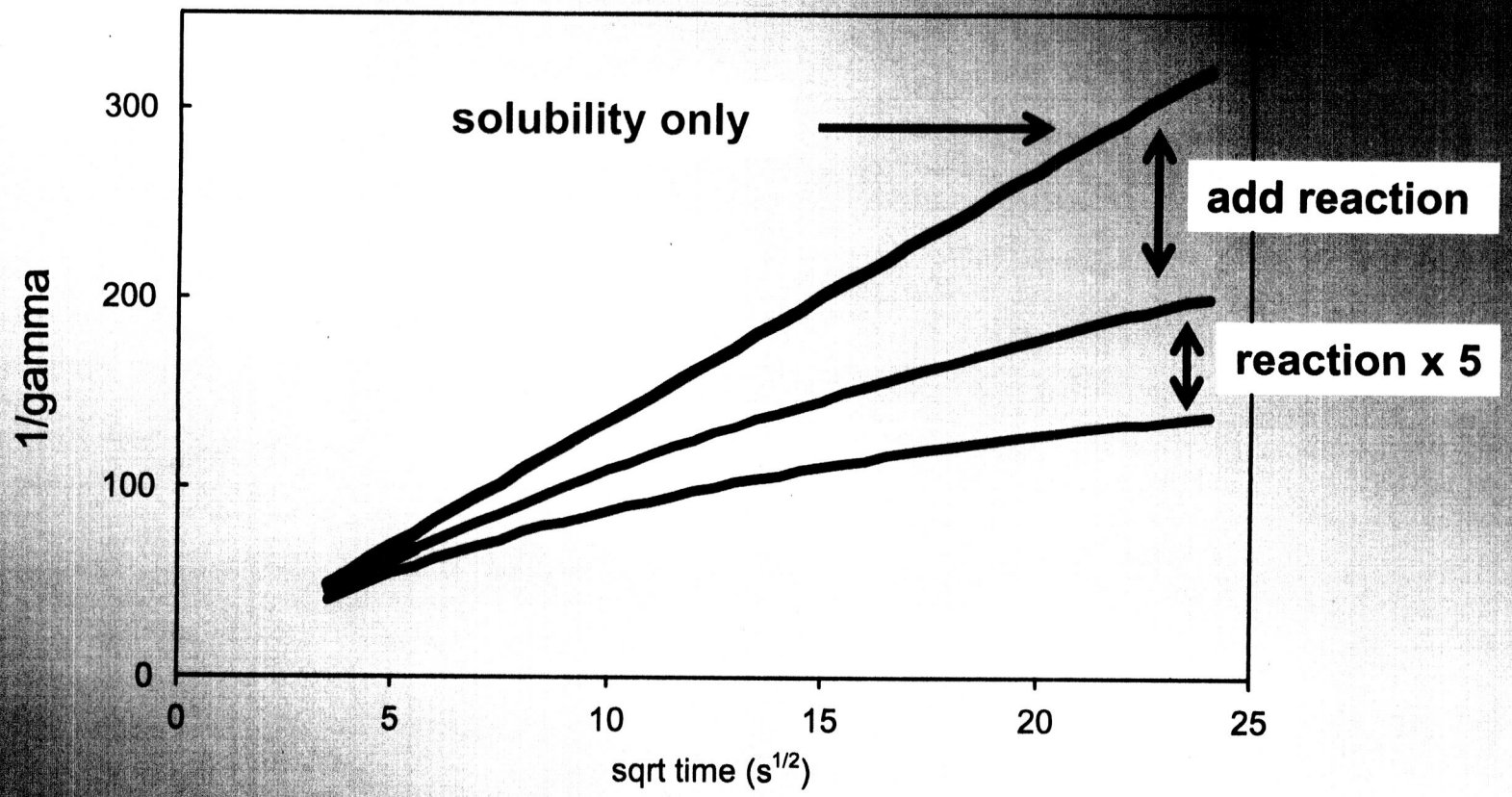

- not linear when solubility and reaction both important
- fit to three variables, H^*, k, and intercept

HOBr Chemistry

- produced in LS by BrO + HO_2 and by $BrONO_2$ hydrolysis
- chlorine activation without polar stratospheric clouds:

  HOBr (aq) + HCl (aq) → BrCl (g)

- *How will HOBr chemistry affect the recovery of ozone in the absence of PSCs?*
- Solution phase chemistry of HOBr is not well defined, especially under cold, acidic conditions. Possible reactions include:

  $HOBr + HBr \leftrightarrows Br_2 + H_2O \quad K_{eq} = 1.6 \times 10^8\ M^{-2}$ at 25°C

  $HOBr + HOBr \leftrightarrows Br_2O + H_2O$

  $HOBr + H^+ \leftrightarrows H_2OBr^+$

  These reactions are favored at low pH, consistent with our observation of reaction in more acidic solutions

HOBr Uptake: 45 wt% H_2SO_4, 231 K

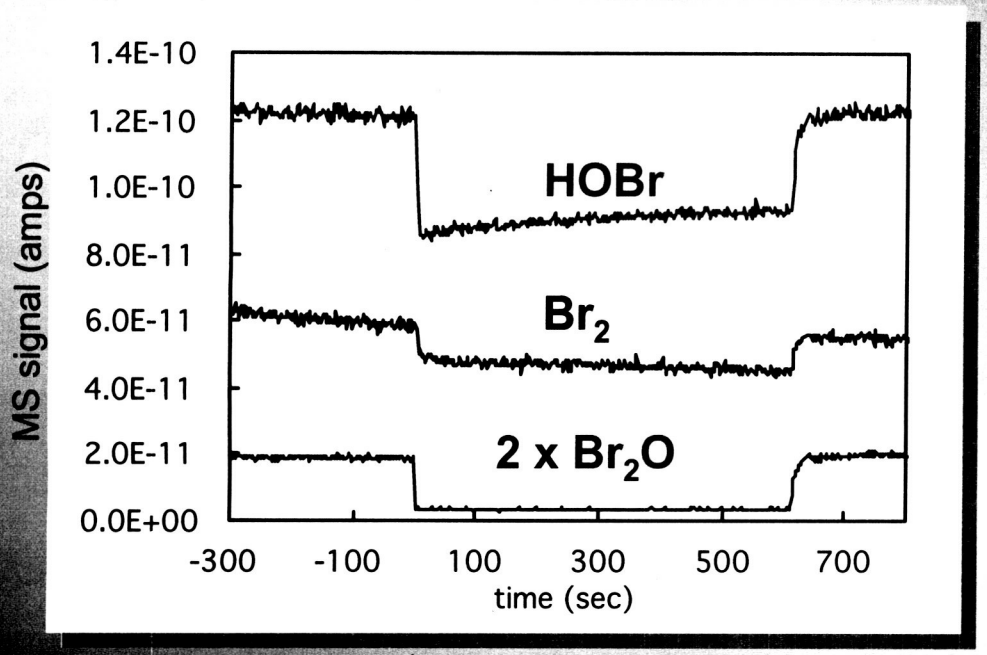

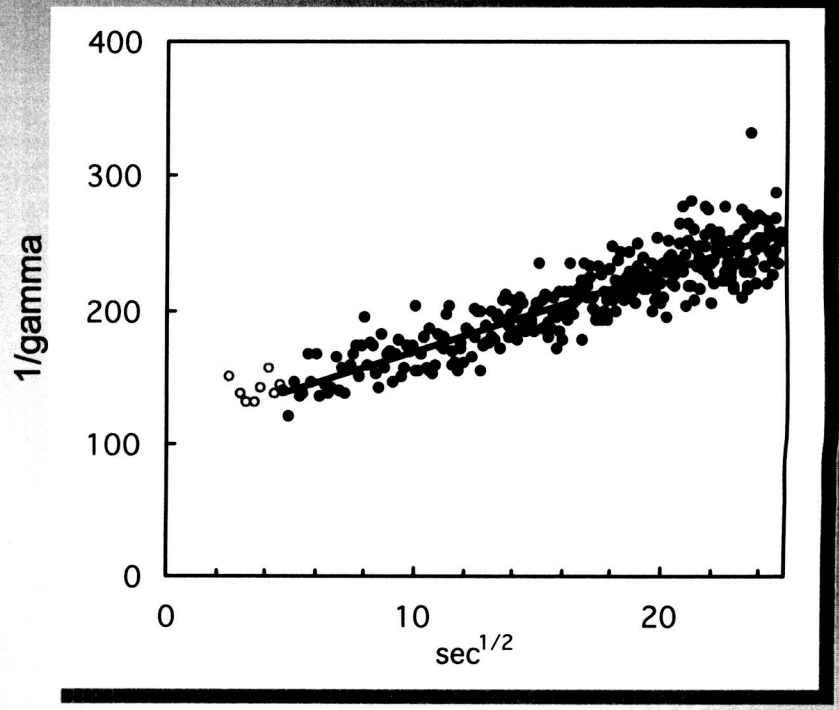

- HOBr taken up by 45 wt% sulfuric acid
- [illegible] indicates only solubility contributes to uptake
- [illegible] and HBr (not shown) impurities are also soluble

NASA

HOBr Uptake: 70 wt% H_2SO_4, 213 K

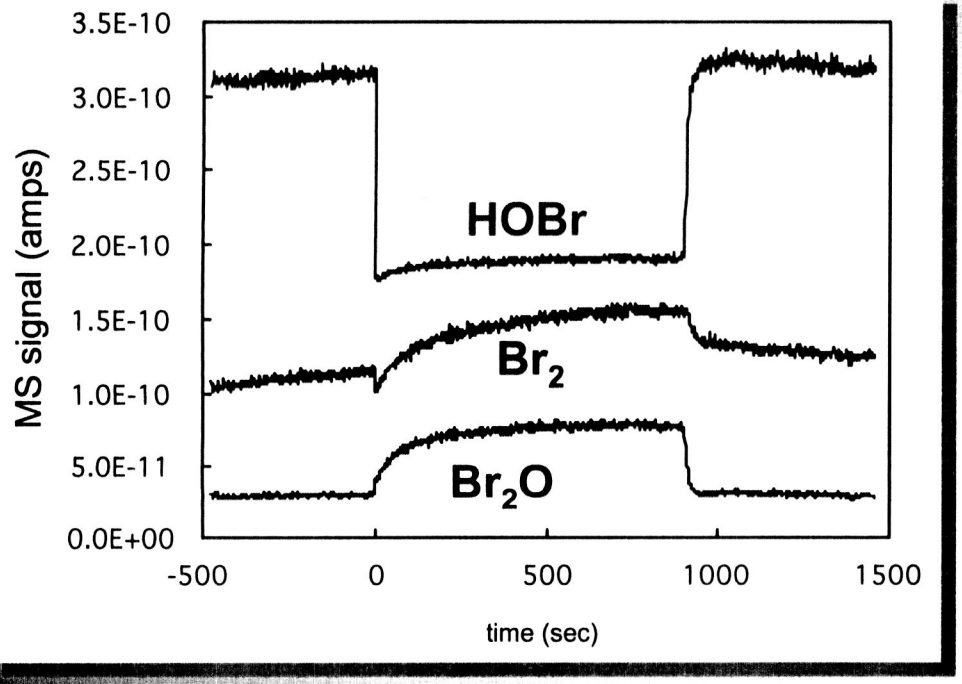

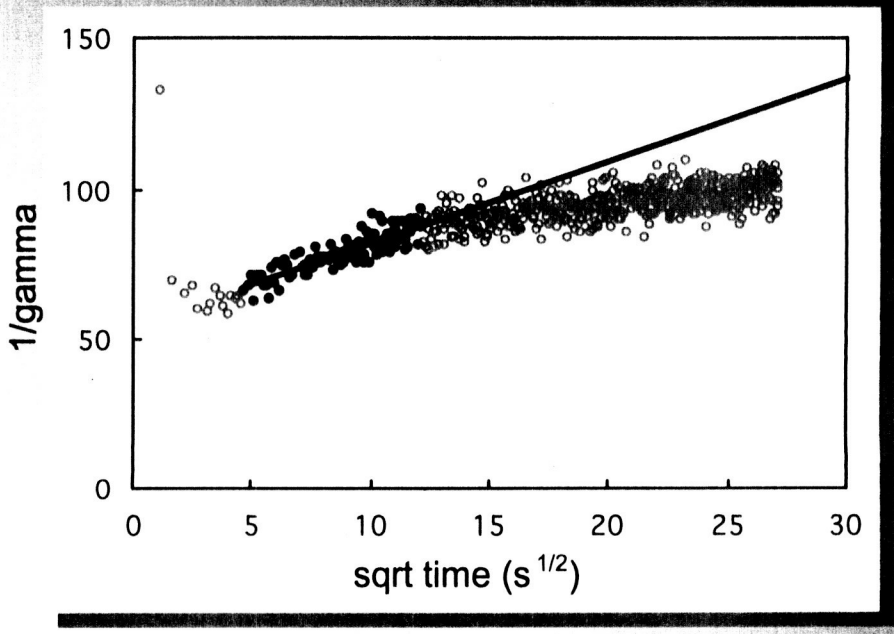

- **HOBr** taken up by 70 wt% sulfuric acid, but not only solubility
- **Br_2** initially taken up, then produced
- **Br_2O** produced
- **Br** taken up throughout (not shown)
- ***HOBr is both soluble and reactive in cold, concentrated acid***

HOBr and Br2 shown offset for clarity

Multi-Parameter Fit to Data

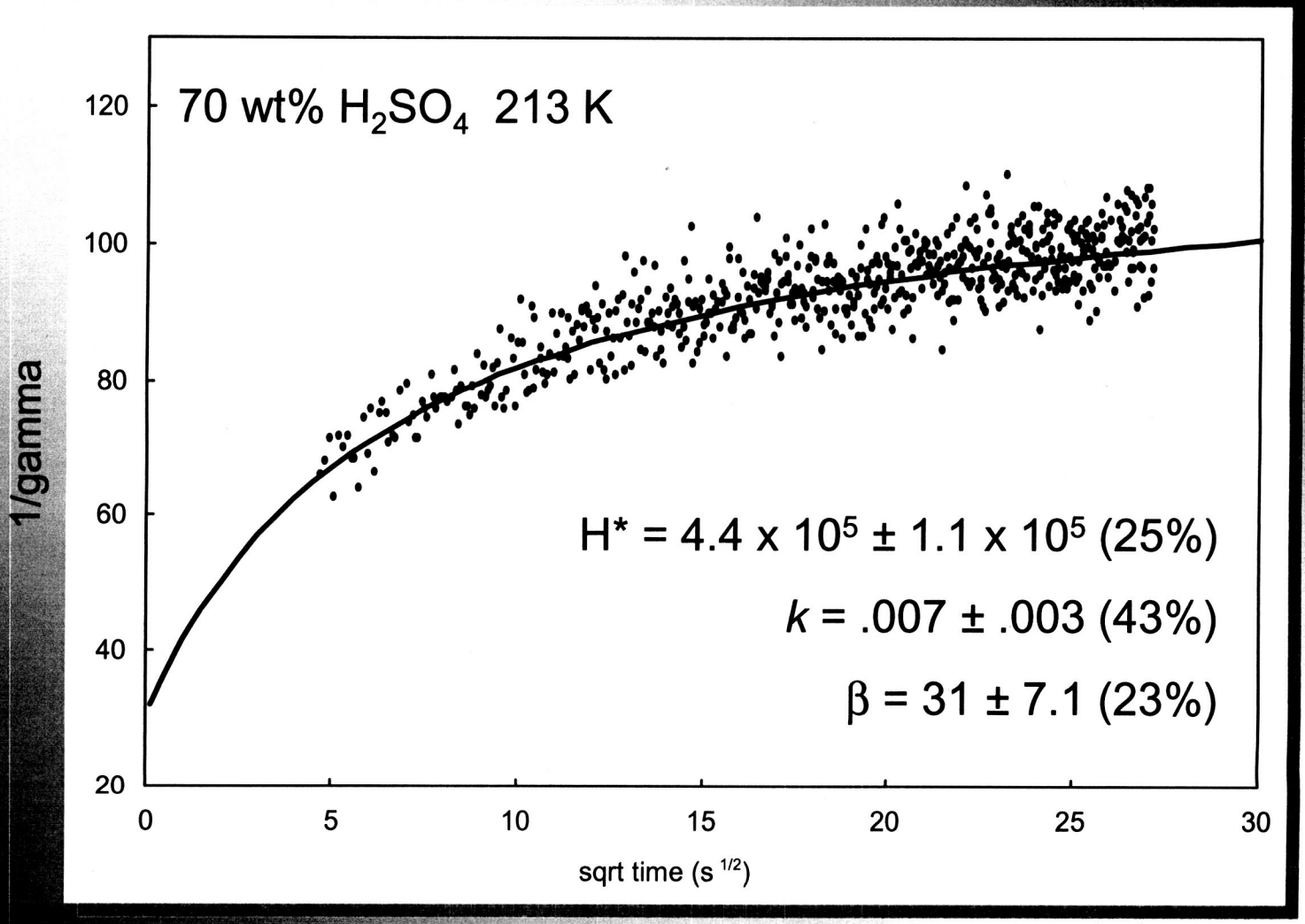

- Henry's Law constant determined within 25%
- [illegible] coefficient better than 50%

Multi-Parameter Fit to Data

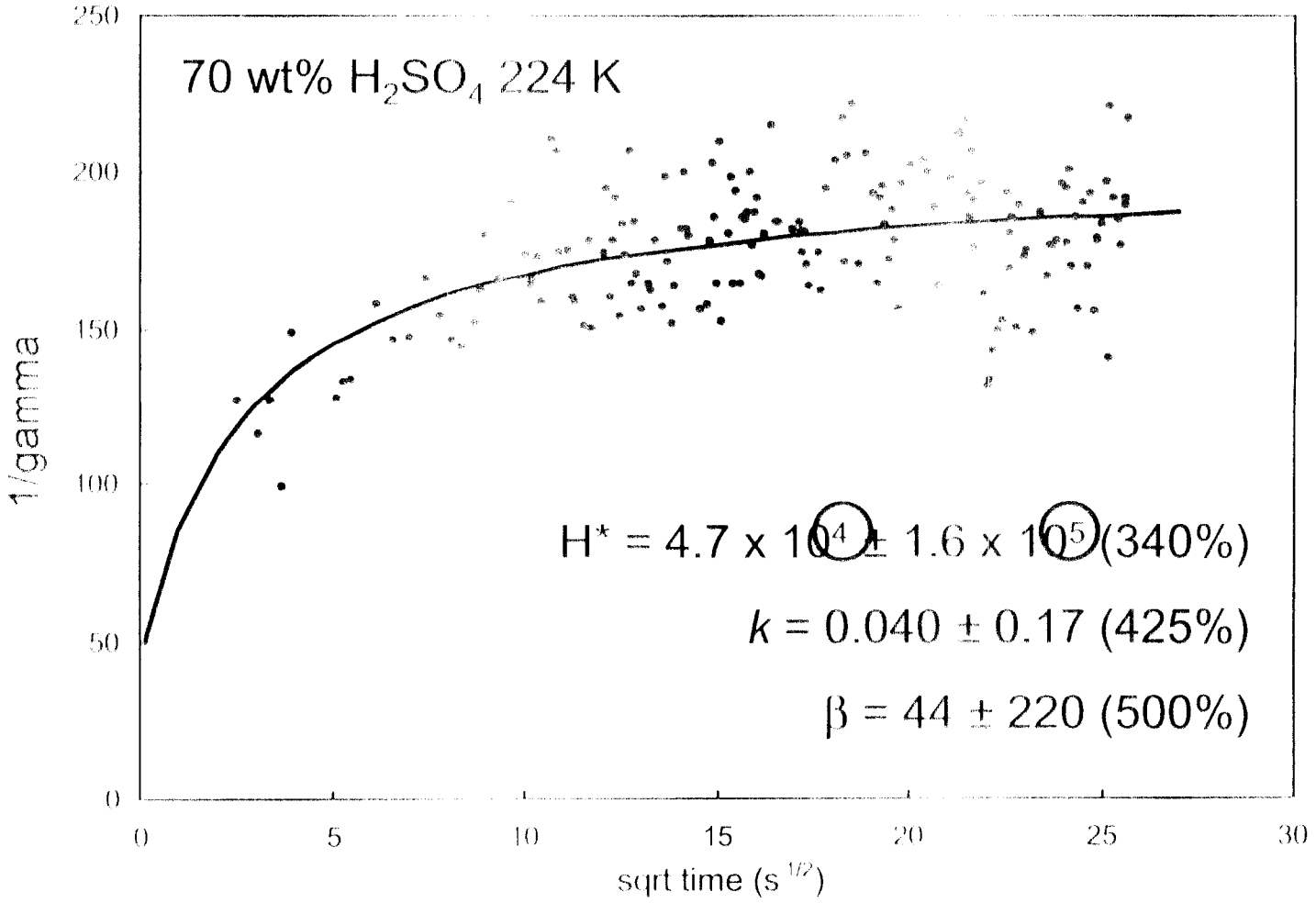

- some data sets provide poorly constrained results
- can lead to factors of 3 or more uncertainly in H^* and k

HOBr Experimental Results

Solubility

$H^* = 10^4 - 10^8$ M atm ^{1}

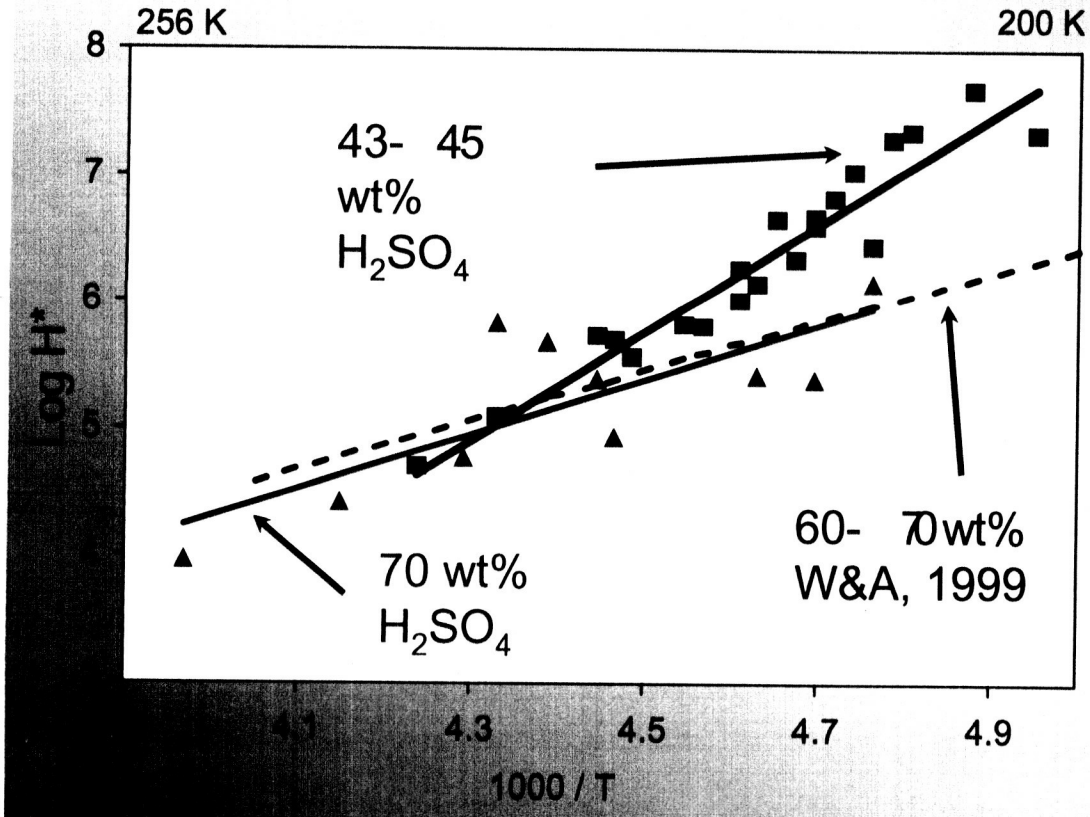

...ined to 0.5 K and averaged, preliminary data

Rea...

- in 45 wt% H_2SO_4, k is usu... zero, no products observed
- for 70 wt% acid, Br_2O and Br_2 released; $k = 10^{-4}$ 10^{-2} s^{-1}

initial analysis gives

k_{II} ~0.5 M $^{1}s^{-1}$ for HOBr + HBr

k_{II} ~0.06 M $^{1}s^{-1}$ for HOBr + HOBr

Atmospheric Implications

Solubility

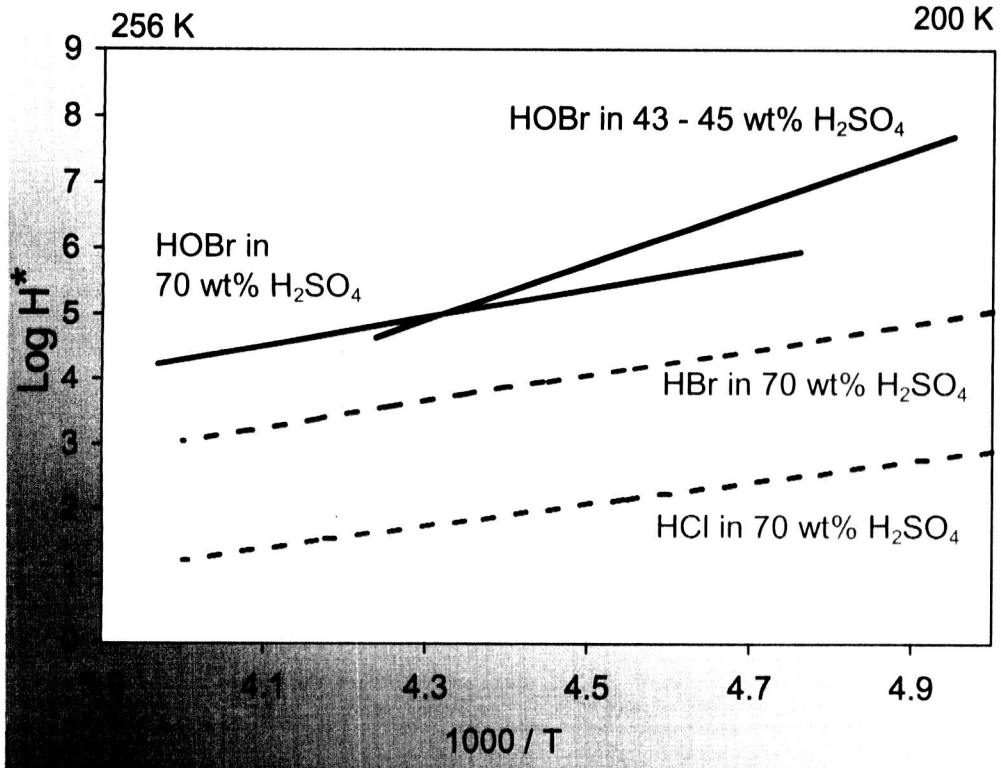

is 10x more soluble than
00x more soluble than HCl

Reactions

$$HOBr + HX \rightleftharpoons BrX + H_2O$$

X = Cl, Br, OBr

$$rate = k\,[HOBr] = k_{II} P_{HX} H^*_{HX} [HOBr]$$

70 wt% H_2SO_4, 213 K	HCl	HBr	HOBr
k_{II} ($M^{-1}s^{-1}$)	**8×10^7**	0.5	0.06
H^* ($M\,atm^{-1}$)	3×10^2	3×10^4	4.4×10^5
mixing ratio	1 ppb	2 ppt	0.6 ppt
k (s^{-1})	**1.4**	2×10^{-9}	1×10^{-9}

- Reaction of HOBr with HCl will dominate in liquid, activating chlorine

Conclusions

- HOBr is significantly soluble in sulfuric acid: $H^* = 10^{$
  43- 45, 55, 60, 70 wt % H_2SO_4 202- 252 K
- Our values of H^* agree with previous measurements
  (Waschewsky & Abbatt, *J Phys Chem A*, 1999)
- Br_2 and Br_2O produced at high acidity
- Determining rate constants from a system where solubility and reaction compete requires data with minimal variability
- Pseudo 1st- order rate constant extracted (preliminary calculations)
- Reactions of HOBr with HBr or HOBr are not likely to compete chlorine activating reaction of HOBr + HCl

Acknowledgements: This work is funded by NASA through the Upper Atmosphere and the Atmospheric Effects of Aviation Program. S. Ashbourn is Dreyfus Foundation. R. Michelsen is supported by the National Research Holsclaw, Eleanore Jehung, Sylvia Law, Chingchia Ly, Joe Metz,

NASA